Stony Brook University

Mechanical Modeling and Analysis of Human Motion for Rehabilitation and Sports

A Dissertation Presented

by

Paul Gonzalo Arauz

to

The Graduate School

in Partial Fulfillment of the

Requirements

for the Degree of

Doctor of Philosophy

in

Mechanical Engineering

Stony Brook University

August 2016

Stony Brook University

The Graduate School

Paul Gonzalo Arauz

We, the dissertation committee for the above candidate for the
Doctor of Philosophy degree,
hereby recommend acceptance of this dissertation.

Imin Kao - Dissertation Advisor
Professor of Mechanical Engineering

Jeffrey Ge - Chairperson of Defense
Professor of Mechanical Engineering

Cindy Chang - Committee Member
Professor of Mechanical Engineering

Sue Ann Sisto - Committee Member
Professor of the School of Health Technology and Management

This dissertation is accepted by the Graduate School

Nancy Goroff
Interim Dean of the Graduate School

Abstract of the Dissertation

Mechanical Modeling and Analysis of Human Motion for Rehabilitation and Sports

by

Paul Gonzalo Arauz

Doctor of Philosophy

in

Mechanical Engineering

Stony Brook University

2016

Modeling and analysis of human motion is important in rehabilitation and sports. To understand functional movements, dynamics of joints, power requirements, and athletic performance, kinematic and kinetic models have to be developed to implement and assess rehabilitation techniques that are applied to unimpaired individuals and patients with movement disorders. In addition, mechanical models are required to evaluate and quantify athletes skills and performance, in order to reduce the risk of potential injuries. For many years, many research efforts have been presented in the field of rehabilitation and movement performance.

This dissertation presents research in mechanical modeling and analysis of human motion focusing on rehabilitation and prevention of sports injury. In particular, the analysis to determine appropriate arthrodesis angle for fingers, as well as the modeling to quantify upper limb joint forces and moments in American football players were investigated.

Several aspects of simulated index finger proximal interphalangeal (PIP) arthrodesis were investigated. First, assessment of quantitative measures of workspace (WS) attributes under simulated PIP joint arthrodesis of the index finger was conducted. Seven healthy subjects were tested with the PIP joint unconstrained and constrained to selected angles.

A model of the constrained finger was developed in order to address the impact of the inclusion of prescribed joint arthrodesis angles on WS attributes. A weighted criterion was formulated to define an optimal constraint angle among several system parameters. Experimental and theoretical modeling results are compared and presented. Secondly, the range of motion (ROM) of the joints and manipulabilities at three selected tip-pinch manipulation postures of the finger were studied experimentally under imposed PIP joint arthrodesis angles. A kinematic model of the index finger was used in experiments which involves three postures. Experimental results are presented. In addition, a general methodology to model the kinematics of a joint constrained finger was investigated. The impact of the inclusion of a specific joint constraint was investigated using two-dimensional (2D) and three-dimensional (3D) workspaces, as well as manipulability measures and ellipsoids. Next, analysis of the effect of simulated PIP joint arthrodesis on distal interphalangeal (DIP) joint free flexion-extension (FE) and maximal voluntary pinch forces was performed. Experiments were conducted using five healthy subjects with the PIP joint unconstrained and constrained to selected angles. Results are presented and discussed. The results of this research facilitate surgeons to determine the optimal fusion angle for joints of human fingers before the arthrodesis operation.

Finally, an inverse dynamics model of the upper limb was developed to test an experimental protocol to measure upper limb joint forces and moments generated by American football players during simulated blocking. An experimenter with football experience volunteered for this study. The maximum blocking force was measured with a custom-built sled including five load cells. 3D motion and kinetics of the football player were measured during hitting of the blocking sled. Model results are presented and discussed. This research provides the understanding of dynamics of the upper limb in order to prevent sport injuries.

Table of Contents

List of Figures

List of Tables

List of Abbreviations

Abbreviation	Description
AA	Abduction-adduction
CMC	Carpometacarpal
D-H	Denavit-Hartenberg
DIP	Distal interphalangeal
DOF	Degree of freedom
ED	Extensor digitorum
EMG	Electromyography
FDP	Flexor digitorum profundus
FE	Flexion-extension
GCS	Global coordinate system
GH	Glenohumeral
IP	Interphalangeal
LCS	Local coordinate system
MCP	Metacarpophalangeal
NC	Non-constrained
PIP	Proximal interphalangeal
RMS	Root-mean-square
ROM	Range of motion
SD	Standard deviation
WS	Workspace
UC	Unconstrained
2D	Two-dimensional
3D	Three-dimensional

Acknowledgements

First and foremost, I would like to express my sincere thanks and appreciation to my advisor and mentor Professor Imin Kao for his guidance throughout this research work. His bright mind brought to me insight and knowledge that have promoted my understanding and have encouraged me to not only grow as a researcher but also as an instructor and independent thinker. Moreover, I would like to thank him for providing me with a not only inspiring but also supportive research environment which has made my education process such a great experience.

I also want to thank Professor Sue Ann Sisto for her advice and providing me with the facilities for conducting experimental studies. Thanks are also due to Professors Jeffrey Ge and Cindy Chang for their assistance and careful reading of this dissertation.

I have had the pleasure of working with and learning from a number of friends and colleagues. Many people have contributed with their comments and effort. All their support and help are gratefully acknowledged: Dr. Rossevelt Moreno, Dr. Jun Nishiyama, Dr. Kunbo Zhang, Gabriel Helguero, Carlos Saldarriaga, Liming Li, Guangyu He, Vamig Mustahsan, and many others. Undoubtedly, the road to the Ph.D. would not have been as smooth without the support from all the friends I have met at Stony Brook.

I would also like to express my heartfelt and gratitude to my mother and family. My mother's memory is a keepsake which has helped me push through these learning and trying years. Without her spiritual support, this dissertation would not have been possible.

Last but not least, I would like to thank my girlfriend Katia. Her love and patience have provided me with unending encouragement and support.

This research work has been conducted with the collaboration of the Manufacturing and Automation Laboratory (MAL) and the Rehabilitation Research and Movement Performance (RRAMP) Laboratory at Stony Brook University. Thanks are also due to Chuancai Zou for his help in doing experiments at the RRAMP Laboratory.

Chapter 1

INTRODUCTION

1.1 Introduction and background

Mechanical models are required to understand three-dimensional (3D) human motion. Indeed, proper functional movements, joint torques, and muscle forces are typically investigated with mechanical models in order to implement and assess motion performance and rehabilitation techniques that are applied to unimpaired and impaired individuals. In this dissertation, kinematic, kinetic, and biomechanical analyses of the index finger and upper limbs, have been developed for: (1) assessment of motion and functional capabilities of fingers under imposed joint constraints, and (2) quantifying athletic performance, motion techniques, upper limb joint moments and forces generated during a simulated blocking activity in collegiate football linemen and linebackers. The results are useful for helping surgeons, physicians, and therapists to make more informed decisions on the selection of immobilization angles. Similarly, the results provide a better understanding of the upper limb joint moments, forces, and muscle activity involved with a simulated blocking activity and how those moments, forces, and muscle activation patterns may be related to clinical signs of posterior shoulder instability in football linemen and linebackers.

Partial or complete kinematic models of the human body can be utilized to investigate functionality, performance, joint angles, trajectories, workspace, among others, when motion is executed. For instance, individual finger workspace and movement can be stud-

ied in unimpaired subjects to determine typical (optimal) joint angles and ranges of motion that allow better capability of movement under imposed joint constraints and when a specific task is being executed. Application of these methods results in better surgical planning and rehabilitation techniques for patients with movement disorders [3, 15, 52, 51]. To this end, arthrodesis, an artificial induction of joint ossification between two bones via surgery, continues to be a pragmatic option in the treatment of pain, deformity, and instability of joints in patients with osteoarthritis and inflammatory arthritis [3, 41, 37, 32, 5]. Nonetheless, when a finger joint has to be fused, preoperative planning has to include a decision on the appropriate angle for arthrodesis [3, 24, 25, 45, 51, 52].

Even though precise modeling of the human motion can be achieved by computerized tomography (CT) or magnetic resonance image (MRI), application of such procedures is not pragmatic when investigating general movement features in several tens of asymptomatic subjects. The placement of surface markers on the body segment to be analyzed is a typical non-invasive method used in accurate capture of three dimensional movements. This approach requires the attachment of surface markers on well-defined bony anatomical landmarks, and marker information is utilized in order to construct kinematic models of the segment body being analyzed.

In this dissertation, the motions of non-constrained (NC) and constrained fingers were utilized in order to investigate the mechanics of motion of the finger when joint constraints are introduced. In particular, the finger workspace, manipulability, functionality, muscle forces, and affected movement due to imposed joint constrain angles have been studied. Kinematic and biomechanical analyses of the index finger when the proximal interphalangeal (PIP) joint is constrained to selected angles have been performed.

In addition, a 3D model of the upper limbs have been developed and applied to investigate athletic performance and upper limb joint forces and moments during a simulated blocking activity in American football linemen and linebackers.

1.2 Preview and outline of following chapters

In Chapter 2, an assessment of quantitative measures of workspace (WS) attributes under simulated proximal interphalangeal (PIP) joint arthrodesis of the index finger is presented. Seven healthy subjects were tested with the PIP joint unconstrained and constrained to selected angles using a motion analysis system. A model of the constrained finger was developed in order to address the impact of the inclusion of prescribed joint arthrodesis angles on WS attributes. Model parameters were obtained from system identification experiments involving flexion-extension (FE) movements of the unconstrained and constrained finger. The data of experimental FE movements of the constrained finger were used to generate the two-dimensional (2D) WS boundaries and to validate the model. A weighted criterion was formulated to define an optimal constraint angle among several system parameters. Experimental and model results were compared and presented.

In Chapter 3, an experimental study of the optimal angle for arthrodesis of fingers based on kinematic analysis with tip-pinch manipulation is presented. To evaluate the appropriate angle for arthrodesis of the index finger proximal interphalangeal (PIP) joint, the range of motion (ROM) of the joints and manipulabilities at three selected tip-pinch manipulation postures of the finger were studied experimentally under imposed PIP joint arthrodesis angles. A kinematic model of the index finger was used in experiments which involves three postures. Experiments were conducted using seven healthy subjects in tip-pinch manipulation tasks to obtain the measurements of finger motions under imposed angles of joint constraint, including the ROM of the joints and the three criteria of manipulability. Data show that the functional ROM and the shape of manipulability ellipses at the fingertip were influenced significantly by the imposed PIP joint constraint in the tip-pinch manipulation tests among subjects. Model and experimental results are also presented.

In Chapter 4, a general methodology to model and investigate a joint constrained finger was developed in order to address the impact of the inclusion of prescribed joint arthrodesis angles on WS and manipulablity. Model parameters were obtained from pre-

vious studies. Two examples of joint arthrodesis (the proximal and distal interphalangeal joints) were used to illustrate of the proposed methodology. A weighted-sum criterion was formulated to define an optimal constraint angle among several system parameters. Model results are compared and presented.

In Chapter 5, a study to analyze the effect of simulated proximal interphalangeal (PIP) joint arthrodesis on distal interphalangeal (DIP) joint free flexion-extension (FE) and maximal voluntary pinch forces was developed. Experiments were conducted using five healthy subjects with the PIP joint unconstrained and constrained to selected angles to produce: (1) free FE movements of the DIP joint at two selected angles of the metacarpophalangeal (MCP) joint, and (2) maximal voluntary tip (thumb and index finger) and chuck (thumb, index, and middle fingers) pinch forces. Results show that the EMG root-mean-square (RMS) values of the Flexor Digitorum Profundus (FDP) and Extensor Digitorum (ED), as well as the range of motion (ROM) of the DIP joint during free FE of the DIP joint did not change significantly. The EMG RMS of FDP and ED showed maximum values when the PIP joint was unconstrained (UC) and constrained at 0° to 20° of flexion during tip and chuck pinch. The index finger MCP and DIP joint positions differed significantly with imposed PIP joint arthrodeses during tip and chuck pinch. Pinch force measurements did not change significantly under simulated PIP joint arthrodesis.

In Chapter 6, an inverse dynamics model was developed in order to test an experimental protocol to measure the upper limb joint forces and moments generated by American football players during simulated blocking. An experimenter with football experience volunteered for this study. The maximum blocking force was measured with a custom-built sled including five load cells. Three dimensional (3D) motion and kinematics of the football player during hitting to the blocking sled were measured with a ten-camera motion capture system. Results show that the model can be used to measure the upper limb joint forces and moments. However, inclusion of force sensing devices with better resolution than the load cells utilized will increase model accuracy.

1.3 Terminology and notations

The terminology used in this dissertation is listed and briefly described in this section.

workspace area: Total area swept by the fingertip as the finger executes all possible ranges of motion [3].

workspace volume: Total volume swept by the fingertip as the finger executes all possible ranges of motion.

manipulability: The ease of arbitrarily changing the position and orientation of the distal phalanx at the tip of the finger [54].

1.3.1 Nomenclature

The nomenclature used in this dissertation are as follows:

coordinate frames:

$\{A\}$: Global coordinate frame

$\{B_i\}$: Local coordinate frame

position and orientations vectors and rotation matrix:

${}^{A}\mathbf{p}$: 3×1 position vector expressed in $\{A\}$ coordinates: ${}^{A}\mathbf{p} = [x\,y\,z]^T$.

${}^{B}\mathbf{p_i}$: 3×1 position vector expressed in $\{B_i\}$ coordinates: ${}^{B}\mathbf{p_i} = [x_i\,y_i\,z_i]^T$.

θ_i : Joint angles of the upper limb

$\mathbf{R}^{-1}$: Inverse of a matrix

$\mathbf{R}^{T}$: Transpose of a matrix

${}^{A}_{B}\mathbf{R}$: Rotation matrix which specifies relationship between coordinate systems $\{A\}$ and $\{B\}$

link parameters:

a_i : link length

α_i : link twist

d_i : link offset

Jacobian and homogeneous transformation matrices:

$\mathbf{J}_\theta$: Joint Jacobian matrix, $\mathbf{J}_\theta \triangleq \frac{\partial \mathbf{X}}{\partial \theta}$

${}^A_B\mathbf{T}$: homogeneous transformations which describes the frame $\{A\}$ relative to the frame $\{B\}$

1.3.2 Notations

The notations used in this dissertation are:

c_1: Notations for the cosine of an angle θ_1 may take any of the forms: $\cos\theta_1 = c\theta_1 = c_1$.

$\mathbf{J}_\theta$: The joint Jacobian matrix [12] which is defined as

$$\mathbf{J}_\theta \triangleq \frac{\partial \mathbf{X}}{\partial \theta} \tag{1.1}$$

${}^{i-1}_{i}\mathbf{T}$: The transform which defines frame $\{i\}$ relative to frame $\{i-1\}$. This transformation will be a function of the four link parameters. The general form of this transform is defined as [12]

$${}^{i-1}_{i}\mathbf{T} = \begin{bmatrix} c\theta_i & -s\theta_i & 0 & a_{i-1} \\ s\theta_i c\alpha_{i-1} & c\theta_i c\alpha_{i-1} & -s\alpha_{i-1} & -s\alpha_{i-1}d_i \\ s\theta_i s\alpha_{i-1} & c\theta_i s\alpha_{i-1} & c\alpha_{i-1} & c\alpha_{i-1}d_i \\ 0 & 0 & 0 & 1 \end{bmatrix} \tag{1.2}$$

Ω: The angular velocity skew-symmetric matrix [1] which is defined as

$$\Omega = \begin{bmatrix} 0 & -\omega_z & \omega_y \\ \omega_z & 0 & -\omega_x \\ -\omega_y & \omega_x & 0 \end{bmatrix} \tag{1.3}$$

vect($\mathbf{A}$)**:** The vector of a 3×3 matrix [1] which is defined as

$$\text{vect}(\mathbf{A}) = \mathbf{a} = \frac{1}{2} \begin{bmatrix} a_{32} - a_{23} \\ a_{13} - a_{31} \\ a_{21} - a_{12} \end{bmatrix} \tag{1.4}$$

tr($\mathbf{A}$)**:** The trace of a 3×3 matrix [1] which is defined as

$$\text{tr}(\mathbf{A}) = a_{11} + a_{22} + a_{33} \tag{1.5}$$

Chapter 2

Assesment of Finger Workspace Attributes Under Simulated Arthrodesis

2.1 Introduction

Fingers have important functions such as grasping, pinching, and manipulating objects which allow humans to interact with their surroundings [21, 20, 22]. Partial or complete loss of these functions due to a disease or injury may require conservative treatment with nonsteroidal anti-inflammatory drugs, steroids injections, splinting, and hand therapy, or more invasive treatment with surgery and rehabilitation techniques which may involve restricting or reducing normal movement to relieve pain, create joint stability, and expedite the recovery process [41]. Patients with osteoarthritis, inflammatory arthritis, and joint trauma are treated by hand surgeons, physicians, and therapists. Although arthrodesis and splinting are common treatments for those conditions, the capability of movement and functionality of the finger have not been carefully considered. For example, arthrodesis, an artificial induction of joint ossification between two bones via surgery, continues to be a pragmatic option in the treatment of pain, deformity, and instability of joints [41, 37, 32, 5]. Nonetheless, when a finger joint has to be fused, preoperative planning has to include a decision on the appropriate angle for arthrodesis [24, 25, 45, 51, 52]. Decisions typically involve aesthetics, information on functional aspects, and patient preferences. While some studies have reported that PIP arthrodesis at 15° to 30° of flexion lead to a more functional

index finger [24]; others have reported that PIP arthrodesis angles at 40° of flexion have a minimal effect on lower-demand activities of daily living [51]. Obviously, constraining a finger joint reduces functionality by reducing the capability of movement and workspace (WS) of the finger. Nevertheless, individual patient function should be considered; for example a guitar player, in the fretting hand, may want the joints more flexed than a data entry operator [24]. Thus, a systematic approach with quantitative analyses will help to make more informed decisions on the fuse angle of arthrodesis.

Different aspects of finger function have been investigated by several researchers. First, the maximal fingertip motion areas of normal and impaired finger joints have been obtained in two-dimensional (2D) measurements using a motion analysis system [9, 10, 11, 8] as a way of quantifying finger movement capabilities. In addition, several studies in literature have measured the functionality of constrained fingers using simulated joint constraint angles and functional tasks [51, 15, 52] to understand how constraint angles affect finger functionality. Moreover, kinematic functional abilities of the hand have been investigated using three-dimensional (3D) modeling and experimental approaches [28, 29] in order to improve designs of handheld objects for individuals with reduced functionality. Several studies have investigated the coupling mechanisms between the DIP and PIP joints in the unloaded finger [26, 19, 33] to advance insight into normal and pathological finger biomechanics. To date, no work analyzing the WS of a finger with a simulated arthrodesis joint has been investigated.

The objective of this study is to investigate how immobilization angles of the PIP joint affect the 2D WS of the index finger by providing the result of quantitative measures of WS attributes that define the areas and shapes of fingertip reach. A finger model of articulated segments, previously used by several authors [26, 39, 53, 35], was utilized to systematically assess the WS attributes for each imposed constraint. The 2D WS of a finger is defined as the total area swept by the fingertip as the finger executes all possible ranges of motion. Comparison between experimental measurements and the theoretical

model was carried out to validate the model. The utility of this approach provides the clinicians and surgeons with a systematic guidance to make more informed decisions before an arthrodesis angle is considered, and customize this angle for each patient in order to enhance the capability of movement of the finger after such intervention.

2.2 Theoretical background

2.2.1 Kinematic model of the index finger

Index finger motions include flexion-extension (FE) of the metacarpophalangeal (MCP), PIP, and distal interphlangeal (DIP) joints, as well as abduction-adduction (AA) of the MCP joint. FE motions of the finger were represented with a kinematic model of articulated segments connected by three hinge joints (MCP, PIP, and DIP joints) [53]. The model assumed three parallel FE joint axes and one AA joint axis that intersects the first FE axis at a right angle [26, 39, 53, 35]. The kinematics of an open chain, such as the index finger, described by the Denavit-Hartenberg (D-H) parameters, is presented in Appendix A. Figures 2.1(a) and 2.1(b) illustrate a schematic representation of the index finger, modeled as a kinematic chain with four revolute or rotary joints (that is, a 4R kinematic chain).

Equation (2.1), derived in Appendix A, describes the Cartesian coordinates (x_{tip}, y_{tip}, and z_{tip}) of the fingertip as a function of the angles of the joints. The Cartesian coordinates of the fingertip are determined with respect to frame $\{0\}$, whose origin coincides with the center of rotation of the MCP joint, and the x_0-axis is along the longest axis of the metacarpal bone in the distal direction.

$$\begin{cases} x_{tip} = & c_1 \left(l_1 c_2 + l_2 c_{23} + l_3 c_{234}\right) \\ y_{tip} = & s_1 \left(l_1 c_2 + l_2 c_{23} + l_3 c_{234}\right) \\ z_{tip} = & -l_1 s_2 - l_2 s_{23} - l_3 s_{234} \end{cases} \tag{2.1}$$

where c_{ijk} and s_{ijk} are $\cos\left(\theta_i + \theta_j + \theta_k\right)$ and $\sin\left(\theta_i + \theta_j + \theta_k\right)$, respectively. The angles θ_1, θ_2, θ_3, and θ_4 are the rotations about the MCP AA, MCP FE, PIP, and DIP joint axes,

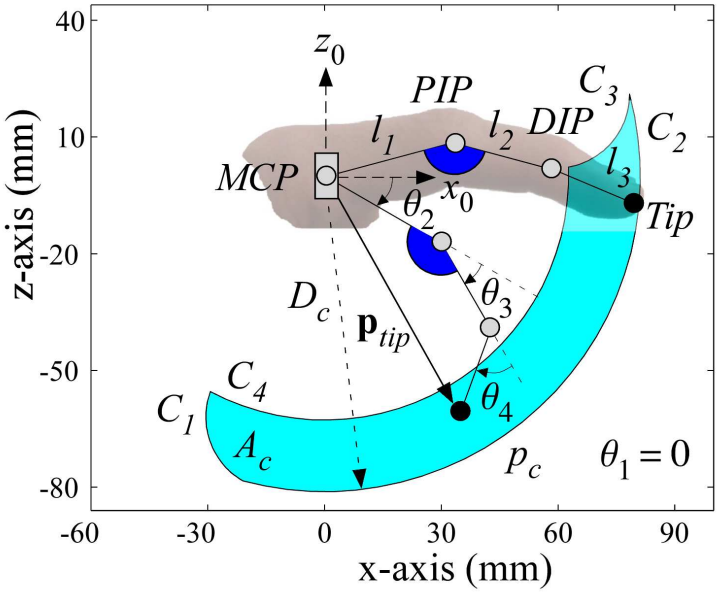

(a) Articulated segment model of the index finger

MCP: Metacarpophalangeal Joint
PIP: Proximal Interphalangeal Joint
DIP: Distal Interphalangeal Joint
Tip: Index Fingertip

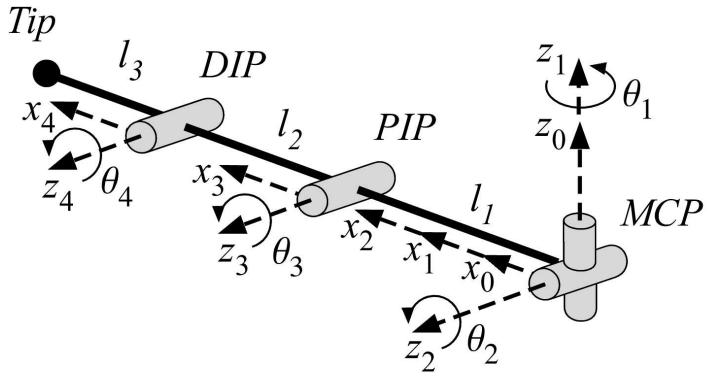

(b) Initial posture of the 4R index finger kinematic chain model

Figure 2.1: (a) Schematic illustration of the articulated index finger segment model. The 2D WS of the PIP joint constrained finger model described in equation (2.1). The parameters are as follows: $l_1 = 42$ mm, $l_2 = 23$ mm, and $l_3 = 19$ mm. The ROM for θ_2 and θ_4 are: $-30^\circ \leq \theta_2 \leq 90^\circ$ and $0^\circ \leq \theta_4 \leq 80^\circ$. The PIP joint constraint angle is: $\theta_3 = 30^\circ$. The 2D WS boundaries are represented by curves C_1, C_2, C_3, and C_4. The WS area, perimeter, and the maximum distance of fingertip reach are: $A_c = 2773$ mm^2, $p_c = 352$ mm, and $D_c = 82$ mm, respectively. Note that the perimeter, p_c, is calculated by adding the lengths of curves C_1, C_2, C_3, and C_4. (b) An initial posture of reference angles of the equivalent kinematic model of the index finger. Note that the length of the unconstrained finger is given by $L = l_1 + l_2 + l_3$.

respectively, and l_1, l_2, and l_3 are the segment lengths of the proximal, middle, and distal phalanges, respectively.

2.2.1.1 Finger coupling mechanisms

The human finger contains tendinous mechanisms that are essential for proper control [27]. One such mechanism couples the DIP (θ_4) and PIP (θ_3) joints in the (unloaded) finger when flexed or extended [26]. Such coupling relation, expressed as $\theta_4 \leq \frac{2}{3}\theta_3$, has been considered in previous finger models [29]. This relation, despite acceptably modeling the motions of the unconstrained finger, is no longer applicable to model a PIP joint with a constrained finger during flexion because now the DIP joint can flex independently. However, extension motions of the DIP joint seem to be affected by distinct immobilization angles of the PIP joint.

2.2.1.2 Generation of 2D WS

Equation (2.1) with model parameters, as well as the ROM of the joints and the value of the PIP joint constraint angle describe the 2D WS boundaries of the constrained finger. Model parameters were obtained from experimental measurements (see Section 2.2.6). An example of the 2D WS of the finger model when the PIP joint (θ_3) is constrained to 30° of flexion is presented in Figure 2.1(a). The parametric expressions of the 2D WS boundaries of the example presented in Figure 2.1(a) are described as

$$
C_1 : \begin{cases} x_{tip} = & l_1 \cos(90^\circ) \\ & +l_2 \cos(90^\circ + 30^\circ) \\ & +l_3 \cos(90^\circ + 30^\circ + \theta_4), \\ y_{tip} = & 0, \\ z_{tip} = & -l_1 \sin(90^\circ) \\ & -l_2 \sin(90^\circ + 30^\circ) \\ & -l_3 \sin(90^\circ + 30^\circ + \theta_4), \end{cases} \quad \text{with} \quad 0^\circ \leq \theta_4 \leq 80^\circ \tag{2.2}
$$

$$
C_2 : \begin{cases} x_{tip} = & l_1 \cos(\theta_2) \\ & +l_2 \cos(\theta_2 + 30^\circ) \\ & +l_3 \cos(\theta_2 + 30^\circ + 0^\circ), \\ y_{tip} = & 0, \\ z_{tip} = & -l_1 \sin(\theta_2) \\ & -l_2 \sin(\theta_2 + 30^\circ) \\ & -l_3 \sin(\theta_2 + 30^\circ + 0^\circ), \end{cases} \quad \text{with} \quad -30^\circ \leq \theta_2 \leq 90^\circ \tag{2.3}
$$

$$
C_3 : \begin{cases} x_{tip} = & l_1 \cos(-30^\circ) \\ & +l_2 \cos(-30^\circ + 30^\circ) \\ & +l_3 \cos(-30^\circ + 30^\circ + \theta_4), \\ y_{tip} = & 0, \\ z_{tip} = & -l_1 \sin(-30^\circ) \\ & -l_2 \sin(-30^\circ + 30^\circ) \\ & -l_3 \sin(-30^\circ + 30^\circ + \theta_4), \end{cases} \quad \text{with} \quad 0^\circ \leq \theta_4 \leq 80^\circ \tag{2.4}
$$

$$
C_4 : \begin{cases} x_{tip} = & l_1 \cos(\theta_2) \\ & +l_2 \cos(\theta_2 + 30^\circ) \\ & +l_3 \cos(\theta_2 + 30^\circ + 80^\circ), \\ y_{tip} = & 0, \\ z_{tip} = & -l_1 \sin(\theta_2) \\ & -l_2 \sin(\theta_2 + 30^\circ) \\ & -l_3 \sin(\theta_2 + 30^\circ + 80^\circ), \\ \text{with} & -30^\circ \leq \theta_2 \leq 90^\circ \end{cases} \tag{2.5}
$$

2.2.2 Design indices

The consideration of kinematic and functional aspects of the finger is important to select the arthrodesis angle that best suits the needs of a patient. In order to assess some of those aspects, quantitative measures of WS attributes that describe the areas and shapes of the fingertip reach were analyzed. In particular, measures of WS attributes of the index finger were investigated under imposed PIP joint constraint angles. Equation (2.6) defines an index pertaining to the 2D WS area

$$
I_A = \frac{A_c(\theta_3)}{L^2} \tag{2.6}
$$

where I_A is the index of the 2D WS, $A_c(\theta_3)$ is the WS area when the PIP finger joint is constrained to a prescribed angle, as shown in Figure 2.1, and L is the length of the unconstrained finger.

Equation (2.7) defines an index pertaining to the aspect ratio of 2D WS

$$
I_a = \frac{\sqrt{A_c(\theta_3)}}{p_c(\theta_3)} \tag{2.7}
$$

where I_a is the index of the aspect ratio of 2D WS, and $p_c(\theta_3)$ is the perimeter of the constrained 2D WS, as shown in Figure 2.1(a).

Equation (2.8) defines an index pertaining to the maximum distance of fingertip reac.

$$
I_D = \frac{D_c(\theta_3)}{L} \tag{2.8}
$$

where I_D is the index of the maximum distance of fingertip reach, $D_c(\theta_3)$ is the maximum distance of fingertip reach when the finger joint is constrained to a prescribed angle, as shown in Figure 2.1(a), and L is the maximum distance of fingertip reach when the finger is unconstrained.

The design indices defined above describe different attributes in the consideration of movement and performance of the finger after joint constraints are imposed.[1] Since each index considers different attributes of the constrained finger and has different ranges of numerical values, the selection of the arthrodesis angle is an optimization which takes into account the trade-offs between conflicting objectives. Although a single solution does not exist to simultaneously optimize each objective, we used a weighted-sum criterion to estimate the constraint angle that best satisfies such condition among the three indices (I_A, I_a, and I_D) as follows

$$\max_{\theta_3} \; f(\theta_3) \tag{2.9}$$

where f is the objective function to be optimized, defined as

$$f(\theta_3) = \sum_{i=1}^{n} \alpha_i \frac{I_i(\theta_3) - \min\{I_i\}}{\max\{I_i\} - \min\{I_i\}} \tag{2.10}$$

where α_i are the weighting factors to adjust for emphasis among considered indices with $\sum \alpha_i = 100\%$, $I_i(\theta_3)$ are index values pertaining to a particular attribute (i) and for a prescribed PIP constraint angle (θ_3), and $i = A, a, D$ are the number of design indices considered. Note that the values of the parameters in equation (2.10) depend on the constraint PIP angle, θ_3. The objective criterion can be adjusted depending on the finger utilization and preferences of each individual; thus, inclusion of the weighting factors allows to customize this perspective and quantify an optimal PIP joint constraint angle among the attributes provided in the design indices.

[1] Although the PIP joint constraint was used in this study, such indices can be calculated for other fingers using similar definitions in a wide variety of other situations.

2.2.3 Data acquisition

Participants: Five male and two female right-handed subjects, aged between 25 to 34, volunteered in this study. All participants had no previous history of upper extremity disorders. Prior to data collection, subjects signed an informed consent document approved by the Stony Brook University Institutional Review Board.

Instrumentation: A ten-camera motion capture system (Vicon MX, Oxford, UK) at a sample frequency of 100 Hz, was arranged in a 2 m $\times$ 2 m square region for data collection. Three dimensional coordinate measurement was determined to be well within 0.5 mm [26]. Seven reflective markers were attached to the dorsal aspects of the index finger and hand with double-sided tape. Figure 2.2 illustrates the marker placements for the 7 $\times$ 9.5 mm spherical markers. Markers were placed proximal to the joint on the distal head of the proximal bone [34]. An 80 mm light-extension frame with two markers, one at the tip and the other one in the middle of the frame, was built and attached to the tip of the index finger to avoid marker occlusion during task motions (Figure 2.2). In particular, close fist postures having a fingertip marker completely occluded by the palm. Custom-made thermoplastic splints were used to constraint the PIP joint at distinct angles (Figure 2.2). One observer customized each PIP splint based on each individual finger length. Manual goniometers were used to verify the constraint angles and adjust the splints accordingly. Once splints were made, they were placed on the finger. Particular attention was needed for splint placement to avoid hindering motion at the MCP and DIP joints. Splints were secured with adhesive circumferential tape.

Setup: During measurements the hand, wrist, and forearm comfortably rested on a height-adjustable table. The wrist was supported by the table and held at a steady neutral position (Figure 2.2). All fingers were flexed and relaxed with exception of the index finger, which performed the movements instructed. FE motions were used to estimate finger parameters. The boundaries of the 2D WS of the index finger were obtained by moving the fingertip (FE movements) at extreme positions. Subjects were instructed to

keep the wrist at a steady position and continuously perform a series of prescribed finger movements:

(1) Starting from a close fist position (all finger joints fully flexed), full extension of the finger by maintaining the MCP joint fully flexed (at approximately 90° of flexion).

(2) The MCP joint is then fully extended by keeping the PIP and/or DIP joints fully extended.

(3) Full flexion of the PIP and/or DIP joints by keeping the MCP joint at maximum extension.

(4) Full flexion of the MCP joint by maintaining the PIP and/or DIP joints fully flexed.

At least five cycles were recorded for each type of motion. Repetitive motions were measured under two conditions: (1) unconstrained finger, and (2) with the index finger PIP joint constrained to 0°, 20°, 30°, 40°, 50°, and 60° of flexion. Participants performed a 20-second trial in each task. Each subject performed a practice trial with the unconstrained and constrained finger before data recording.

2.2.4 Data processing

In order to analyze finger motions, each marker was taken as a set of three points indicating the relative x, y and z coordinates of the marker in space, relative to the Vicon coordinate system, or global coordinate system (GCS). A local coordinate system (LCS) is then embedded in the hand plane defined by the marker model and subsequent planes and vectors are defined relative to the hand plane. Data were exported to and processed with MATLAB (MathWorks Inc., Natick, MA, USA) software package. Data were filtered using a second order Butterworth low-pass filter with 20 Hz cut-off frequency. Three vectors, one for each phalanx were created using markers placed on the MCP, PIP, and DIP joints,

and a virtual marker at the fingertip created 40 mm apart from the middle marker of the light-extension frame and towards the fingertip. FE movements of the MCP, PIP, and DIP joints are calculated with respect to the plane defined by the markers placed on the hand (Figure 2.2). Movements and joint angle calculations were performed according to Metcalf *et al.* [34]. Only FE angles were considered. Small rotations in other directions due to non-constant interphalangeal joint axes were neglected because of the assumption of parallel FE joint motions. To analyze a WS generation trial, fingertip trajectory points were projected on a plane paralleling the long axis of the finger, and fingertip motion was measured in a 2D plane. The areas of the regions enclosed by the projected points were computed and analyzed with MATLAB. Subjects performed 5 cycles of WS generation. At least three cycles were selected arbitrarily for analysis of the WS test. The approximate duration of the WS cycle was 4 seconds.

2.2.5 Statistical analysis

Statistical significance of the simulated PIP joint constraint angles was analyzed with repeated measures ($p < 0.05$, with the significance level being 0.05) across the subjects using one-way analysis of variance (ANOVA). The simulated PIP joint constraint angles were randomized and assigned by the experimenter. The result of each condition was represented as the average across three measurements.

2.2.6 Parameter estimation

Estimation of segment lengths, as well as the center of rotation of the MCP, PIP, and DIP joints were obtained by applying least-squares fitting methods to marker trajectories during FE tasks [16, 53]. Measurement of the ROM of the joints was conducted using the planes and vectors described in Section 2.2.4.

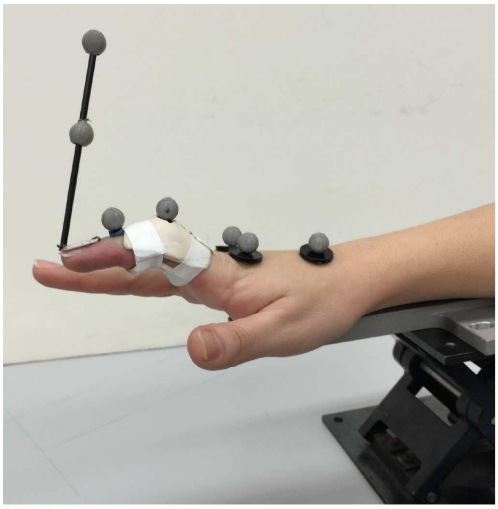

(a)

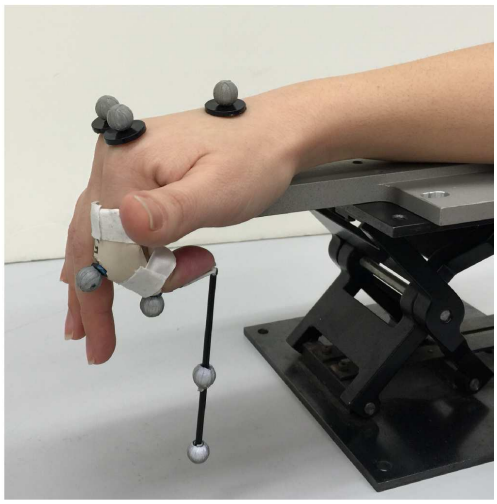

(b)

Figure 2.2: Finger postures with 9.5 mm spherical markers attached and the PIP joint splinted. The 80-mm light-extension frame with two markers attached to the fingertip prevented marker occlusion during finger motions. Finger postures during task performance: (a) full extension of the MCP and DIP joints, and (b) full flexion of the MCP and DIP joints.

2.2.7 Experimental validation of model

Experimental measurements of the design indices of the 2D WS attributes (area, shape, and maximum distance of fingertip reach) of each subject and model results of the constrained finger were compared to assess the validity of the model under imposed PIP joint constraint angles. Model segment lengths were obtained from finger experimental data of each subject. Likewise, the average ROM of the MCP and DIP joints of the unconstrained finger of all subjects was included in the model for each PIP constraint angle analyzed. Once model parameters were established, model implementation was straightforward as explained in Section 2.2.1.2.

2.3 Results

The estimation of the segment lengths of the index finger for all subjects were $l_1 = 42$ mm (SD 4 mm) and $l_2 = 23$ mm (SD 2 mm), and the estimation of distance from the DIP joint center to the marker point on the fingertip was $l_3 = 19$ mm (SD 1 mm). The mean active (FE movements) ROM of the MCP and DIP joints of the unconstrained (UC) and constrained index finger for all the subjects are presented in Figure 2.3. The active ROM of the MCP and DIP joints of the index finger did not change significantly ($p > 0.05$) among subjects under selected PIP joint constraint angles. Table 2.1 shows the average and standard deviation of experimental measurements of the 2D WS area, perimeter, and the distance of maximum fingertip reach of all subjects when the PIP joint was constrained to the selected angles. Table 2.2 shows the theoretical data of the 2D WS area, perimeter, and the distance of maximum fingertip reach when the PIP joint was constrained to the selected angles. The model was constructed by using equation (2.1) along with the segment lengths (l_1, l_2, and l_3), the PIP joint constraint angle (θ_3), and the ROM of the MCP (θ_2) and DIP (θ_4) joints of the unconstrained finger by averaging the parameters of all subjects. While experimental measurements of the 2D WS areas changed significantly ($p < 0.05$) under the imposed PIP joint constraints among subjects (Table 2.1), measurements of perimeters and

fingertip reach distances did not differ significantly ($p > 0.05$). The average experimental values for the 2D WS areas were all lower than the theoretical values, whereas perimeters and fingertip reach distances presented small differences (Table 2.1).

Figure 2.4 shows the 2D WS boundaries of one subject (subject no. 4) obtained from experimental measurements and the model of the finger with the PIP joint unconstrained and constrained to three selected PIP angles of 0°, 40°, and 60° of flexion. In addition, experimental and model angles of the MCP (θ_2) joint were plotted on the horizontal axis, and those of the DIP (θ_4) joint on the vertical axis of a rectangular coordinate system during WS generation for one subject (see Figure 2.4). This result described the variability of the ROM of the MCP and PIP joints during WS generation. The model included a constant (average of all subjects) ROM of the MCP and DIP joints. While the differences between the theoretical model and experimental results are small when the PIP joint is constrained to 40° of flexion (10%), these increased significantly when the PIP was constrained to 0° ($< 50\%$) and 60° (25%) as it can be observed in Figure 2.4.

The design indices, I_A, I_a, and I_D, of the index finger changed significantly ($p > 0.05$) among subjects under selected PIP joint constraint angles. The average and standard deviation values of the design index pertaining to the 2D WS area, shown in Fig. 2.5(a), indicate the greatest WS areas for PIP joint constraint angles of 40° to 50° of flexion. Figure 2.5(b) show the average and standard deviation data of the aspect ratio index. I_a increased as the PIP constraint angle increased. This means that the 2D WS shapes were more evenly distributed as the PIP constraint angles increased. The average and standard deviation values of I_D indicate that the maximum distance of fingertip reach decreased monotonically as the PIP joint increased. With PIP joint constraint angles of 30°, 40°, 50°, and 60°, the maximum distance of fingertip reach is reduced by approximately 3, 4, 7, and 10 %, respectively (Figure 2.5(c)).

Experimental WS attributes of one subject (subject no. 4) and a general model, including the average of the ROM of the MCP and DIP joints of the unconstrained finger

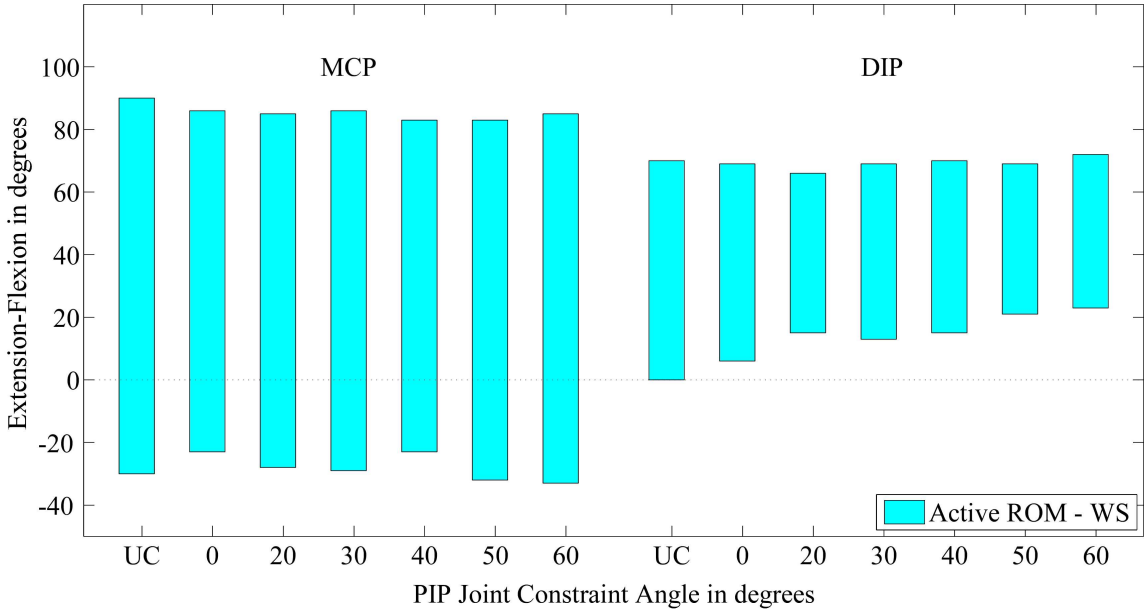

Figure 2.3: The active ROM of the MCP and DIP joints of the index finger when the PIP joint is unconstrained (UC) and constrained to selected angles of 0°, 20°, 30°, 40°, 50°, and 60° of flexion.

Table 2.1: The average data of the experiment of seven healthy subjects over three measurements. A_c: average 2D WS area; p_c: average 2D WS perimeter; D_c: average 2D WS maximum distance of fingertip reach; SD: standard deviation.

Subject	Average	1	2	3	4	5	6	7	Mean	SD
PIP 0°	A_c mm^2	1089	1449	734	1260	1169	1266	866	1115	252
	p_c mm	409	445	270	398	297	324	344	354	63
	D_c mm	90	91	79	88	79	78	78	83	6
PIP 20°	A_c mm^2	1435	1966	987	1761	1352	1543	1194	1463	332
	p_c mm	384	469	260	393	319	312	333	353	68
	D_c mm	89	90	78	87	78	77	77	82	5
PIP 30°	A_c mm^2	1809	2567	1058	2357	1629	1569	1320	1759	540
	p_c mm	374	456	252	381	309	303	348	346	66
	D_c mm	88	89	77	86	77	76	76	81	6
PIP 40°	A_c mm^2	1910	2737	1033	2729	1630	1519	140	1863	649
	p_c mm	360	440	243	392	297	292	336	337	67
	D_c mm	86	87	75	84	76	75	75	80	6
PIP 50°	A_c mm^2	1967	2378	1055	2793	1678	1654	1545	1867	573
	p_c mm	349	420	232	374	284	305	321	326	62
	D_c mm	84	85	74	82	74	73	73	78	6
PIP 60°	A_c mm^2	1978	2320	1206	2315	1688	1736	1487	1819	415
	p_c mm	330	398	219	354	268	288	304	309	58
	D_c mm	81	83	71	79	72	71	71	75	6

Table 2.2: Theoretical data obtained with the constrained finger model. The model parameters are as follows: $l_1 = 42$ mm, $l_2 = 23$ mm, and $l_3 = 19$ mm. The ROM for θ_2 and θ_4 are: $-30^\circ \leq \theta_2 \leq 90^\circ$ and $0^\circ \leq \theta_4 \leq 80^\circ$.

Model	PIP 0°	PIP 20°	PIP 30°	PIP 40°	PIP 50°	PIP 60°
A_c mm^2	2136	2615	2773	2870	2902	2870
p_c mm	374	361	352	339	325	308
D_c mm	84	83	82	80	78	76

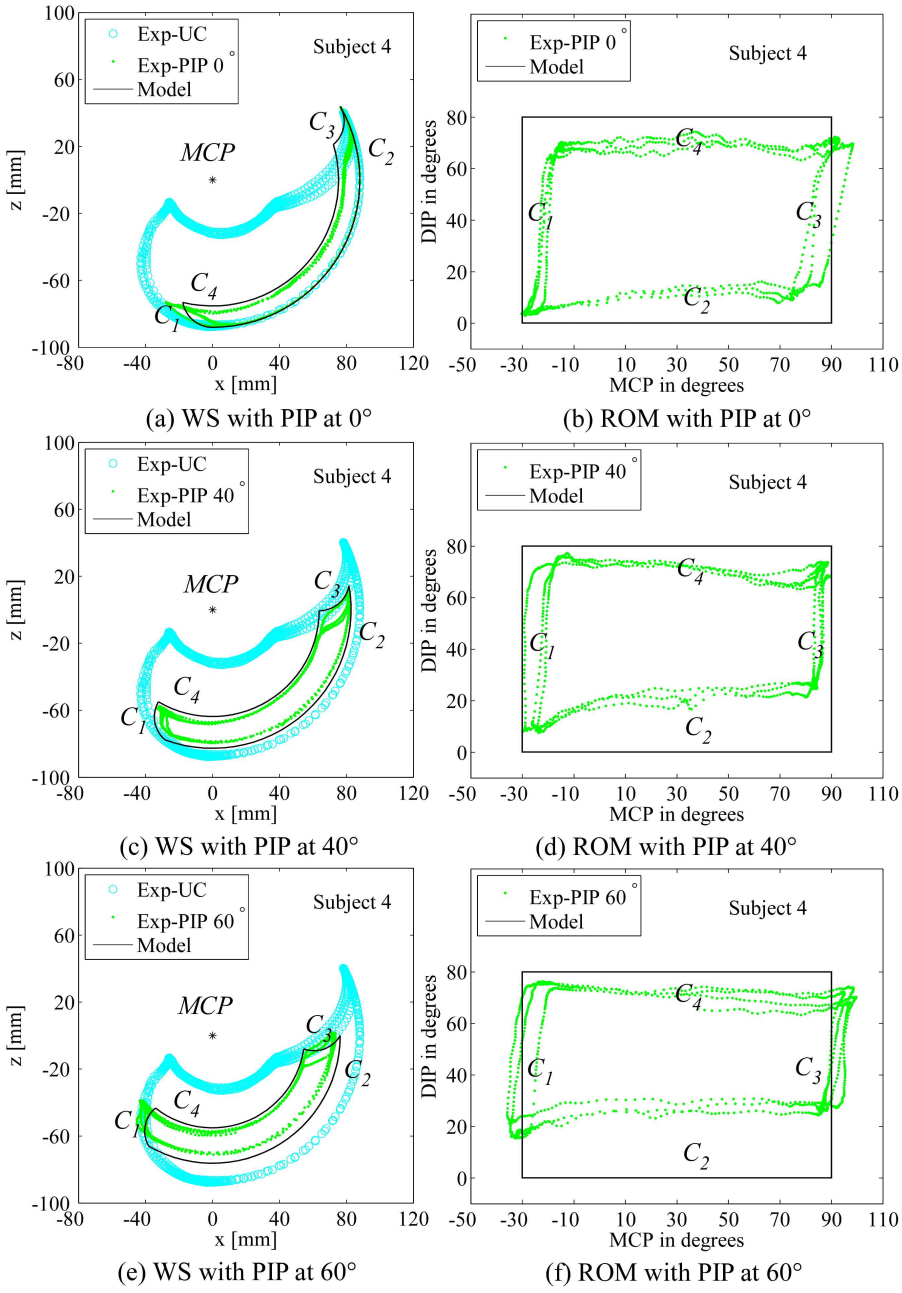

Figure 2.4: The experimental 2D WS boundaries when the PIP joint is unconstrained (UC)(cyan circles) and constrained (green dots). The black solid line shows the 2D WS boundaries C_1, C_2, C_3, and C_4 of the theoretical finger model. The model used a constant (average of all subjects) ROM of the joints. The parameters are as follows: $l_1 = 44$ mm, $l_2 = 26$ mm, and $l_3 = 18$ mm. The ROM for θ_2 and θ_4 are: $-30^\circ \leq \theta_2 \leq 90^\circ$ and $0^\circ \leq \theta_4 \leq 80^\circ$. Model and experimental constrained areas are: (a) 2178 and 1260 mm^2, (c) 2908 and 2729 mm^2, and (d) 2908 and 2315 mm^2, with the PIP constrained angle at 0°, 40°, and 60° of flexion, respectively. Experimental (gray dots) and model (black solid line) angles of the MCP (θ_2) joint plotted on the horizontal axis, and those of the DIP (θ_4) joint on the vertical axis of a rectangular coordinate system during generation of the WS boundaries C_1, C_2, C_3, and C_4 for one subject with the PIP constrained to: (b) 0°, (d) 40°, and (f) 60° of flexion.

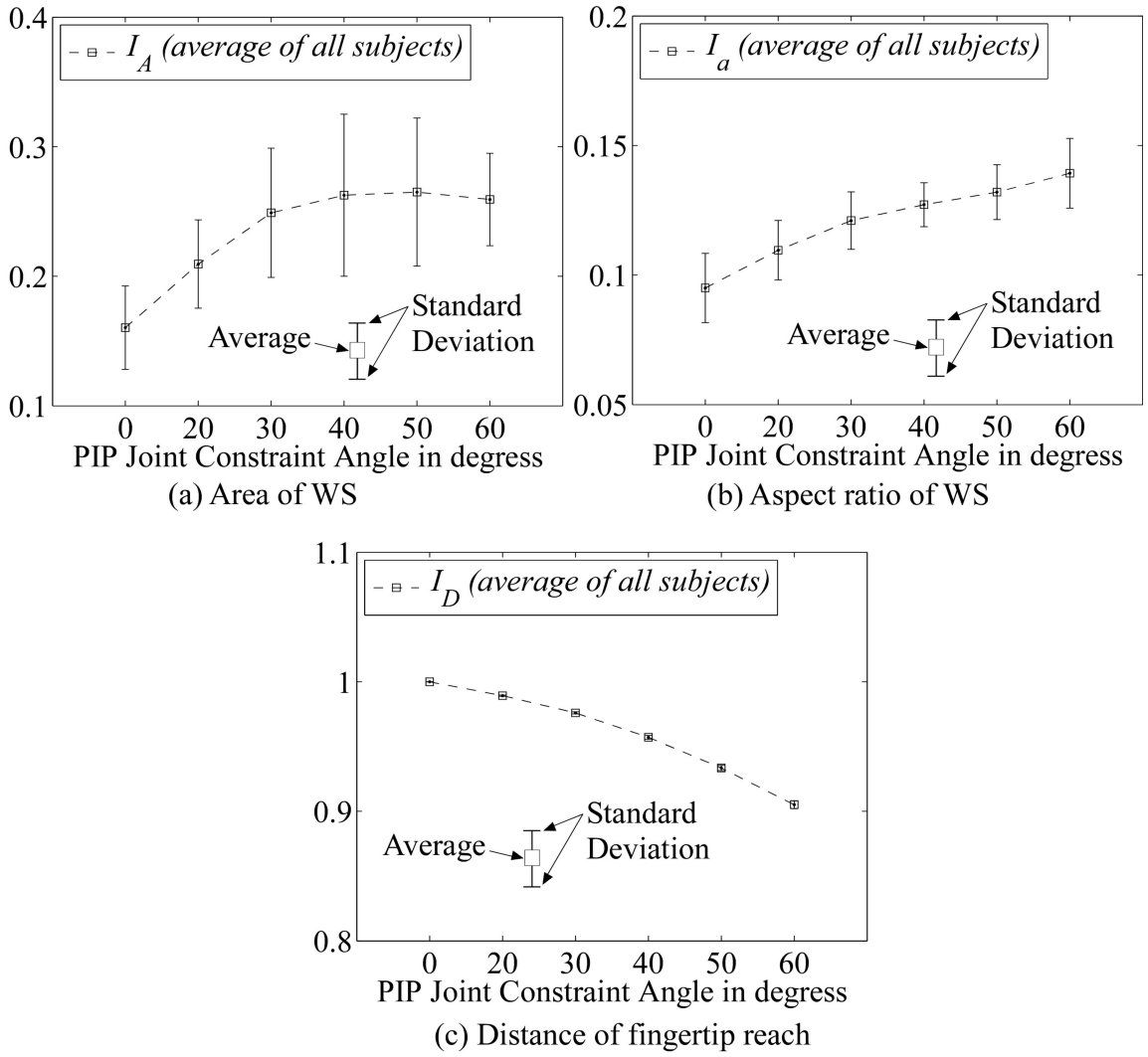

Figure 2.5: The design indices: (a) pertaining to the WS area, I_A ; (b) pertaining to the WS aspect ratio, I_a; and (c) pertaining to the maximum distance of fingertip reach, I_D, of the constrained finger with experimental data of all subjects.

of all subjects, were compared and are shown in Fig. 2.6. Experimental and model design indices pertaining to the 2D WS area, shown in Figure 2.6(a), indicate that the greatest WS areas were for PIP joint constraint angles of 40° to 50° and 40° to 60° of flexion, respectively. Figure 2.6(b) shows that the aspect ratio index, I_a, of the model and experiments, increased as the PIP constraint angle increased. Similarly, the theoretical values of I_a were greater than experimental ones due to a reduced ROM of the MCP and DIP joints during experimental motions. Small differences were observed between values of experiment measurements and model prediction of I_D.

To illustrate the usage of the weighted-sum criterion in equation (2.10), we considered three scenarios. First, if all indices were weighted equally and treated with equal importance, the weighting factors would be $\alpha_A = \alpha_a = \alpha_D = \frac{1}{3}$. Using the results from Fig. 2.6 with different constraint angle θ_3, the maximum of funtion f in equation (2.10) was obtained, and plotted in Figure 2.7. The second scenario emphasizes the 2D WS area, with a choice of $\alpha_A = 0.6$, $\alpha_a = 0.2$, and $\alpha_D = 0.2$ for the weighted-sum. The optimized index f was obtained and plotted in Figure 2.7. In the third scenario, the emphasis was in the consideration of the 2D WS shape, with a penalty on large aspect ratio, in order to make the WS more homogeneous.[2] With a choice of $\alpha_A = 0.2$, $\alpha_a = 0.6$, and $\alpha_D = 0.2$ to meet the criterion, f was obtained and plotted in Figure 2.7. In the first scenario when all indices are weighted equally and treated with equal importance, experimental and theoretical values of f in Figure 2.7 (a) and (b) reached their maximum values with the PIP joint constraint angle between 40° and 50° of flexion. In the second scenario, experimental and theoretical values of f are maximum when the PIP joint was constrained at 50° of flexion. With an emphasis of the aspect ratio of the 2D WS, I_a, in the third scenario, experimental and theoretical values of f reached their maximum values when the PIP joint was constrained at 50° and 60°, respectively.

[2] WS with small aspect ratio will appear as a long and slender strip shape, which will limit the ability to freely move from one point to the other within the WS as in Figure 2.4(a).

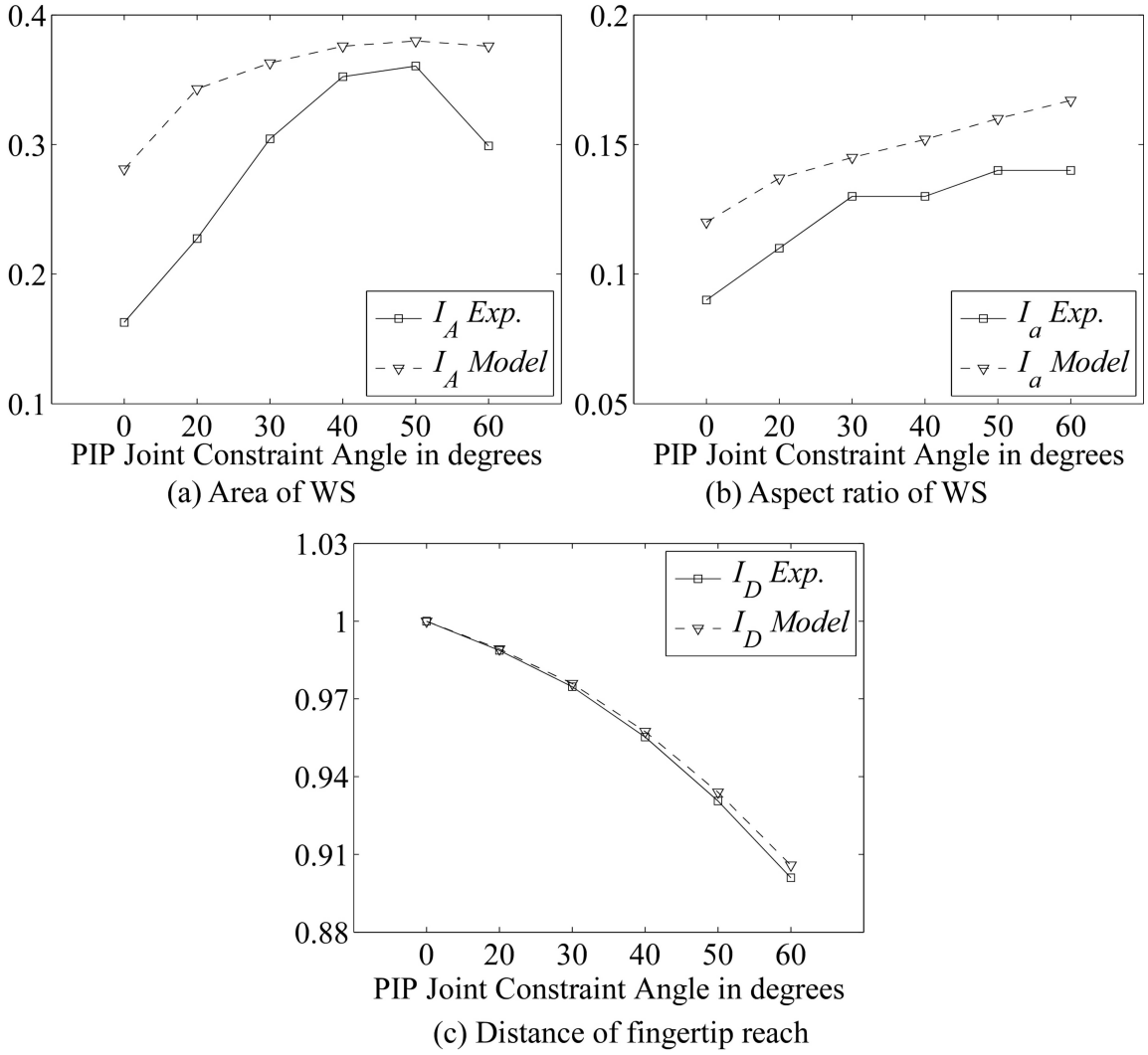

Figure 2.6: Comparison of design indices of the constrained finger between the experimental data of one subject (subject no. 4) and model prediction. The parameters of the model are as follows: $l_1 = 44$ mm, $l_2 = 26$ mm, and $l_3 = 18$ mm. The ROM for θ_2 and θ_4 are: $-30^\circ \leq \theta_2 \leq 90^\circ$ and $0^\circ \leq \theta_4 \leq 80^\circ$.

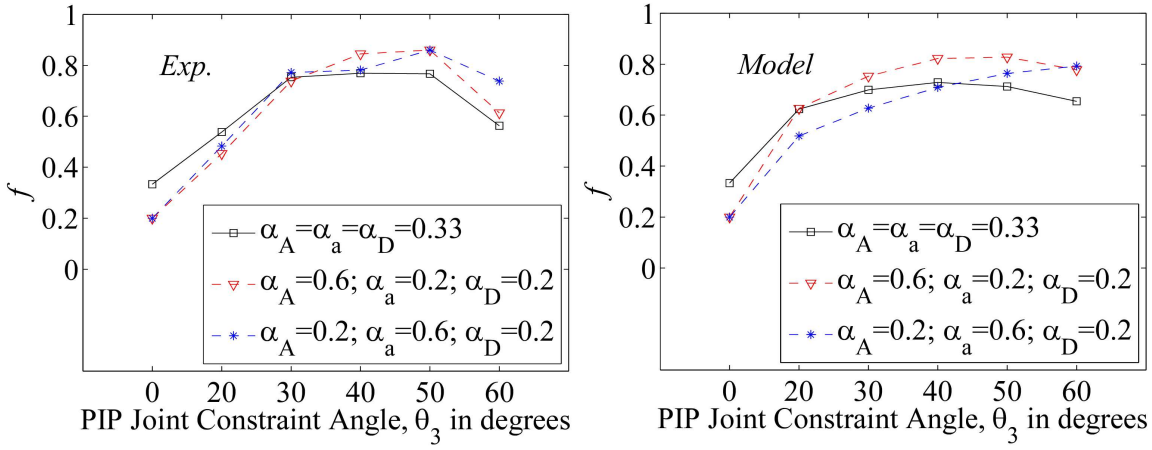

(a) Experimental measurements (b) Theoretical prediction

Figure 2.7: The weighted-sum criterion, f in equation (2.10), as a function of the PIP joint angle θ_3, for different sets of α_i. The experimental measurements and theoretical prediction are presented in (a) and (b), respectively.

2.4 Discussions

This study investigated the impact of simulated index finger PIP arthrodesis based on 2D WS attributes. Development of a theoretical model and methodology to quantify the 2D WS attributes of a finger under imposed joint constraints offers investigators several advantages over current methods used to estimate the appropriate angle for arthrodesis. Indeed, finger models can be used to document functional abilities and design for functional ability. In addition, the importance of using a kinematic model resides in the fact that it can be applied to determine very localized information based on analyzing the global finger behavior of a normative population. Current methods are limited to select arthrodesis angles based on values of experimental data obtained from few finger functional tasks and simulated joint arthrodesis [51, 15, 52]. Investigation of the 2D WS attributes of the constrained finger using theoretical models will provide surgeons and clinicians with guidance to make more informed decisions on the selection of the appropriate constraint angle, and customize this angle for each patient using the optimized weighted-sum proposed in this study.

2.4.1 The ROM of the joints

The DIP joint tendes to slightly decrease its active ROM as the PIP joint constraint angles increased, based on results presented in Figure 2.3. This could be explained due to the coupling mechanisms between the PIP and DIP joints (see Section 2.2.1.1). The human finger contains tendinous mechanisms that are essential for proper control. It is known that the PIP and DIP joints move together in flexion and extension [19, 26]. Thus, constraining the motion of the PIP joint seemed to have an effect on the active ROM of the DIP joint of the constrained finger (Figures 2.3, 2.4b, 2.4d, and 2.4f).

2.4.2 Comparison of experimental and theoretical 2D WS data

The 2D WS of the index finger under imposed PIP joint constraint angles was measured using a motion analysis system. A kinematic model of the constrained finger was used to estimate the 2D WS dimensions. Since the DIP joint was flexed independently when the PIP joint was constrained, coupling mechanisms between the PIP and DIP joints were neglected. However, experimental data of the ROM of the joints suggested that other complex anatomical structures may still have an effect on the extension motion of the DIP joint of the constrained finger (Figure 2.4b, 2.4d, and 2.4e). The average values of experimental measurements of the 2D WS areas of the index finger under imposed PIP joint constraint angles showed that the greatest areas (capability of movement of the fingertip) were obtained for PIP joint constraint angles from 40° to 60° (Table 2.1). This result, despite concurring with the results obtained with the finger model, presented lower values because model parameters included a constant average ROM of the MCP and DIP joints (Table 2.1 and 2.2). Theoretical and experimental measurements of the 2D WS perimeters and maximum distance of fingertip reach presented small differences in Tables 2.1 and 2.2. Nonetheless, since the model used a constant (average of all subjects) ROM of the MCP and DIP joints, the 2D WS perimeter continuously decreased as the PIP joint constraint angle increased (Table 2.2). This was not observed in experimental results due to variations in the ROM of the MCP and DIP joints under imposed PIP joint constraint angles (Table 2.1). Indeed, model accuracy depended on the selection of the ROM of the MCP and DIP joints. Even though model and experimental results matched well when the PIP joint was constrained to 40° (Figure 2.4), applicability of the model was affected when a constant (average of all subjects) ROM of the MCP and DIP joints was considered.

2.4.3 Experimental design indices

Design indices were defined and calculated to assess the 2D WS attributes of the finger under imposed joint constraint angles. Experimental results of the average of all

subjects were used in the assessment of 2D WS attributes using three design indices. Even though the perimeter, p_c, and the maximum distance of fingertip reach, D_c, did not change significantly among subjects, their normalization through the design indices I_a and I_D presented significant differences. In fact, the three design indices, I_A, I_a, and I_D, differed significantly ($p > 0.05$) among subjects under selected PIP joint constraint angles. The I_A index, with constrained PIP joint is plotted in Figure 2.5(a), showing that the fingertip has the greatest 2D WS areas when the PIP joint is constrained to about 50°. Furthermore, Figure 2.5(b) shows that the design index pertaining to the aspect ratio of the 2D WS, I_a, exhibited increasing values until the PIP joint was 60°, when the 2D WS was most evenly distributed. In addition, the design index pertaining to the maximum distance of fingertip reach, I_D, in Figure 2.5(c), presented a reduction of about 0 to 10% as the PIP joint constraint angle increased from 0° to 60°.

2.4.4 Comparison of experimental and theoretical design indices

Model and experimental results of one subject (subject no. 4) were used in the assessment of 2D WS attributes using three design indices. The I_A index, with constrained PIP joint is plotted in Figure 2.6(a), indicating that the the greatest 2D WS areas are obtained when the PIP joint is constrained to about 50°. Moreover, Figure 2.6(b) shows that the design index pertaining to the aspect ratio of the 2D WS, I_a, exhibited increasing model values until the PIP joint was 60°, when the 2D WS was most evenly distributed. In contrast, experimental values of I_a increased until a maximum value was reached when the PIP joint was 50°. In addition, the design index pertaining to the maximum distance of fingertip reach, I_D, is presented in Figure 2.6(c). Experimental and model results of I_D indicated that the maximum distance of fingertip reach was reduced by 10% when the PIP joint constraint angle was constrained to 60° of flexion.

In this study, there were discrepancies between the experimental and model results of the 2D WS attributes. Those discrepancies, in addition to being caused by variations in

the ROM of the MCP and DIP joints, can be accounted for only considering finger motions in the FE plane. Small rotations of the MCP joint in the AA plane were neglected during experimental WS generation.

2.4.5 Comparison of experimental and theoretical weighted-sum criterion

Information of the design indices can be combined to determine an optimal constraint angle among the attributes considered (see Section 2.2.2). Various scenarios were presented with different sets of weighting factors for trade-off among three indices. Even though an arbitrary choice of weighting factors was used to illustrate the application of the weighted-sum criterion, these values could be selected to represent aspects such as cosmetic appearance or functionality. For instance, if emphasis in cosmetic appearance were considered, the choice of weighting factors with a penalty on large maximum distance of fingertip reach, I_D, would customize the selection of the PIP constraint angle for such purpose. Similarly, if the emphasis were in consideration of precision manipulation (e.g., writing, key insertion, or picking up and holding a very fine object) only, $\alpha_A = \alpha_a$ and $\alpha_D = 0$ may be a good choice to estimate an efficient PIP constraint angle that meets the criterion. Further investigations are required to relate weighting factors to functional and aesthetic aspects.

2.4.6 Limitations

While this research presented a kinematic model to assess the 2D WS attributes of a constrained finger, the model has limitations. Coupling mechanisms between the DIP and PIP joint were neglected when the PIP joint was constrained. Experimental results suggested that the PIP joint constraint angle affected the active ROM of the DIP joint. Likewise, intra-coupling mechanisms were not considered. The relative position of the digits seemed to have a small influence on the active ROM of the MCP joint during experimental

WS generation.

Although a perfect immobilization of the PIP joint was not possible due to skin movement, custom-made thermoplastic splints constrained the range of motion of the PIP joint to less than 5°. PIP joint constraint angles greater than 60° led to significant accumulation of skin in the volar aspects at the level of the index finger's proximal and middle phalanges. Thus, splint constraint angles greater than 60° did not restrict the motion of the PIP joint properly and were not considered in this experimental study.

A complete finger functioning cannot be described only from the viewpoint of kinematics, but also kinetics. Force exertion and joint torque contributions must be included to fully understand and assess the finger WS under imposed PIP joint constraints. Moreover, diseases that lead to arthrodesis are typically associated with adjacent joint impairment, such as arthritis at other joints and impaired muscle function. These factors were not considered. Further study is needed to identify the effect of the index finger PIP joint arthrodesis on hand function using standardized tests and during daily activities.

2.5 Summary

In the chapter, we present a systematic approach, based on the kinematics of fingers, to allow surgeons and physicians to determine the optimal constraint angle for arthrodesis operation to fuse the joints of a finger. This methodology utilizes the kinematic modeling of finger with analytical equations that will allow surgeons, physicians, and therapists to systematically understand the workspace attributes of a finger before a constraint angle is imposed, which has the advantage over prevailing *ad hoc* approaches. In addition, such arthrodesis can be customized for individual patients based on optimization of relevant indices to enhance the quality of life after surgery or during rehabilitation. The theoretical and experimental results suggest that the optimal PIP arthrodesis angles of the index finger are between 40° and 50° of flexion for design indices weighted equally.

Chapter 3

Experimental Study of the Optimal Angle for Arthrodesis of Fingers Based on Kinematic Analysis with Tip-pinch Manipulation

3.1 Introduction

Rheumatoid arthritis and osteoarthritis may lead to painful instability of fingers, making movement and even simple tasks difficult to perform. Symptomatic cases of hand osteoarthritis is a major public health concern reported for 5-25% of the population [18, 41]. This pathology induces a degradation of articular cartilage and surronding tissues resulting in loss of grip strength, reduce range of motion, severe pain, and other impairments regarding daily tasks [18, 41]. Conservative treatment with nonsteroidal anti-inflammatory drugs, steroids injections, splinting and therapy may relieve symptoms temporarily. Nonetheless, once these treatment options fail, patients may require a more invasive treatment to relieve their symptoms [41, 45, 52]. Arthrodesis, an artificial induction of joint ossification between two bones via surgery, provides a pain-free stable joint but sacrifices motion after the surgery [5, 32, 37, 41, 51]. Although the impact of arthrodesis on hand and finger function remains a matter of debate among surgeons, preoperative planning has to include a decision on the appropriate angle for arthrodesis [24, 25, 45, 51, 52, 3]. Obviously, constraining a finger joint reduces functionality by limiting the ability to perform important everyday tasks such as writing, delivering medication, key-insertion, and among others.

The objective of this research is to study a methodology for determining an optimal PIP constraint angle based on the maximization of the range of motion (ROM) of the joints and the manipulability of finger under imposed PIP joint constraint angles. A precision tip-pinch manipulation task was used to analyze how the imposed PIP constraint angles affect the ability for finger to manipulate objects among subjects in three selected postures.

3.1.1 Literature review

Studies on the combined finger manipulability of the index finger and thumb [53], the hand functional changes due to simulated proximal interphalangeal (PIP) of all fingers [51], the influence of the PIP joint fusion on precision pinch kinematics [15], and the measures of workspace attributes under simulated PIP joint arthrodesis of the index finger [3],were reviewed in order to enable us to place our work in perspective with respect to existing research in these fields. While these studies have significantly contributed to the understanding of finger and hand movement capabilities, there has not been an investigation on how the ROM of the joints and precision tip-pinch manipulation of a constrained finger are affected under finger joint arthrodesis. Precision manipulation, the hallmark of human's superior dexterity, is key to the ability to perform a large number of daily tasks such as writing, key insertion, or picking up and holding a very fine object like a pill (medication) or pin [3, 6, 53]. Consequently, precision manipulation under imposed joint constraints needs to be investigated in order to make more informed decisions on the appropriate angle for arthrodesis.

In this article, a kinematic evaluation was conducted on the index finger to determine the optimal PIP joint arthrodesis angles for precision in tip-pinch manipulation. Precision tip-pinch manipulation, involving repositioning a fine object in the fingertips, is used in everyday tasks [6]. The manipulability of a finger can be regarded as the ease of arbitrarily changing the position and orientation of the distal segment (phalanx) of the fingertip [54]. The manipulability of a finger in flexion-extension is explained by the shape and posture of

the manipulability ellipse in the flexion-extension plane [53].

3.2 Theoretical modeling and experimental validation

3.2.1 Kinematic model and manipulability

A kinematic model of the index finger, previously developed by the authors [3], was used to investigate manipulability. The kinematics of an open chain, such as the index finger, is shown in Figure 3.1. Equation (3.1) describes the Cartesian coordinates (x_{tip}, y_{tip}, and z_{tip}) of the fingertip as a function of the joint angles. The Cartesian coordinates of the fingertip are determined with respect to frame $\{0\}$, whose origin coincides with the center of rotation of the MCP joint, and the x_0-axis is along the longest axis of the metacarpal bone in the distal direction, as shown in Figure 3.1(a).

$$\begin{cases} x_{tip} = & c_1\left(l_1c_2 + l_2c_{23} + l_3c_{234}\right) \\ y_{tip} = & s_1\left(l_1c_2 + l_2c_{23} + l_3c_{234}\right) \\ z_{tip} = & -l_1s_2 - l_2s_{23} - l_3s_{234} \end{cases} \tag{3.1}$$

where c_{ijk} and s_{ijk} are $\cos\left(\theta_i + \theta_j + \theta_k\right)$ and $\sin\left(\theta_i + \theta_j + \theta_k\right)$, respectively. The angles θ_1, θ_2, θ_3, and θ_4 are the angles of rotation with respect to the MCP abduction-adduction, and MCP, PIP, and distal interphalangel (DIP) flexion-extension joint axes, respectively, as shown in Figure 3.1(b). The parameters l_1, l_2, and l_3 are the segment lengths of the proximal, middle, and distal phalanges, respectively. To obtain the model depicted by equation. (3.1), it is necessary to determine the joint angles and segment lengths of the index finger.

The Jacobian matrix, denoted as $\mathbf{J}_\theta$, relates the infinitesimal displacement at the tip of the finger in the Cartesian space with respect to the change of joint angles. Equation (3.2) defines the Jacobin matrix.

$$\delta\mathbf{p}_{tip} = \mathbf{J}_\theta \delta\Theta \tag{3.2}$$

where $\delta\mathbf{p}_{tip} = [\delta x_{tip}\ \delta z_{tip}]^T$ and $\delta\Theta = [\delta\theta_2\ \delta\theta_3\ \delta\theta_4]^T$ are the infinitesimal changes of the

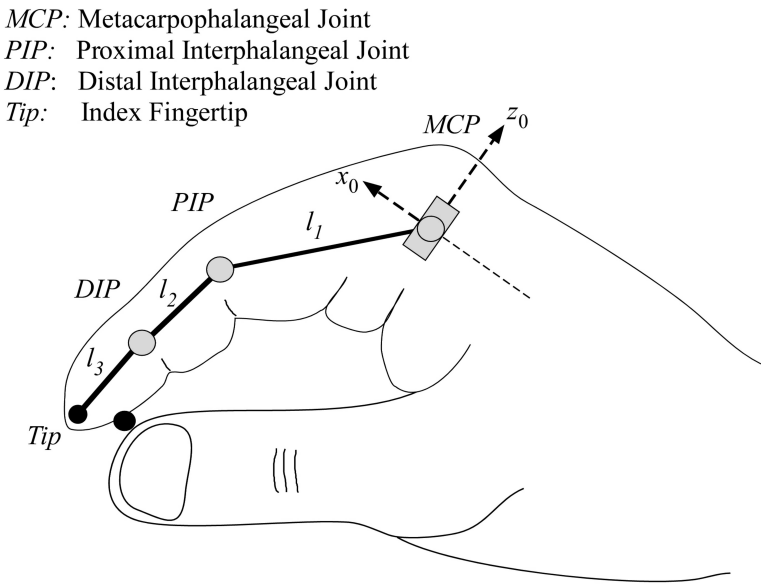

(a) Segment model of the index finger

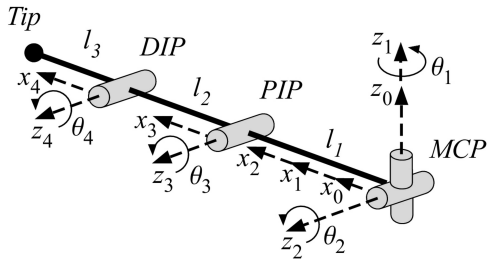

(b) Initial posture of the index finger model

Figure 3.1: Schematic illustration of the segment model of the index finger during tip-pinch manipulation.

Cartesian and joint coordinates, respectively.

The manipulability ellipse at the tip of the index finger in the flexion-extension plane (*xz*-plane) was calculated by applying the singular value decomposition to the Jacobian matrix, as follows

$$\mathbf{J}_\theta = \mathbf{U}\Sigma\mathbf{V}^T \tag{3.3}$$

where $\mathbf{U}$ and $\mathbf{V}$ are 2×2 and 3×3 orthogonal matrices, respectively, and Σ is a 2×3 matrix defined as

$$\Sigma = \left[\begin{array}{cc|c} \sigma_1 & 0 & 0 \\ 0 & \sigma_2 & 0 \end{array}\right] \tag{3.4}$$

The scalars σ_1 and σ_2 in equation (3.4) are the *singular values* of $\mathbf{J}_\theta$, which are equal to the square root of the eigenvalues of the matrix $\mathbf{J}_\theta\mathbf{J}_\theta^T$. The singular values, σ_1 and σ_2, are ordered as $\sigma_1 \geq \sigma_2 \geq 0$. In addition, setting $\mathbf{u_1}$ and $\mathbf{u_2}$ as the column vectors of $\mathbf{U}$, the semi axes of the manipulability ellipsoid are $\sigma_1\mathbf{u_1}$ and $\sigma_2\mathbf{u_2}$.

The manipulability measure, *w*, is defined as [54]

$$w = \sqrt{\det\left(\mathbf{J}_\theta\mathbf{J}_\theta^\mathbf{T}\right)} = \sqrt{\det\left(\Sigma\Sigma^T\right)} = \sigma_1\sigma_2 \tag{3.5}$$

which relates to the area of the manipulability ellipse. The measure *w* is used to compare the ellipses at selected tip-pinch manipulation postures for imposed PIP joint constraints.

3.2.2 Manipulabilty evaluation

Three quantities of evaluation were investigated under imposed PIP joint constraint angles across all subjects to access the manipulability. They are: (1) the shapes of manipulability ellipses, (2) manipulability measures, and (3) the direction angle of major axis of the manipulability ellipse of the index finger in tip-pinch manipulation postures.

The assumptions made to compute manipulability in this study include the main movement was flexion-extension, single-point contact without friction between the fingertips and object, and quasistatic manipulation [20, 21, 22].

Figure 3.2 shows an example of the manipulability ellipse at the tip of the PIP joint constrained index finger for a precision tip-pinch manipulation posture. Parameters, including segment lengths and joint angles, were obtained from experimental measurements (see Section 3.2.6). The finger PIP joint was constrained to 30°. The x-z plane is the flexion-extension plane of the index finger. The tip of the index finger is used as the origin of the x'-z' coordinate system, parallel to the x-z coordinate system, of the manipulability ellipses. In order to analyze manipulability ellipses, the following three measures are defined.

(1) The shape of the manipulability ellipse was investigated by measuring the ratio of the radii of its minor axis (σ_2) to the major axis (σ_1) as defined in equation (3.6), see also Figure 3.2.

$$r = \frac{\sigma_2}{\sigma_1} \tag{3.6}$$

(2) The manipulability measure, $w = \sigma_1\sigma_2$, relating to the area of the manipulability ellipse, was compared for distinct PIP constraint angles using equation (3.5).

(3) The major-axis angle, α, measured counterclockwise with respect to the x'-axis, is utilized to indicate the direction which is easy to manipulate the fingertip under the imposed PIP joint constraints, as shown in Figure 3.2.

3.2.3 Participants

Five male and two female right-handed subjects, aged from 25 to 34 years old, volunteered in this study. All participants had no previous history of upper extremity disorders. Prior to the data collection, subjects signed an informed consent document approved by the Stony Brook University Institutional Review Board.

3.2.4 Data acquisition

A ten-camera motion capture system (Vicon MX, Oxford, UK) at a sample frequency of 100 Hz, was arranged in a 2m $\times$ 2m square region for data collection. Three dimensional

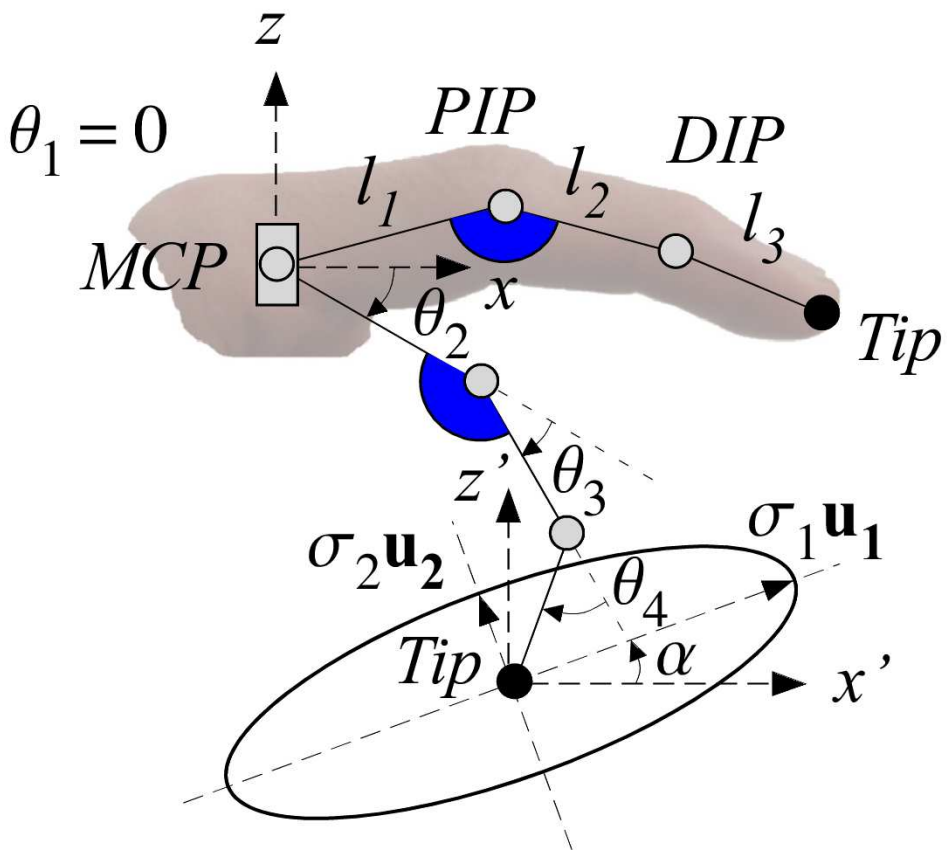

Figure 3.2: Schematic illustration of a manipulability ellipse at a selected posture of the index finger during tip-pinch manipulation indicated by the 3-segment kinematic model, with the PIP joint constrained at 30°. The segment lengths of the subject are as follows: $l_1 = 44$ mm, $l_2 = 23$ mm, and $l_3 = 19$ mm.

accuracy measurement was determined to be well within 0.5 mm [3]. Seven reflective markers were attached to the dorsal aspects of the index finger and hand with double-sided tape [3]. Figure 3.3 illustrates the marker placements for the 7×9.5 mm spherical markers. An 80-mm light-extension frame with two markers was built and attached to the tip of the index finger in order to avoid marker occlusion during task motions. Custom-made thermoplastic splints were used to constraint the PIP joint at six distinct angles, as illustrated in Figure 3.3. An experimenter customized each PIP splint based on each individual finger length. Manual goniometers were used to verify the constraint angles and adjust the splints accordingly [3]. Despite the fact a perfect immobilization of the PIP joint was not possible due to skin movement, custom-made thermoplastic splints constrained the range of motion of the PIP joint to about 5°.

3.2.5 Experimental setup

The wrist was extended at an angle of 30°, while the forearm comfortably rested on a height-adjustable table during experiments. All fingers were flexed and relaxed with exception of the index finger and thumb, which performed the movements, as instructed. First, flexion-extension motions were used to estimate finger parameters [3]. Next, the subjects were instructed to hold a pin between the index finger and thumb, without removing or replacing the contact, and perform repeated motions of the digits allowing extension (Posture 1), intermediate (Posture 2), and flexion postures (Posture 3), as presented in Figure 3.3 [53]. At least five cycles were recorded for each prescribed motion. Repetitive motions were measured under two conditions: (1) non-constrained finger, and (2) with the index finger PIP joint constrained to 0°, 20°, 30°, 40°, 50°, and 60° of flexion. Participants performed a 20-second trial in each task. Each subject performed a practice trial with the non-constrained and constrained finger before data recording.

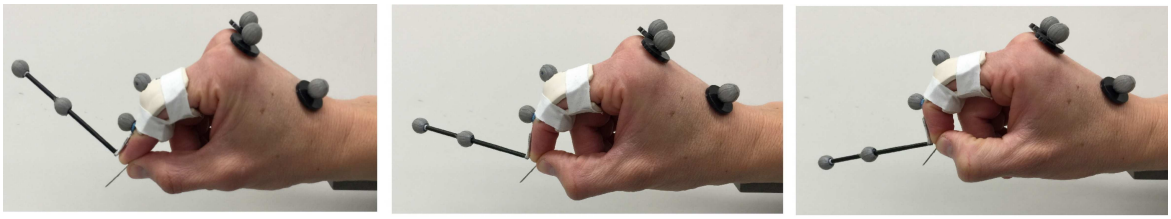

(a) Posture 1
Extension

(b) Posture 2
Intermediate

(c) Posture 3
Flexion

Figure 3.3: Tip-pinch manipulation postures of measurement of the index finger with 9.5-mm spherical markers attached and the PIP joint splinted. The 80-mm light extension frame with two markers attached at the fingertip prevented marker occlusion during manipulation of a pin.

3.2.6 Data processing

Each marker was taken as a set of three points indicating the relative x, y, and z coordinates of the marker in space, relative to the Vicon coordinate system, or global coordinate system. A local coordinate system is then embedded in the hand plane defined by the marker model, and subsequent planes and vectors are defined relative to the hand plane. Data were then processed with MATLAB software package. Since finger motions did not exceed 5 cycles per second, data were filtered using a second-order Butterworth low-pass filter with 20 Hz cut-off frequency to reduce high-frequency noise. Three vectors, one for each phalanx, were created using the markers placed on the MCP, PIP, and DIP joints, as well as a virtual marker at the fingertip created 40 mm apart from the middle marker of the extension frame and towards the fingertip. Joint angles were calculated according to the method presented by [3]. Only angles in the flexion-extension plane were considered. Small rotations in other directions due to non-constant interphalangeal joint axes were neglected. Estimation of segment lengths, as well as the center of rotation of the finger joints were obtained by applying the least squares fitting to marker trajectories during flexion-extension tasks [3, 53]. The first two cycles of each trial were excluded from data analysis. The joint angles were analyzed at the three selected postures shown in Figure 3.3. Tip-pinch manipulation postures 1, 3, and 2 were identified at instants when the DIP (θ_4) joint angle was minimum, maximum, and the average between maximum and minimum, respectively. Average data of three cycles were selected for analysis. Typically, results of cycles were consistent and could be selected arbitrarily. The approximate duration of the precision tip-pinch manipulation cycle was between two and three seconds.

3.2.7 Statistical analysis

The ROM of the MCP and DIP joints of the non-constrained and constrained finger was analyzed among subjects. In addition, finger postures and manipulability ellipses were obtained and analyzed for each PIP joint constraint angle among subjects. Statistical

significance of the effect of the imposed PIP joint constraint angles was analyzed with repeated measures across all subjects using one-way analysis of variance (ANOVA). The PIP constraint angles (splints) were randomized and assigned by the experimenter. If assumptions of normality and equal variance were not met, then the analysis of variance of ranks was utilized. If the obtained p-value was less than the significant level ($p < 0.05$), then significant differences were assumed.

3.3 Results

3.3.1 Paramenter estimation

The estimation of the segment lengths of the index finger for all subjects (mean $\pm$ S.D.) were $l_1 = 42 \pm 4$ mm and $l_2 = 23 \pm 2$ mm, and the estimation of distance from the DIP joint center to the marker point on the fingertip was $l_3 = 19 \pm 1$ mm.

3.3.2 Functional ROM of the joints

The functional ROM of the MCP joint of the index finger varied significantly ($p = 3.71 \times 10^{-10}$) for the imposed PIP joint constraint angles, as shown in Figure 3.4. A significant increment of the ROM of the MCP joint was observed as the PIP joint constraint angle increased from 0° to 30° of flexion (approximately three times as observed in Figure 3.4). The centers of the bar of the MCP joint decreased as the PIP joint was constrained from 40° to 60° of flexion; nonetheless, small differences in the ROM of the MCP joint were observed (less than 10% as presented in Figure 3.4). The functional ROM of the DIP joint of the constrained and non-constrained index finger did not change significantly ($p = 0.11$) among subjects during tip-pinch manipulation, as shown in Figure 3.4. Similar to the ROM of the MCP joint, the ROM of the DIP joint slightly increased as the PIP joint constraint angle increased.

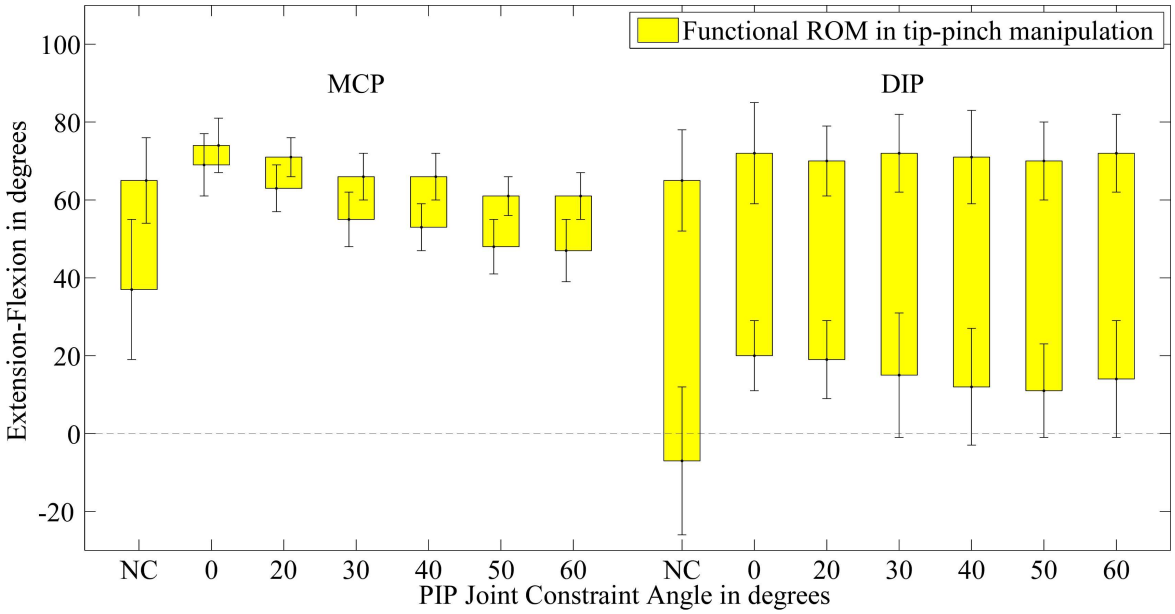

Figure 3.4: The average of the functional ROM of the MCP and DIP joints of the index finger of seven subjects when the PIP joint is non-constrained (NC) and constrained to selected angles of 0°, 20°, 30°, 40°, 50°, and 60° during the tip-pinch manipulation.

3.3.3 Manipulability

Manipulability ellipses at the three selected postures of the index during tip-pinch manipulation were investigated across subjects under simulated PIP joint arthrodesis. Figure 3.5 shows the result for tip pinch manipulation postures of a typical subject (subject no. 7) for the sake of clarity in illustration. Other subject present similar results. The shape of the manipulability ellipses at the fingertip is more evenly distributed as the finger postures change from extension to flexion postures, as indicated in Figure 3.5.

The three quantities of evaluation, r, w, and α, were calculated across all subjects and are illustrated in Figure 3.6, with comparisons among the three postures. The results are summarized in the following.

The ratio of the minor axis to the major axis of the manipulability ellipse, r, of the index finger changes significantly (posture 1: $p = 0.0003$, posture 2: $p = 5.81 \times 10^{-7}$, and posture 3: $p = 5.33 \times 10^{-8}$) under the imposed PIP joint constraints in the three tip-pinch manipulation postures. Figure 3.6(a) shows that the greater the PIP joint constraint angle, the more evenly distributed the shapes of the manipulability ellipses are at the fingertip.

Manipulability measures, w, do not differ significantly (posture 1: $p = 0.25$, posture 2: $p = 0.53$, and posture 3: $p = 0.12$) under the imposed PIP joint constraint angles in the three tip-pinch manipulation postures selected, as illustrated in Figures 3.6(b). Results showed that manipulability measures, w, have the largest values when the PIP joint angle was constrained to 50°, 60°, and 20° at tip-pinch manipulation postures 1, 2, and 3, respectively, as shown in Figure 3.6(b).

The direction angles of major axis of the manipulability ellipse of the index finger, α, differ significantly (posture 1: $p = 0.0001$, and posture 2: $p = 0.038$) at extension and intermediate postures, yet it does not differ significantly (posture 3: $p = 0.9$) at flexion postures, as shown in Figure 3.6(c). At posture 1 and 2, the direction angles of major axis of the manipulability ellipse, α, increased as the imposed PIP joint constraint angle increased from 30° to 60°, as shown in Figure 3.6(c). At posture 3, the angle, α, has the

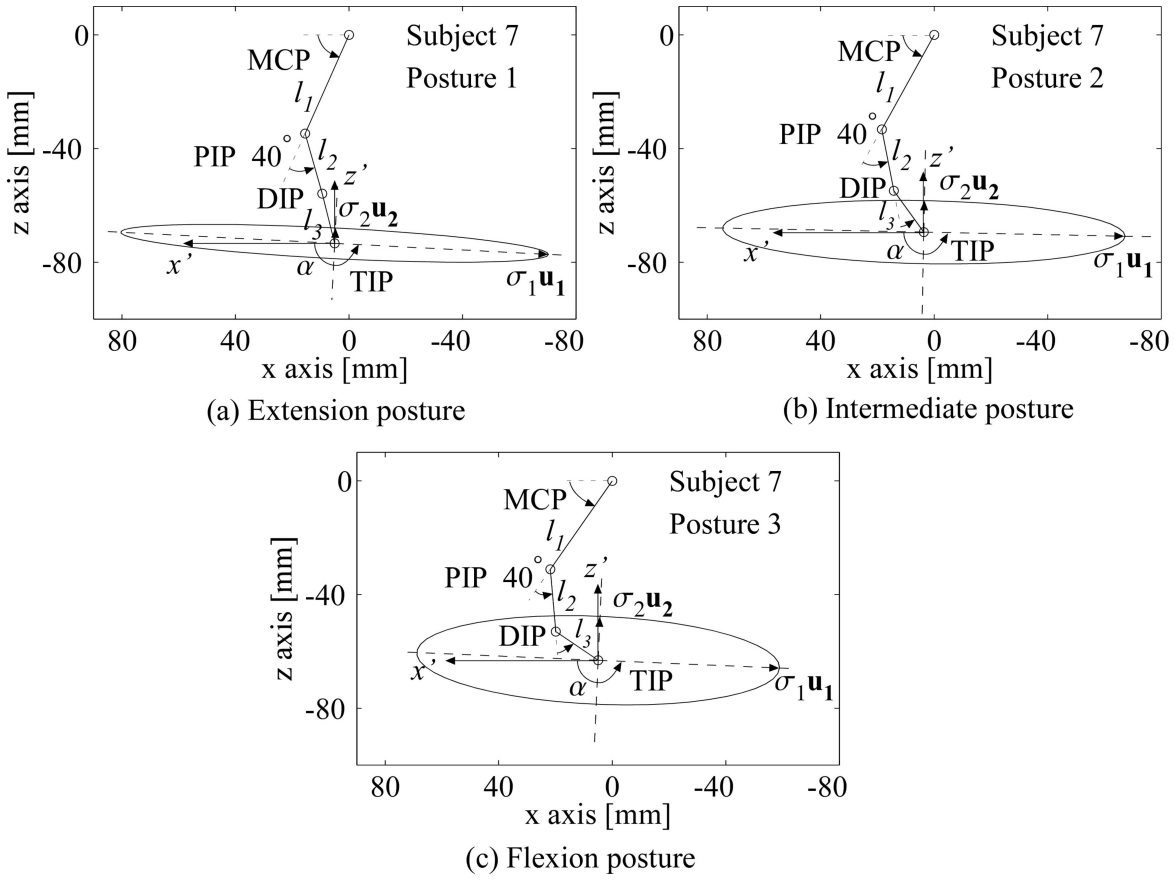

Figure 3.5: Schematic illustration of manipulability ellipses at three selected postures of the index finger during tip-pinch manipulation indicated by the 3-segment kinematic model, with the PIP joint constrained at 40°. For simplicity and clarity of presentation, the data of one subject (subject no. 7) are illustrated here. Other subjects have similar illustrations. The segment lengths of the subject are as follows: $l_1 = 38$ mm, $l_2 = 22$ mm, and $l_3 = 18$ mm.

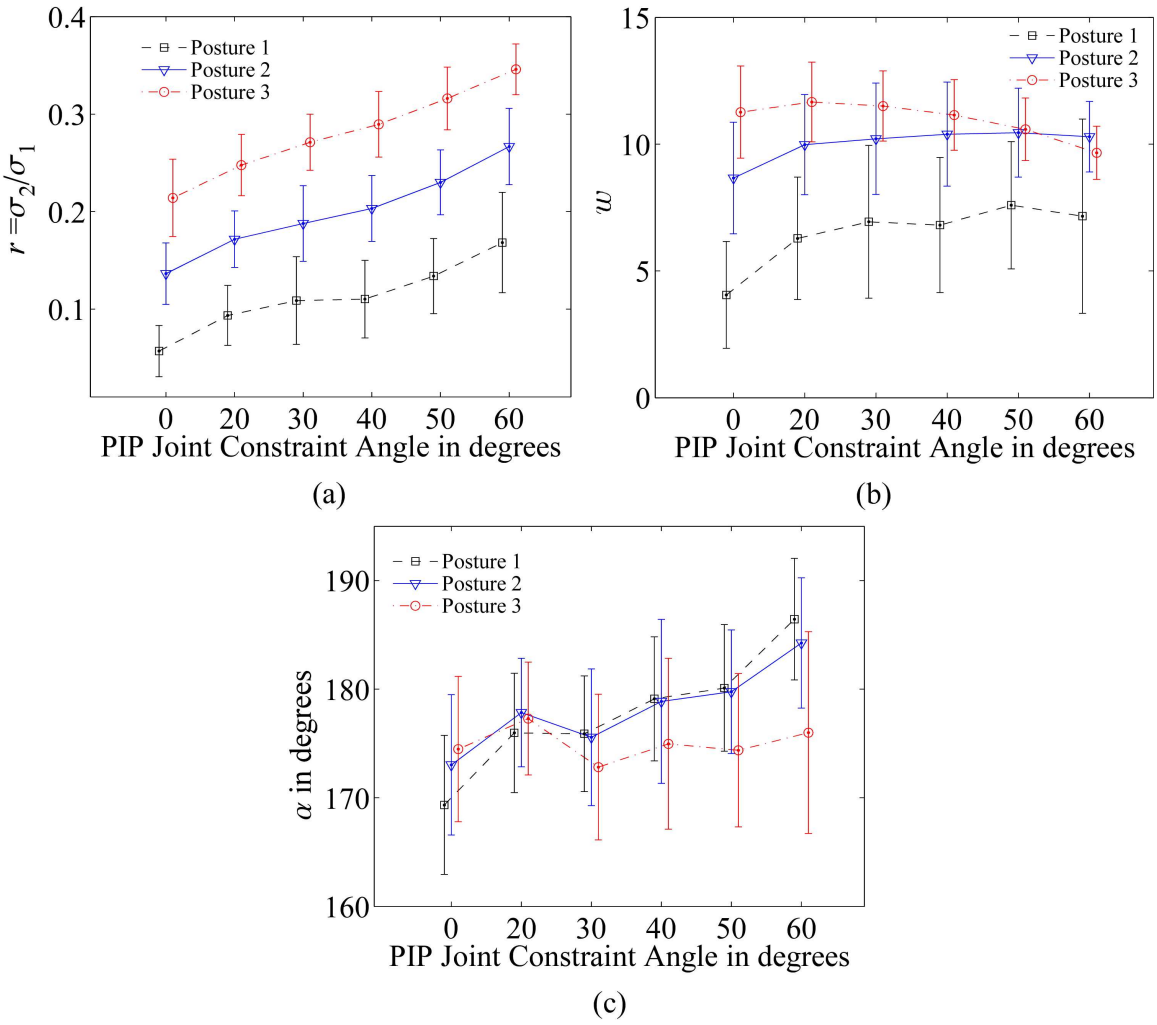

Figure 3.6: The average of (a) the ratio of the radii of the minor to major axes of the manipulabililty ellipse, $r = \frac{\sigma_2}{\sigma_1}$, (b) the manipulability measure, $w = \sigma_1\sigma_2$, and (c) the manipulability ellipse major-axis angle α.

largest value with the PIP joint constrained at 20°, as shown in Figure 3.6(c).

3.4 Discussions

In this study, we investigated precision tip-pinch manipulation of the index finger under simulated PIP arthrodesis at prescribed angles using the ROM of the joints and a kinematic model that represents the finger as a serial kinematic chain. The results obtained in this study are based on both experimental analysis and the theoretical model. Theoretical results are relevant because they provide more accurate analytical model, instead of an *ad hoc* approach, and better physical insights. In the following sections, we discuss the results of the study.

3.4.1 Functional ROM of the joints

The functional ROM of the MCP and DIP joints of the index finger are analyzed when the PIP joint is either non-constrained or constrained at 0°, 20°, 30°, 40°, 50°, and 60° of flexion. The functional ROM of the MCP joint is significantly reduced by the imposed PIP joint constraint angles, as shown in Figure 3.4. The functional ROM of the MCP and DIP joints of the constrained finger slightly increases as the PIP joint constraint angle increases. This result, consistent with results of previous studies [51], indicates that the precision of manipulation increases as the PIP joint constraint angle is increased during tip-pinch manipulation. Similarly, the result of the functional ROM of the MCP and DIP joints shows that the constrained index finger can attain postures close to those of the non-constrained finger during tip-pinch manipulation when the PIP joint is constrained to angles between 40° to 60° of flexion. Although these findings concur with previous studies reporting the impact of PIP joint arthrodesis on finger and hand function [15, 51], they show a limited compensatory motion at the MCP joint when a PIP joint constraint is imposed during a tip-pinch manipulation task. In addition, the results of the ROM of the joints of the constrained finger suggest that the functional workspace [3, 6] of the fingertip

in tip-pinch manipulation is reduced when the PIP joint is constrained to 0° and 20°.

3.4.2 Manipulabilty

Figure 3.5 illustrates the calculation of the manipulability ellipses at the three selected postures for one subject with the finger PIP joint constrained to 40°. This result indicates that the shapes of the manipulability ellipses are best distributed at the flexion posture (Posture 3). In addition, the size of the manipulability ellipse and the angle α have small variations among postures, as illustrated in Figures 3.5(a), 3.5(b), and 3.5(c). Similar quantitative results of the manipulability are observed across all subjects, as shown in Figure 3.6.

3.4.3 The three measures, *r*, *w*, and α

Even though the ratio of the radii of the minor axis to major axis the manipulability ellipses, *r*, increases from posture 1 to posture 3, as shown in Figure 3.6(a), the manipulability measures, *w*, and the angle, α, do not always increase from posture 1 to posture 3 for a specific PIP joint constraint angle, as shown in Figure 3.6(b) and 3.6(c). These results of the PIP joint constrained finger are consistent with previous studies reporting the tip-pinch manipulation between the non-constrained index finger and thumb [53].

There are significant differences among the subjects for the ratio *r* of the index finger under the imposed PIP joint constraints in the three tip-pinch manipulation postures. The shapes of the manipulability ellipses are more evenly distributed [1] for the three tip-pinch manipulation postures considered when the PIP joint is constrained at 50° to 60° of flexion.

Our results suggest that PIP arthrodesis angles at 50° to 60° of flexion, having tip-pinch postures with the shape of the manipulability ellipses at the fingertip more evenly distributed, lead to the optimal performance of the finger in manipulation and grasping of fine objects. Though, being analytically and systematically obtained based on theoretical

[1] Evenly distributed manipulation ellipse with higher ratio *r* indicates better manipulability.

modeling of the finger, these results are consistent with previous works using prevailing *ad hoc* approaches. Indeed, several researchers have reported that a PIP joint arthrodesis at 40° to 50° of flexion facilitates grip strength and lead to more natural precision pinch postures [14, 15, 51].

In this study, we quantified the PIP arthrodesis angle that optimizes tip-pinch manipulation. It is known that the selection of the arthrodesis angle is an optimization which takes into account the trade-offs between conflicting objectives. Findings of this study can be compared to other finger aspects or attributes such as the ones previously presented by the authors in [3] to select the constraint angle that best satisfies those conditions.

3.4.4 Limitations

Although the results of manipulability of the constrained index finger are calculated from real finger postures, they may not replicate the values of manipulability of the real finger completely because skin compliance at the fingertip in tip-pinch manipulation was not considered. In addition, even though the shapes of manipulability ellipses are independent of the joints and tip velocities, finger coordination and dexterity, affected by joints and tip velocities, were not considered. Nonetheless, this theoretical analysis provides insights into understanding how manipulabilities were affected during tip-pinch manipulation when the PIP joint was constrained to selected angles.

3.5 Summary

A study using the kinematic modeling with the experimental measurements utilizing the tip-pinch manipulation of the index finger under imposed PIP joint constraint angles was conducted. This study also presented a methodology using the ROM and manipulability in tip-pinch manipulation to evaluate the influence of different constrained PIP joint angles. Results suggest that a PIP joint constrained between 50° to 60° of flexion lead to a natural finger posture with more evenly distributed manipulability. In general, a similar

analysis can be applied to other fingers and joints so that constraint angles allowing optimal manipulation can be determined. This systematic and analytical methodology can help surgeons and physicians in determining PIP arthrodesis angles that allow fingers after surgery to be more suitable for precision tip-pinch manipulation tasks.

Chapter 4

Kinematic Modeling for the Optimal Joint Constraint Angles of Fingers

4.1 Introduction

Partial or complete loss of the finger joint motions due to a disease or injury may require conservative treatment with nonsteroidal anti-inflammatory drugs, steroids injections, splinting, and hand therapy, or more invasive treatment with surgery and rehabilitation techniques which may involve restricting or reducing normal movement to relieve pain, create joint stability, and expedite the recovery process [41, 3]. Consequently, we would like to be able to predict finger joint constraint angles to optimize its capability of movement and manipulability. The index finger models developed in Chapters 2 and 3 can be applied to predict the optimal joint constraint angles. The finger workspace (WS), and manipulability measures are proposed to identify the joint constraint angle which is most suited for optimal finger motion. The finger models are applied to further investigate not only the two-dimmensional (2D) but also three-dimensional (3D) WS. In addition, manipulability of the constrained and unconstrained fingers are analyzed under distinct joint constraint angles. Constraint angles are investigated for both the index finger distal interphalangeal (DIP) and proximal interphalangeal (PIP) joints.

4.2 Application of kinematic model of finger

In the following, a systematic approach, based on the application of the kinematic model of the finger, is used to determine the 2D and 3D WS of the index finger under three conditions: (1) without constraining the finger joints , (2) with the PIP joint constrained to selected angles, and (3) with the DIP joint constrained to prescribed angles. Examples applying specific numbers and parameters are utilized here to illustrate the theoretical analysis.

4.2.1 WS of the unconstrained finger

As mentioned in Section 2.2.1.1, the index finger contains tendinous mechanisms that are essential for proper control. The coupling relation between the DIP and PIP joints, expressed as $\theta_4 \leq \frac{2}{3}\theta_3$, has been considered in previous finger models [29], and is included in the model of the unconstrained finger.

Equation (2.1) with model parameters and the coupling relation between the DIP and PIP joints, as well as the ROM of the joints describe the 2D WS boundaries of the unconstrained finger. Model parameters were obtained from experimental measurements (see Section 2.2.6).

The 2D WS of the finger model is presented in Figure 4.1(a). The parametric expressions of the 2D WS boundaries of the example presented in Figure 4.1(a) are described as

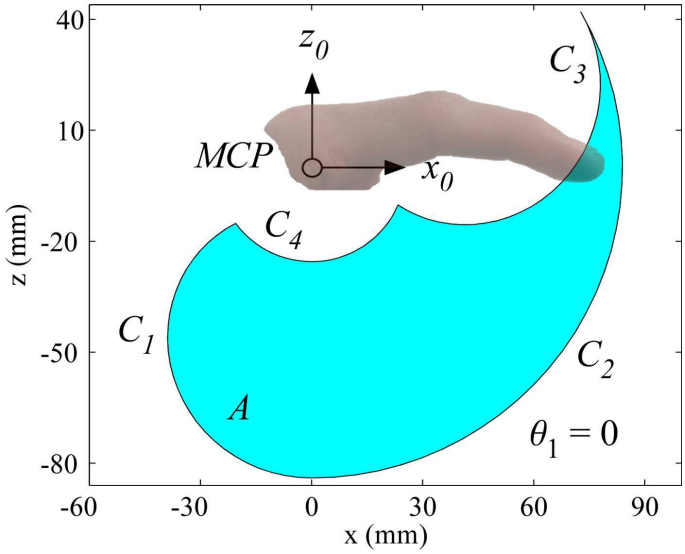

(a) 2D WS

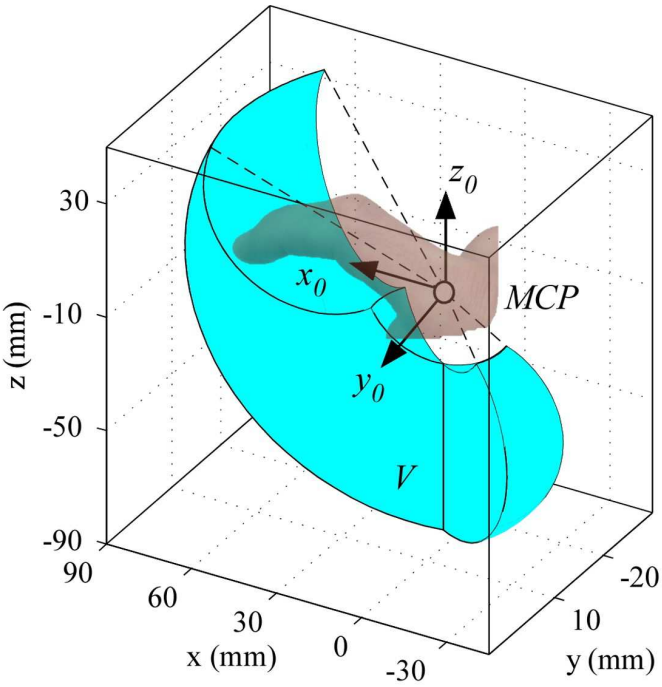

(b) 3D WS

Figure 4.1: (a) The model representation of the 2D WS of the unconstrained index finger. The model parameters are as follows: $l_1 = 42$ mm, $l_2 = 23$ mm, and $l_3 = 19$ mm. The ROM of the joints are: $-30^\circ \leq \theta_1 \leq 10^\circ$,$-30^\circ \leq \theta_2 \leq 90^\circ$, $0^\circ \leq \theta_3 \leq 110^\circ$, and $0^\circ \leq \theta_4 \leq 80^\circ$. The coupling relation between the PIP and DIP joint is $\theta_4 \leq \frac{2}{3}\theta_3$. The 2D WS boundaries are represented by curves C_1, C_2, C_3, and C_4. The WS area is $A = 6,710$ mm^2. (b) The 3D WS of the unconstrained index finger with a volume $V = 151,830$ mm^3.

$$
C_1 : \begin{cases} x_{tip} = & l_1 \cos(90^\circ) \\ & +l_2 \cos(90^\circ + \theta_3) \\ & +l_3 \cos(90^\circ + \theta_3 + \frac{2}{3}\theta_3), \\ y_{tip} = & 0, \\ z_{tip} = & -l_1 \sin(90^\circ) \\ & -l_2 \sin(90^\circ + \theta_3) \\ & -l_3 \sin(90^\circ + \theta_3 + \frac{2}{3}\theta_3), \end{cases} \quad \text{with} \quad 0^\circ \leq \theta_3 \leq 110^\circ \tag{4.1}
$$

$$
C_2 : \begin{cases} x_{tip} = & l_1 \cos(\theta_2) \\ & +l_2 \cos(\theta_2 + 0^\circ) \\ & +l_3 \cos(\theta_2 + 0^\circ + \frac{2}{3}0^\circ), \\ y_{tip} = & 0, \\ z_{tip} = & -l_1 \sin(\theta_2) \\ & -l_2 \sin(\theta_2 + 0^\circ) \\ & -l_3 \sin(\theta_2 + 0^\circ + \frac{2}{3}0^\circ), \end{cases} \quad \text{with} \quad -30^\circ \leq \theta_2 \leq 90^\circ \tag{4.2}
$$

$$
C_3 : \begin{cases} x_{tip} = & l_1 \cos(-30^\circ) \\ & +l_2 \cos(-30^\circ + \theta_3) \\ & +l_3 \cos(-30^\circ + \theta_3 + \frac{2}{3}\theta_3), \\ y_{tip} = & 0, \\ z_{tip} = & -l_1 \sin(-30^\circ) \\ & -l_2 \sin(-30^\circ + \theta_3) \\ & -l_3 \sin(-30^\circ + \theta_3 + \frac{2}{3}\theta_3), \end{cases} \quad \text{with} \quad 0^\circ \leq \theta_3 \leq 110^\circ \tag{4.3}
$$

$$
C_4 : \begin{cases} x_{tip} = & l_1 \cos(\theta_2) \\ & +l_2 \cos(\theta_2 + 110^\circ) \\ & +l_3 \cos(\theta_2 + 110^\circ + \frac{2}{3} 110^\circ), \\ y_{tip} = & 0, \\ z_{tip} = & -l_1 \sin(\theta_2) \\ & -l_2 \sin(\theta_2 + 110^\circ) \\ & -l_3 \sin(\theta_2 + 110^\circ + \frac{2}{3} 110^\circ), \end{cases} \quad \text{with} \quad -30^\circ \leq \theta_2 \leq 90^\circ \tag{4.4}
$$

The 3D WS of the finger model is presented in Figure 4.1(b). Since the model considers that the abduction-adduction (AA) axis of the MCP joint intersects the flexion-extension (FE) axis of the MCP joint at a right angle, the 3D WS is obtained by revolving the 2D WS about the AA joint axis of the MCP joint. The ROM of MCP joint about the AA axis obtained from experimental measurements is $-30^\circ \leq \theta_1 \leq 10^\circ$. When generating the 3D WS, the singularity[1] of AA axis of the MCP joint (z_0-axis) can be observed in Figure 4.1(b).

4.2.2 Manipulability of the unconstrained finger

Manipulability can be regarded as the ease of arbitrarily changing the position and orientation of the end-effector at the tip [54]. Manipulability *measure* and *ellipsoid* will be defined in this section to quantify the manipulability of the unconstrained index finger.

The manipulability measure w is defined as [54]

$$
w = \sqrt{\det\left(\mathbf{J}_\theta \mathbf{J}_\theta^{\mathbf{T}}\right)} \tag{4.5}
$$

where $\mathbf{J}_\theta$ is the Jacobian matrix. Employing the Jacobian matrix for the index finger, defined as $[dx\ dy\ dz]^T = \mathbf{J}_\theta [d\theta_1\ d\theta_2\ d\theta_3\ d\theta_4]^T$, we can derive

$$
w = |l_1 c_2 + l_2 c_{23} + l_3 c_{234}|\, \tilde{w}(\theta_2, \theta_3, \theta_4) \tag{4.6}
$$

[1] The singularity refers to exterior boundary of the WS. In Figure 4.1(b), the singularity is along the exterior surfaces of the 3D WS, where further extension of the finger reach becomes impossible: that is, the fingertip will lose ability to reach in certain directions.

where $\tilde{w}$ is the manipulability measure of the index finger which moves in the FE plane (xz-plane), defined as

$$\tilde{w}(\theta_2, \theta_3, \theta_4) = \sqrt{\det \tilde{\mathbf{J}}\tilde{\mathbf{J}}^{\mathbf{T}}} \tag{4.7}$$

where the reduced Jacobian $\tilde{\mathbf{J}}$ is defined as $[dx\, dz]^T = \tilde{\mathbf{J}}[d\theta_2\, d\theta_3\, d\theta_4]^T$, and is expressed as

$$\tilde{\mathbf{J}} = \begin{bmatrix} -l_1 s_2 - l_2 s_{23} - l_3 s_{234} & -l_2 s_{23} - l_2 s_{234} & -l_3 s_{234} \\ -l_1 c_2 - l_2 c_{23} - l_3 c_{234} & -l_2 c_{23} - l_2 c_{234} & -l_3 c_{234} \end{bmatrix} \tag{4.8}$$

Note that although the notations for the reduced Jacobian $\tilde{\mathbf{J}}$ and $\tilde{w}$ are different from those in Chapter 3, the definitions are exactly the same.

4.2.3 Manipulability ellipsoid

Next, we introduce the manipulability ellipsoid.

The Jacobian matrix of the index finger model considered typically has a maximum rank of three. Employing the singular-value decomposition (SVD), three singular values can be found corresponding to three basis axes. The three singular values are the semi-axes of the ellipsoid, with the principal axes along the three basis [54]. Let the SVD of the Jacobian matrix $\mathbf{J}_\theta$ be

$$\mathbf{J}_\theta = \mathbf{U}\Sigma\mathbf{V}^{\mathbf{T}} \tag{4.9}$$

where $\mathbf{U}$ and $\mathbf{V}$ are 3×3 and 4×4 orthogonal matrices, respectively, and Σ is and 3×4 matrix defined by

$$\Sigma = \left[\begin{array}{ccc|c} \sigma_1 & & \mathbf{0} & \\ & \ddots & & \mathbf{0} \\ \mathbf{0} & & \sigma_3 & \end{array}\right] \tag{4.10}$$

The scalars $\sigma_1, \sigma_2, \sigma_3$ are called the *singular values* of $\mathbf{J}_\theta$, which are equal to the square root of the eigenvalues of the matrix $\mathbf{J}_\theta\mathbf{J}_\theta^{\mathbf{T}}$. The singular values, $\sigma_1, \sigma_2, \sigma_3$, are ordered as, $\sigma_1 \geq \sigma_2 \geq \sigma_3 \geq 0$. The Jacobian matrix of the index finger, $\mathbf{J}_\theta$, is a 3×4 matrix with a rank of three. Hence, the manipulability ellipsoid of the index finger has three singular values

and three semi-axes. In addition, letting $\mathbf{u_1}$, $\mathbf{u_2}$, and $\mathbf{u_3}$ be the column vectors of $\mathbf{U}$, the semi-axes of the manipulability ellipsoid are $\sigma_1\mathbf{u_1}$, $\sigma_2\mathbf{u_2}$ and $\sigma_3\mathbf{u_3}$ [54].

Substitution of equation (4.9) into equation (4.5) results in

$$w = \sqrt{\det(\Sigma\Sigma^{\mathbf{T}})} = \sigma_1\sigma_2\sigma_3 \tag{4.11}$$

Equation (4.11) shows that the manipulability measure is the product of the singular values of the Jacobian matrix of the index finger [54]. It is important to note that the value of w of the index finger only depends on the angles of the MCP (θ_2), PIP (θ_3), and DIP (θ_4) joints, and does not depend on the angle of the MCP (θ_1) joint.

The Jacobian matrix, $\mathbf{J}_\theta$ with SVD, defines three singular values along three axes which defines an ellipsoid. This manipulability ellipsoid depicts the versatility of movement in all directions. For example, small singular value of σ_3 indicates that the finger's ability to move along the direction $\mathbf{u_3}$ is limited and constrained. For the sake of illustration, we will first consider the reduced number of DOF from 3D (in $\mathbf{J}_\theta$) to 2D (in $\tilde{\mathbf{J}}$) the FE plane (xz-plane) without considering θ_1. In this case, the manipulability ellipsoid is degenerated to an ellipse and easier to visualize. The Jacobian we consider in equation (4.8) for the 2D ellipse is a 2×3 matrix which typically has a rank of two. Consequently, the manipulability ellipse of the index finger that moves in the FE plane has two singular values and two semi-axes. Furthermore, equations (4.7) and (4.8) are used to calculate the 2D manipulability measure, $\tilde{w}$, of the index finger that moves in the FE plane. It can be shown that $\tilde{w}$ only depends on the angles of the PIP (θ_3) and DIP (θ_4) joints, and does not depend on the angle of the MCP (θ_2) joint. A plot of the 2D manipulability measure, $\tilde{w}$, is presented in Figure 4.2(a). Figure 4.2(b) presents several 2D manipulability ellipses with postures of the index finger when it moves along a line parallel to the z-axis. The 2D manipulability ellipses are calculated using the SVD method presented above.

The 2D manipulability can be compared using the following methodology, with $\sigma_1\mathbf{u_1}$ and $\sigma_2\mathbf{u_2}$. Six different postures are shown with corresponding ellipses in Figure 4.2(b). A magnified view of posture 3 is illustrated with $\sigma_1\mathbf{u_1}$ and $\sigma_2\mathbf{u_2}$ along the two principal

axes. Since the versatility of movement is related to the magnitude (area) and shape of the ellipse, the ellipse with greater area (larger $\sigma_1\sigma_2$) and more circular shape ($\min|\sigma_1 - \sigma_2|$) corresponds to better manipulability. For instance, ellipses 1, 2, and 3 in Figure 4.2(b) are better because they have less disparity ($|\sigma_1 - \sigma_2|$) between σ_1 and σ_2 than that of ellipses 4, 5, and 6. Among ellipses 1, 2, and 3, ellipse 3 is better because of larger area ($\sigma_1\sigma_2$). Therefore, ellipse 3 has the best manipulability among the six postures in Figure 4.2(b). At posture 6, the ellipse degenerates to a line, defined by $\sigma_1\mathbf{u_1}$ representing the only direction which the fingertip can move, because $\sigma_2 = 0$.

An illustration of the 3D manipulability measure, *w*, inside the 2D WS in the FE plane ($\theta_1 = 0$) is illustrated in Figure 4.3(a) that displays regions of *w* with a range of values, as shown. Larger values of *w* render better manipulability. As explained above, *w* is independent of the angle of the MCP (θ_1) joint. Thus, a similar illustration can be obtained for any particular WS plane defined by the AA angle θ_1 of the MCP joint. In addition, an example of a 3D manipulability ellipsoid with a specific finger posture is presented in Figure 4.3(b), when the index fingertip reaches a position with the maximum *w*. Comparison of the 3D manipulability ellipsoids follows the same methodology for 2D, presented above, by comparing $\sigma_1\mathbf{u_1}$, $\sigma_2\mathbf{u_2}$, and $\sigma_3\mathbf{u_3}$.

4.3 WS and manipulabilty of the finger with constrained joints

In this section, WS as well as manipulability measures and ellipsoids are analyzed on a finger with a joint constrained to discrete fixed angles. The following examples present analysis of the index finger model by constraining of the PIP and DIP joints individually.

4.3.1 Finger with the PIP joint constrained

The 2D WS of the index finger when its PIP joint is constrained to values from 0° to 80° of flexion is analyzed. Once the PIP joint of the index finger is constrained to a fixed

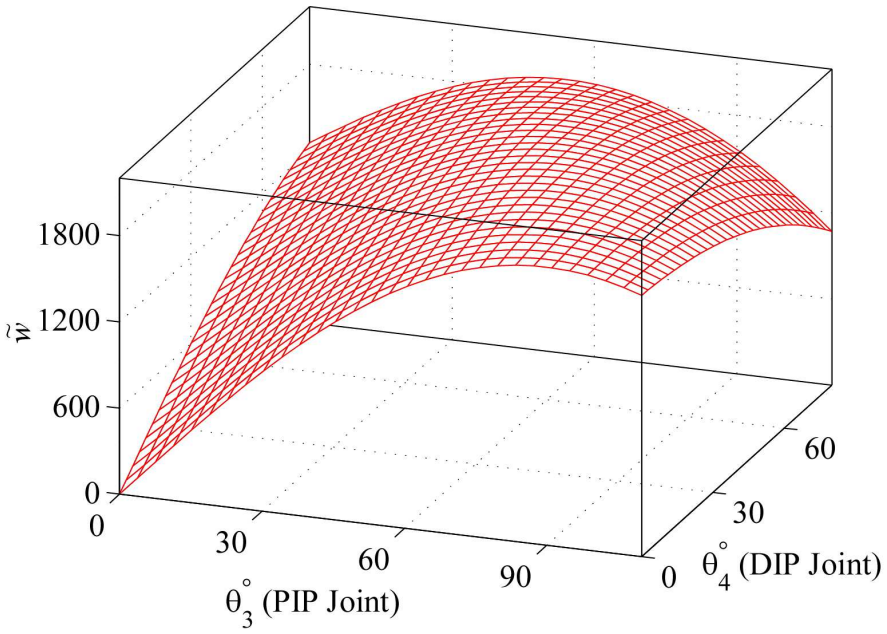

(a) 2D manipulability *measure* $\tilde{w}$ of the index finger

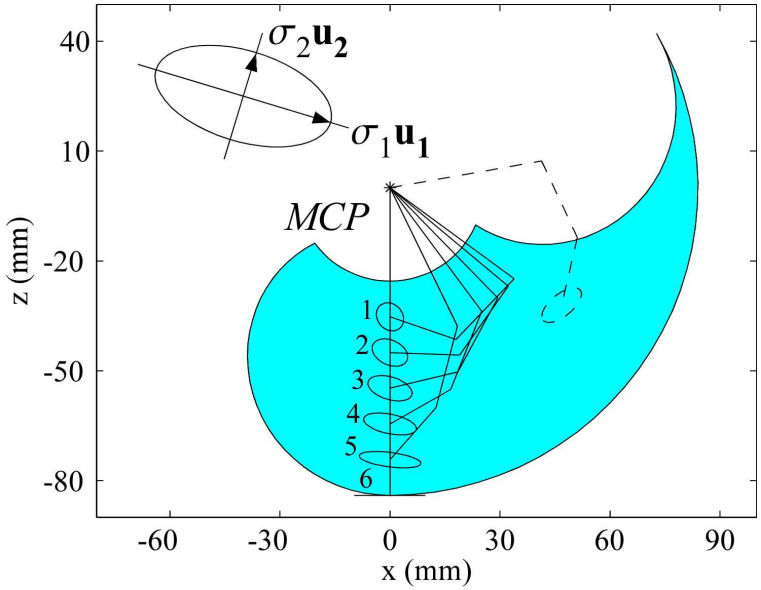

(b) 2D manipulability *ellipses* with finger postures of the index finger

Figure 4.2: (a) The 2D manipulability *measure*, $\tilde{w}$, of the index finger. The maximum value of the 2D manipulability measure, $\tilde{w}$, is around 2×10^3. (b) The 2D manipulability *ellipses* with six different finger postures along a line parallel to the z-axis. A magnified view of posture 3 is illustrated with the two principal directions $\mathbf{u_1} = [0.96 \ -0.29]^T$ and $\mathbf{u_2} = [0.29 \ 0.96]^T$ and the corresponding singular values, $\sigma_1 = 62$ and $\sigma_2 = 31$. The 2D manipulability ellipse of the specific finger posture when the fingertip has maximum $\tilde{w}$ is plotted in dashed-line.

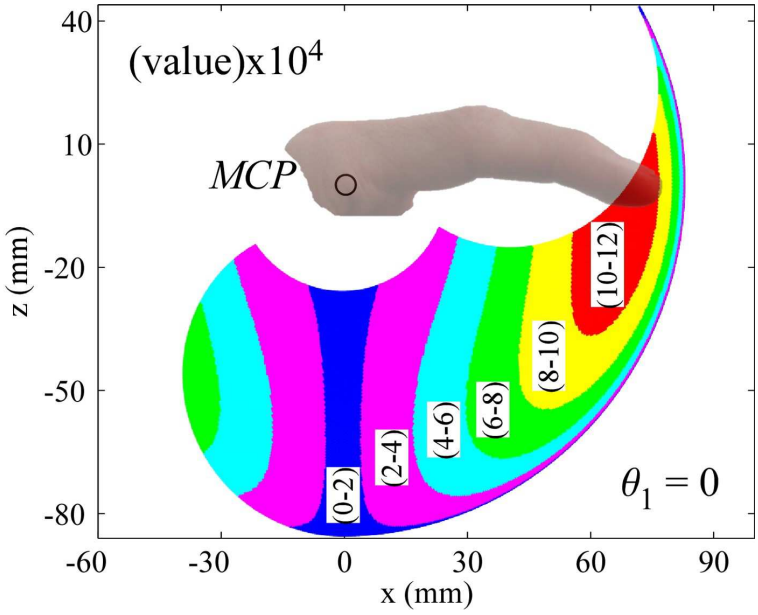

(a) 3D manipulability measure

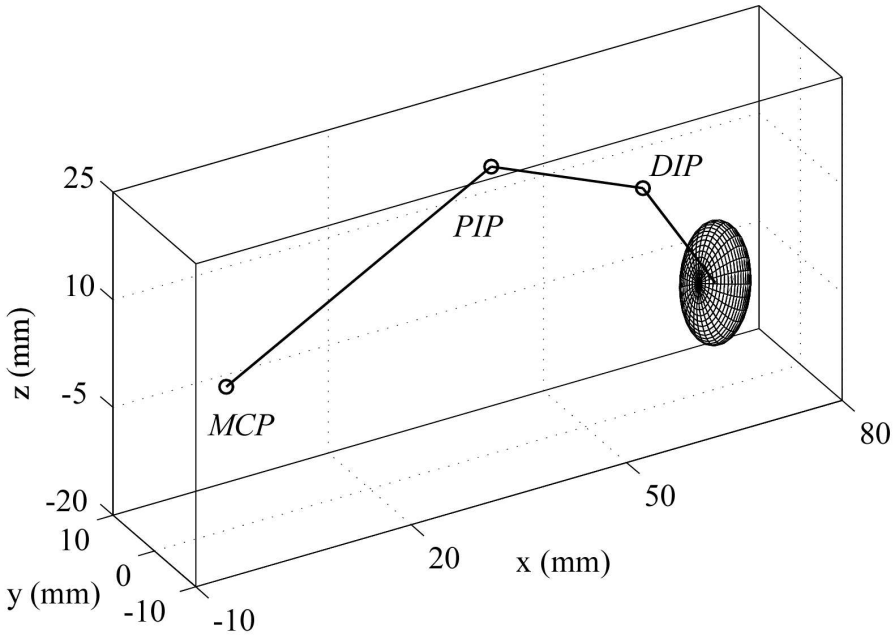

(b) Example of 3D manipulability ellipsoid

Figure 4.3: (a) The 3D manipulability measure, w, of the index finger when $\theta_1 = 0$, as represented on a 2D WS. Several regions corresponding to different ranges of the values of w are illustrated. The maximum value of w, is around 12.7×10^4. (b) The 3D manipulability *ellipsoid* of the specific finger posture when the fingertip has maximum w is plotted. The values of singular values are $\sigma_1 = 77.76$, $\sigma_2 = 68.12$, $\sigma_3 = 24.31$, along with $\mathbf{u_1} = [-0.25\ 0\ -0.97]^T$, $\mathbf{u_2} = [0\ 1\ 0]^T$, and $\mathbf{u_3} = [0.97\ 1\ -0.25]^T$.

angle, it becomes a 3R model, with 3 revolute joints.

Equation (2.1) with model parameters, as well as the ROM of the joints and the value of the PIP joint constraint angle describe the 2D WS boundaries of the constrained finger. Model parameters were obtained from experimental measurements (see Section 2.2.6). Examples of the 2D WS of the finger model when the PIP joint (θ_3) is constrained to 0°, 30° and 60° of flexion are presented in Figure 4.4(a). The parametric expressions of the 2D WS boundaries of the example presented in Section 2.2.1.2 were used with distinct PIP joint constraint angles in order to determine the 2D WS of the finger.

The 3D WS of the PIP constrained finger model is presented in Figure 4.4(b). Similar to the 3D WS of the unconstrained finger, the 3D WS of the constrained case is obtained by revolving the 2D WS of the constrained finger about the AA joint axis of the MCP joint. The ROM of MCP joint about the AA axis was obtained from experimental measurements.

When the PIP joint of index finger is constrained ($\theta_3 = \text{constant}$), the reduced Jacobian $\mathbf{J}'_\theta$, with a DOF (θ_3) removed, is defined as $[dx\ dy\ dz]^T = \mathbf{J}'_\theta[d\theta_1\ d\theta_2\ d\theta_4]^T$. Then, the elements of the $\mathbf{J}'_\theta$ matrix are

$$\begin{aligned}
\mathbf{J}'_\theta(1,1) &= s_1(-l_1c_2 - l_2c_{23} - l_3c_{234}) \\
\mathbf{J}'_\theta(1,2) &= c_1(-l_1s_2 - l_2s_{23} - l_3s_{234}) \\
\mathbf{J}'_\theta(1,3) &= -l_3c_1s_{234} \\
\mathbf{J}'_\theta(2,1) &= c_1(l_1c_2 + l_2c_{23} + l_3c_{234}) \\
\mathbf{J}'_\theta(2,2) &= s_1(-l_1s_2 - l_2s_{23} - l_3s_{234}) \\
\mathbf{J}'_\theta(2,3) &= -l_3s_1s_{234} \\
\mathbf{J}'_\theta(3,1) &= 0 \\
\mathbf{J}'_\theta(3,2) &= -l_1c_2 - l_2c_{23} - l_3c_{234} \\
\mathbf{J}'_\theta(3,3) &= -l_3c_{234}
\end{aligned} \tag{4.12}$$

The $\mathbf{J}'_\theta$ matrix is a reduced 3×3 matrix, and the SVD analysis becomes a conventional eigenvalue problem. The interpretation of the results is similar to Section 4.2.2.

The manipulability measure of the constrained index finger is found by substituting

equation (4.12) into equation (4.11), resulting in

$$w_c = |l_3(l_1c_2 + l_2c_{23} + l_3c_{234})(l_2s_4 + l_1s_{34})| \tag{4.13}$$

The constrained 3R model is used to calculate the manipulability measure and ellipsoid of the index finger. Manipulability measures and ellipsoids are calculated using the Jacobian matrix of the 3R model, $\mathbf{J}'^{2}_{\theta}$, derived in equation (4.12). Since manipulability measures and ellipsoids are configuration-dependent, the maximum values of the manipulability measures and their corresponding ellipsoids are considered for analysis. Figure 4.5 presents the calculation of the manipulability ellipsoids for distinct PIP joint constraint angles. Equation (4.13) shows that the manipulability measure of the constrained finger does not depend on the angle of MCP (θ_1) joint. Figure 4.5 presents the manipulability measure (w_c) obtained when the index finger PIP joint is constrained to angles at 0°, 30°, and 60°. Due to the singularity along the z-axis, as in Figure 4.1(b), the manipulability measure, w_c, of the constrained finger is zero along this axis because one singular value is equal to zero. However, this does not mean that the index finger cannot manipulate an object along the z-axis. It simply means that the manipulability is lost along the direction associated with the null singular value.

4.3.2 Finger with the DIP joint constrained

The 2D WS of the index finger model with the DIP joint constrained to values from 0° to 80° of flexion is analyzed. Once the DIP joint of the index finger is constrained to a fixed angle, it becomes a 3R model, with 3 revolute joints.

Equation (2.1) with model parameters, as well as the ROM of the joints and the value of the DIP joint constraint angle describe the 2D WS boundaries of the constrained finger. Model parameters were obtained from experimental measurements (see Section 2.2.6). Examples of the 2D WS of the finger model when the DIP joint (θ_4) is constrained to 0°, 30°

[2] Although one DOF of the index finger has been removed (θ_3 = constant), the Jacobian matrix of the 3R model, $\mathbf{J}'_{\theta}$, is of rank three. Thus, three singular values and three principal axes can be obtained by solving the conventional eigenvalue problem.

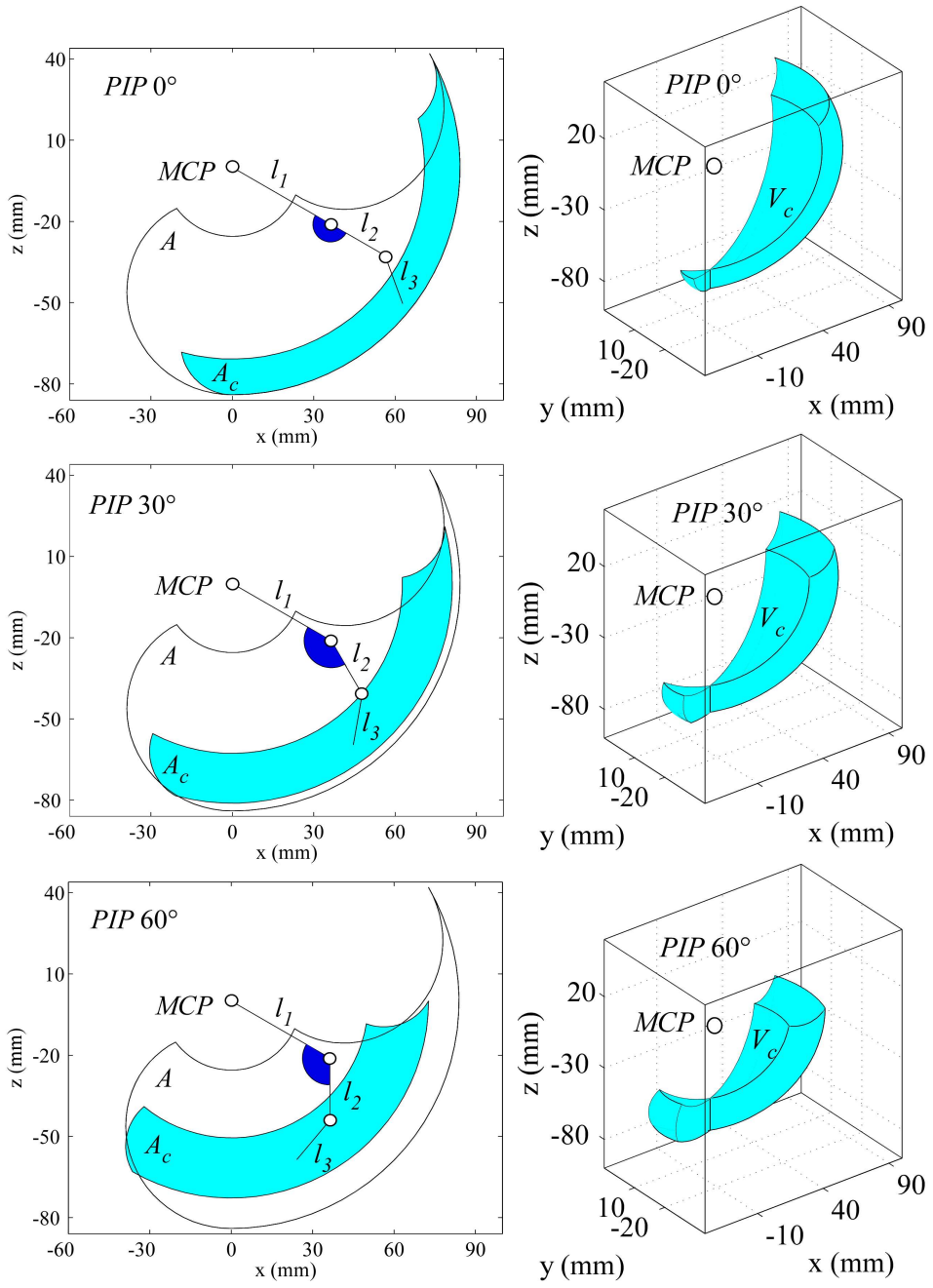

(a) 2D WS (b) 3D WS

Figure 4.4: (a) The 2D WS when the PIP joint is constrained at 0°, 30°, and 60°, respectively. The colored area shows the reduced WS with the corresponding angular constraint, as compared with the 2D WS without constraint. The areas of the reduced WS are 2,136 mm^2, 2,773 mm^2, and 2,870 mm^2, respectively. (b) The 3D WS is shown with PIP joint angles at 0°, 30°, and 60°. The volumes of the reduced work-volumes are 74,751 mm^3, 80,216 mm^3, and 64,584 mm^3, respectively.

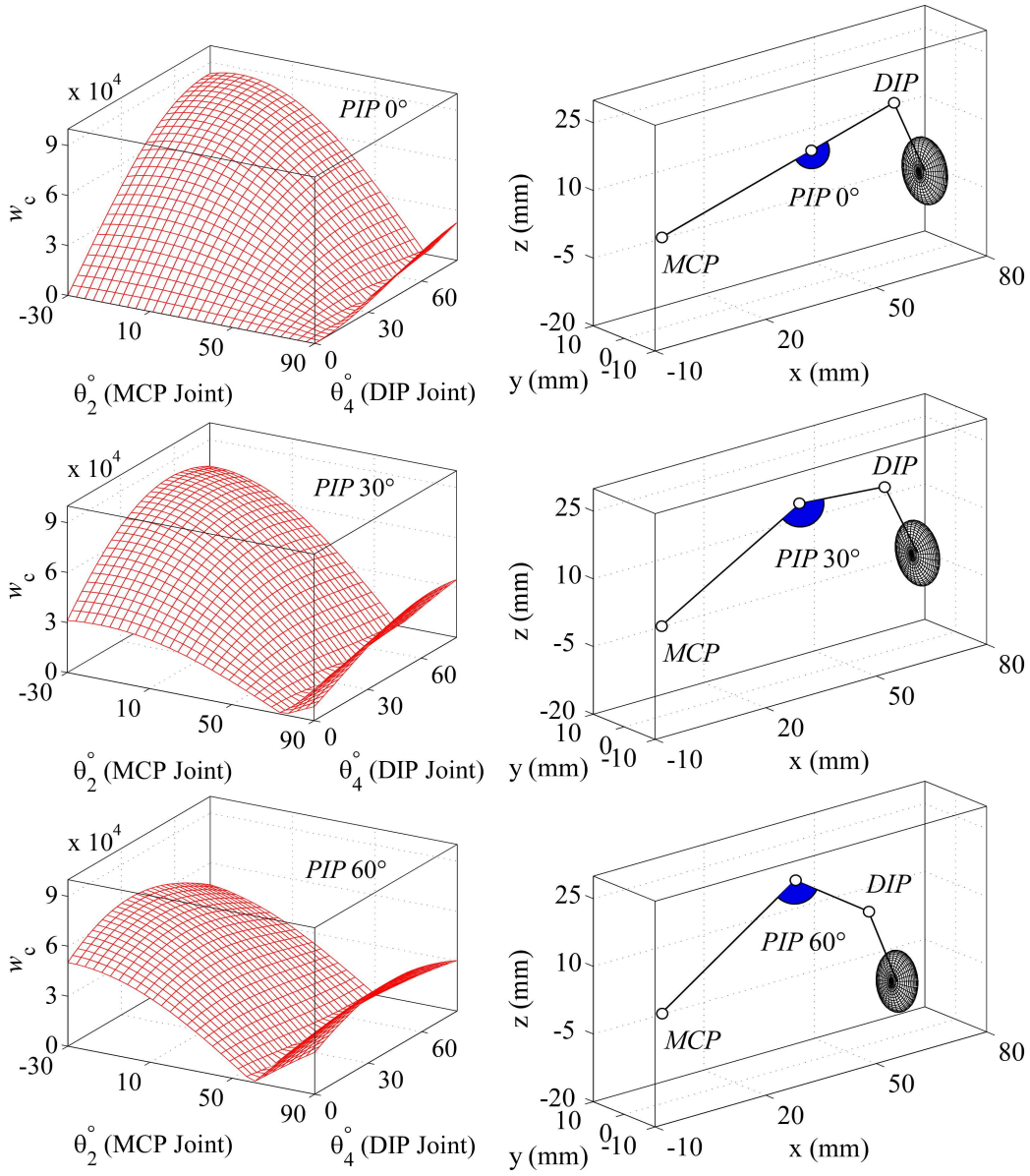

(a) 3D manipulability measure (b) 3D manipulability ellipsoid

Figure 4.5: (a) The 3D manipulability measure when the PIP joint is constrained at 0°, 30°, and 60°. The maximum values of the 3D manipulability measure are $8,63 \times 10^4$, $8,13 \times 10^4$, and $6,73 \times 10^4$, respectively. (b) The 3D manipulability ellipsoids of the specific finger postures corresponding to the maximum values of the 3D manipulability measures are plotted when the PIP joint is constrained at 0°, 30°, and 60°, respectively.

and 60° of flexion are presented in Figure 4.6(a). The parametric expressions of the 2D WS boundaries in equations (4.14) to (4.17) were used to determine the 2D WS of the finger under selected DIP joint constrain angles.

$$C_1 : \begin{cases} x_{tip} = & l_1\cos(90^\circ) \\ & +l_2\cos(90^\circ+\theta_3) \\ & +l_3\cos(90^\circ+\theta_3+\text{DIP}), \\ y_{tip} = & 0, \\ z_{tip} = & -l_1\sin(90^\circ) \\ & -l_2\sin(90^\circ+\theta_3) \\ & -l_3\sin(90^\circ+\theta_3+\text{DIP}), \end{cases} \quad \text{with} \quad 0^\circ \leq \theta_3 \leq 110^\circ \tag{4.14}$$

$$C_2 : \begin{cases} x_{tip} = & l_1\cos(\theta_2) \\ & +l_2\cos(\theta_2+0^\circ) \\ & +l_3\cos(\theta_2+0^\circ+\text{DIP}), \\ y_{tip} = & 0, \\ z_{tip} = & -l_1\sin(\theta_2) \\ & -l_2\sin(\theta_2+0^\circ) \\ & -l_3\sin(\theta_2+0^\circ+\text{DIP}), \end{cases} \quad \text{with} \quad -30^\circ \leq \theta_2 \leq 90^\circ \tag{4.15}$$

$$
C_3 : \begin{cases} x_{tip} = & l_1 \cos(-30^\circ) \\ & +l_2 \cos(-30^\circ + \theta_3) \\ & +l_3 \cos(-30^\circ + \theta_3 + \text{DIP}), \\ y_{tip} = & 0, \\ z_{tip} = & -l_1 \sin(-30^\circ) \\ & -l_2 \sin(-30^\circ + \theta_3) \\ & -l_3 \sin(-30^\circ + \theta_3 + \text{DIP}), \end{cases} \quad \text{with} \quad 0^\circ \leq \theta_3 \leq 110^\circ \tag{4.16}
$$

$$
C_4 : \begin{cases} x_{tip} = & l_1 \cos(\theta_2) \\ & +l_2 \cos(\theta_2 + 110^\circ) \\ & +l_3 \cos(\theta_2 + 110^\circ + \text{DIP}), \\ y_{tip} = & 0, \\ z_{tip} = & -l_1 \sin(\theta_2) \\ & -l_2 \sin(\theta_2 + 110^\circ) \\ & -l_3 \sin(\theta_2 + 110^\circ + \text{DIP}), \end{cases} \quad \text{with} \quad -30^\circ \leq \theta_2 \leq 90^\circ \tag{4.17}
$$

The 3D WS of the DIP constrained finger model is presented in Figure 4.6(b). Similar to the 3D WS of the PIP constrained finger, the 3D WS of the DIP constrained case is obtained by revolving the 2D WS about the AA joint axis of the MCP joint. The ROM of MCP joint about the AA axis was obtained from experimental measurements.

When the DIP joint of index finger is constrained ($\theta_4 =$ constant), the reduced Jacobian $\mathbf{J}'_\theta$, with a DOF (θ_4) removed, is defined as $[dx\ dy\ dz]^T = \mathbf{J}'_\theta [d\theta_1\ d\theta_2\ d\theta_3]^T$. Then,

the elements of the $\mathbf{J}'_\theta$ matrix are given by

$$\begin{aligned}
\mathbf{J}'_\theta(1,1) &= s_1(-l_1c_2 - l_2c_{23} - l_3c_{234}) \\
\mathbf{J}'_\theta(1,2) &= c_1(-l_1s_2 - l_2s_{23} - l_3s_{234}) \\
\mathbf{J}'_\theta(1,3) &= c_1(-l_2s_{23} - l_3s_{234}) \\
\mathbf{J}'_\theta(2,1) &= c_1(l_1c_2 + l_2c_{23} + l_3c_{234}) \\
\mathbf{J}'_\theta(2,2) &= s_1(-l_1s_2 - l_2s_{23} - l_3s_{234}) \\
\mathbf{J}'_\theta(2,3) &= s_1(-l_2s_{23} - l_3s_{234}) \\
\mathbf{J}'_\theta(3,1) &= 0 \\
\mathbf{J}'_\theta(3,2) &= -l_1c_2 - l_2c_{23} - l_3c_{234} \\
\mathbf{J}'_\theta(3,3) &= -l_2c_{23} - l_3c_{234}
\end{aligned} \tag{4.18}$$

The $\mathbf{J}'_\theta$ matrix is a reduced 3×3 matrix, and the SVD analysis becomes a conventional eigenvalue problem. The interpretation of the results is similar to Section 4.2.2.

The manipulability measure of the constrained index finger is found by substituting equation (4.18) into equation (4.11) as follows

$$w_c = |l_1(l_1c_2 + l_2c_{23} + l_3c_{234})(l_2s_3 + l_3s_{34})| \tag{4.19}$$

The constrained 3R, model is used to calculate the manipulability measure and ellipsoid of the index finger. Manipulability measures and ellipsoids are calculated using the Jacobian matrix of the 3R model, $\mathbf{J}'^{3}_\theta$, derived in equation (4.18). Since manipulability measures and ellipsoids are configuration-dependent, the maximum values of the manipulability measures and their corresponding ellipsoids are considered for analysis. Figure 4.7 presents the calculation of the manipulability ellipsoids for distinct DIP joint constraint angles. Equation (4.19) shows that the manipulability measure of the constrained finger does not depend on the angle of MCP (θ_1) joint. Figure 4.7 presents the manipulability measure (w_c) obtained when the index finger DIP joint is constrained to angles at 0°, 30°, and

[3] Although one DOF of the index finger has been removed ($\theta_4 =$ constant), the Jacobian matrix of the 3R model, $\mathbf{J}'_\theta$, is of rank three. Thus, three singular values and three principal axes can be obtained by solving the conventional eigenvalue problem.

Table 4.1: Theoretical data obtained with the unconstrained and constrained finger model. The model parameters are as follows: $l_1 = 42$ mm, $l_2 = 23$ mm, and $l_3 = 19$ mm. The ROM for θ_1, θ_2, θ_3 and θ_4 are: $-30^\circ \leq \theta_1 \leq 10^\circ$, $-30 \leq \theta_2 \leq 90^\circ$, $0^\circ \leq \theta_3 \leq 110^\circ$ and $0^\circ \leq \theta_4 \leq 80^\circ$. The coupling relation between the DIP and PIP joint of the unconstrained (UC) finger is $\theta_4 \leq (2/3)\theta_3$. A/A_c: 2D WS area; V/V_c: 3D WS volume

Model	A/A_c mm^2	V/V_c mm^3	Model	A/A_c mm^2	V/V_c mm^3
UC	6,710	151,830	UC	6,710	151,830
PIP 0°	2,136	74,751	DIP 0°	4,958	127,478
PIP 20°	2,615	81,175	DIP 20°	5,360	130,857
PIP 30°	2,773	80,216	DIP 30°	5,443	128,535
PIP 40°	2,870	76,843	DIP 40°	5,443	123,702
PIP 50°	2,902	71,483	DIP 50°	5,360	117,702
PIP 60°	2,870	64,584	DIP 60°	5,197	108,509
PIP 80°	2,615	48,053	DIP 80°	4,652	88,627

60°. Again, due to the singularity along the z-axis, as in Figure 4.1(b), the manipulability measure, w_c, of the constrained finger is zero along this axis because one singular value is equal to zero.

4.4 Results of theoretical modeling

Results of the 2D and 3D WS areas and volumes of the unconstrained and constrained index finger model are summarized in Table 4.1. Similarly, the result of manipulability measures and ellipsoids of the unconstrained and constrained index finger model are summarized in Table 4.2.

4.4.1 Design indices

Similar to Section 2.2.2, the consideration of kinematic aspects of the finger was utilized to select the optimal joint constraint angles. In order to assess some of those aspects, quantitative measures of WS and manipulability were analyzed. In particular, measures of the 2D and 3D WS, as well as manipulability measures and ellipsoids of the index finger

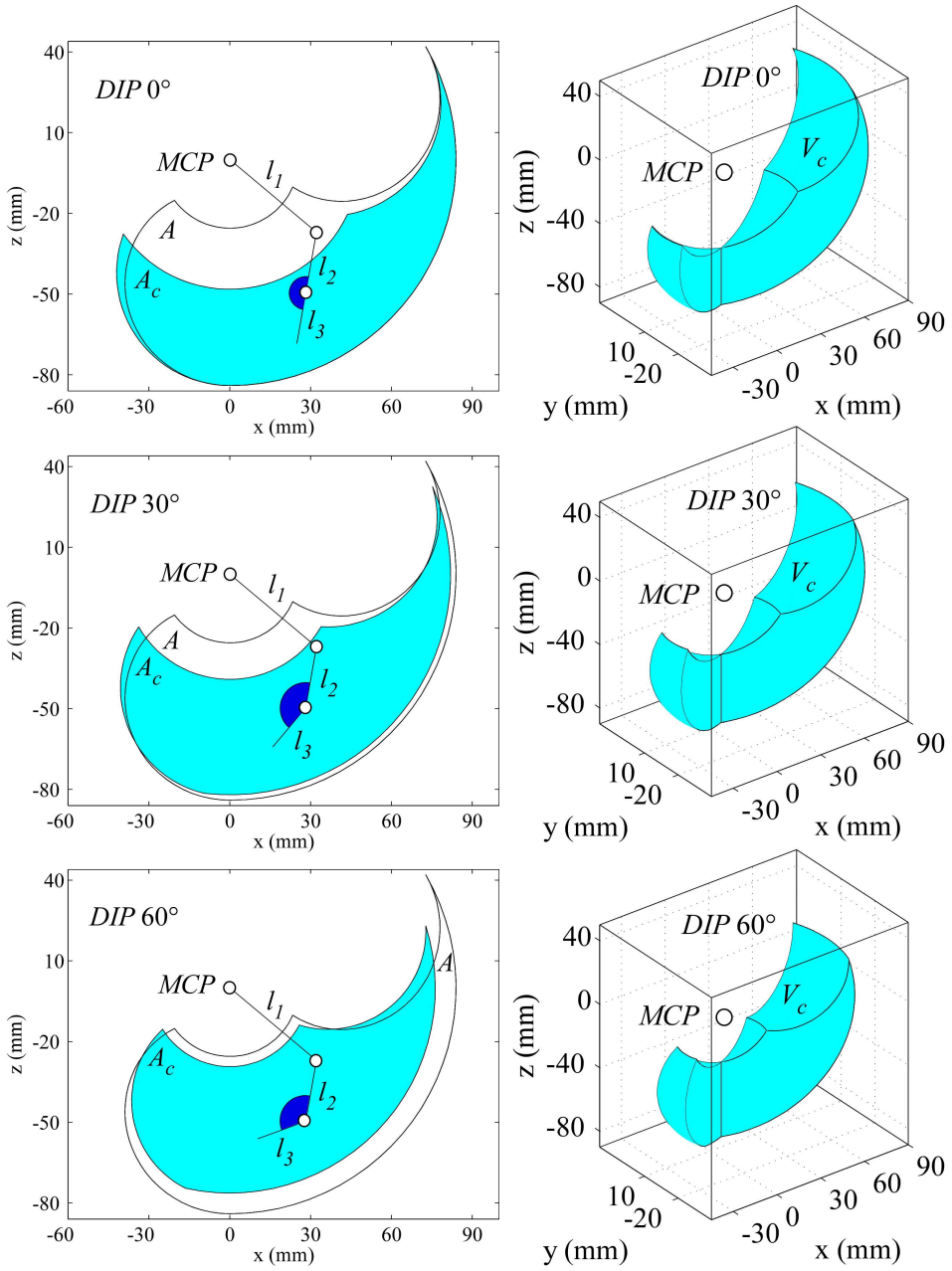

(a) 2D WS (b) 3D WS

Figure 4.6: (a) The 2D WS when the DIP joint is constrained at 0°, 30°, and 60°, respectively. The colored area shows the reduced WS with the corresponding angular constraint, as compared with the 2D WS without constraint. The areas of the reduced WS are 4,958 mm^2, 5,443 mm^2, and 5,197 mm^2, respectively. (b) The 3D WS is shown with DIP joint angles at 0°, 30°, and 60°. The volumes of the reduced work-volumes are 136,793 mm^3, 128,775 mm^3, and 108,509 mm^3, respectively.

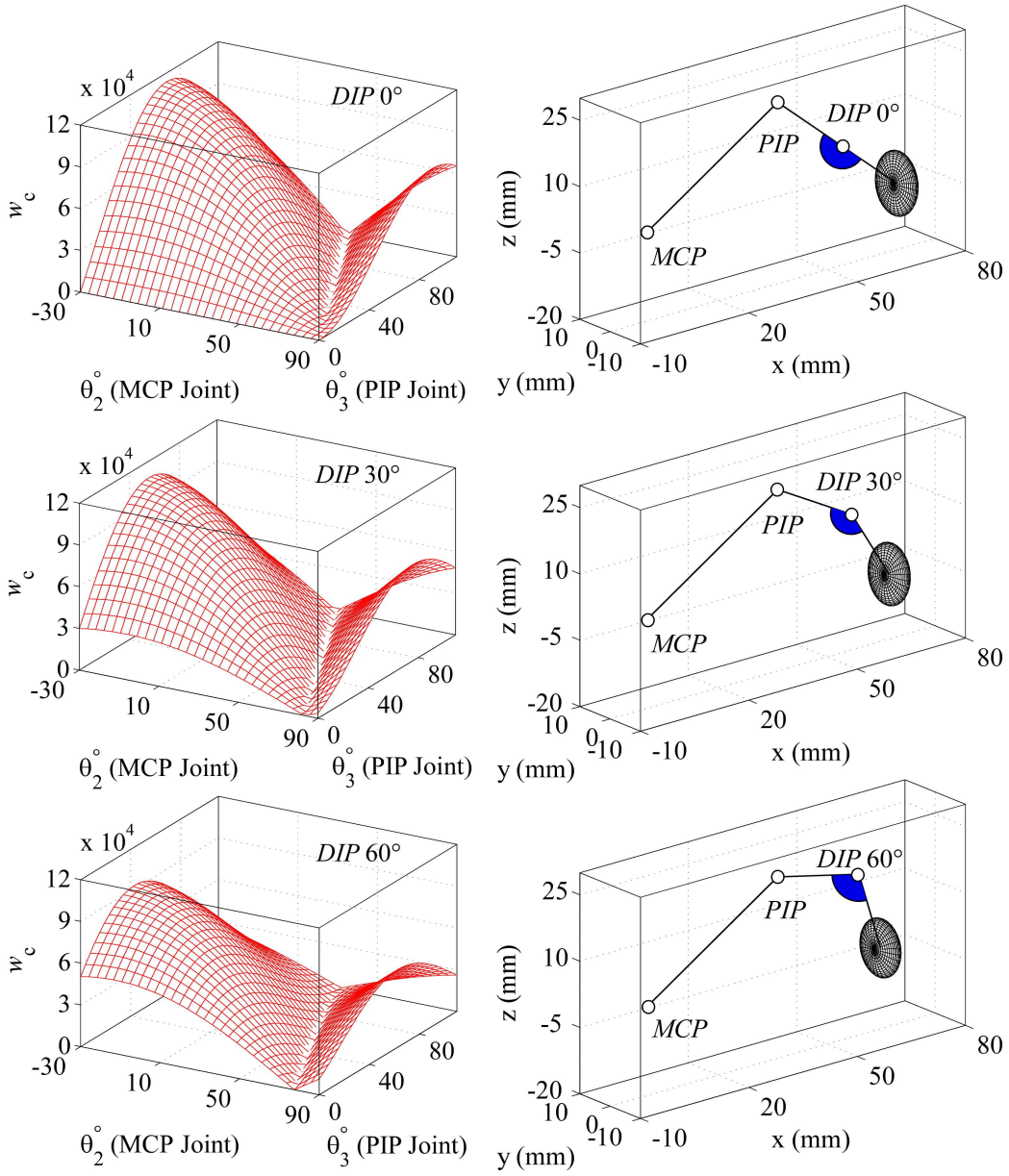

(a) 3D manipulability measure (b) 3D manipulability ellipsoid

Figure 4.7: (a) The 3D manipulability measure when the DIP joint is constrained at 0°, 30°, and 60°. The maximum values of the 3D manipulability measure are 11.3×10^4, 10.8×10^4, and 9.24×10^4, respectively. (b) The 3D manipulability ellipsoids of the specific finger postures corresponding to the maximum values of the 3D manipulability measures are plotted when the DIP joint is constrained at 0°, 30°, and 60°, respectively.

Table 4.2: Theoretical data obtained with the unconstrained and constrained finger model. The model parameters are as follows: $l_1 = 42$ mm, $l_2 = 23$ mm, and $l_3 = 19$ mm. The ROM for θ_1, θ_2, θ_3 and θ_4 are: $-30 \leq \theta_1 \leq 10^\circ$, $-30^\circ \leq \theta_2 \leq 90^\circ$, $0^\circ \leq \theta_3 \leq 110^\circ$ and $0^\circ \leq \theta_4 \leq 80^\circ$. The coupling relation between the DIP and PIP joint of the unconstrained (UC) finger is $\theta_4 \leq (2/3)\theta_3$. The principal direction, $\mathbf{u_1} = [0\ 1\ 0]^T$, remains constant. $w_{\max}/w_{c\max}$: maximum value of manipulability measure ; σ: singular value; $\mathbf{u}$: principal direction.

Model	$w_{\max}/w_{c\max}$	σ_1	σ_2	σ_3	$\mathbf{u_1}$	$\mathbf{u_3}$
UC	$1.27\text{x}10^5$	77.76	68.12	24.31	$[-0.25\ 0\ -0.97]^T$	$[0.97\ 0\ -0.25]^T$
PIP 0°	$8.63\text{x}10^4$	72.21	71.61	16.68	$[0.06\ 0\ 0.99]^T$	$[-0.99\ 0\ 0.06]^T$
PIP 20°	$8.41\text{x}10^4$	71.63	71.01	16.53	$[0.04\ 0\ 0.99]^T$	$[-0.99\ 0\ 0.04]^T$
PIP 30°	$8.13\text{x}10^4$	70.24	69.63	16.63	$[0.03\ 0\ 0.99]^T$	$[-0.99\ 0\ 0.03]^T$
PIP 40°	$7.76\text{x}10^4$	69.31	68.62	16.32	$[-0.03\ 0\ -0.99]^T$	$[0.99\ 0\ -0.03]^T$
PIP 50°	$7.29\text{x}10^4$	67.08	66.27	16.40	$[0.1\ 0\ 0.99]^T$	$[-0.99\ 0\ 0.1]^T$
PIP 60°	$6.73\text{x}10^4$	65.33	64.06	16.07	$[0.16\ 0\ 0.99]^T$	$[-0.99\ 0\ 0.16]^T$
PIP 80°	$5.39\text{x}10^4$	60.67	57.87	15.36	$[0.29\ 0\ 0.96]^T$	$[-0.96\ 0\ 0.29]^T$
DIP 0°	$1.13\text{x}10^5$	78.5	69.34	20.88	$[0.23\ 0\ 0.98]^T$	$[-0.98\ 0\ 0.23]^T$
DIP 20°	$1.11\text{x}10^5$	77.1	68.19	21.14	$[0.23\ 0\ 0.97]^T$	$[-0.97\ 0\ 0.23]^T$
DIP 30°	$1.08\text{x}10^5$	75.83	67.26	21.18	$[0.23\ 0\ 0.97]^T$	$[-0.97\ 0\ 0.23]^T$
DIP 40°	$1.04\text{x}10^5$	74.22	66.12	21.14	$[0.22\ 0\ 0.97]^T$	$[-0.97\ 0\ 0.22]^T$
DIP 50°	$9.85\text{x}10^4$	73.92	66.41	20.12	$[0.17\ 0\ 0.98]^T$	$[-0.98\ 0\ 0.17]^T$
DIP 60°	$9.24\text{x}10^4$	71.7	64.85	19.86	$[0.16\ 0\ 0.99]^T$	$[-0.99\ 0\ 0.16]^T$
DIP 80°	$7.78\text{x}10^4$	66.56	61.25	19.09	$[-0.12\ 0\ 0.99]^T$	$[0.99\ 0\ -0.12]^T$

model were investigated under imposed PIP and DIP joint constraint angles.

Equation (4.20) defines an index pertaining to the 2D WS area

$$I_A = \frac{A_c}{A} \tag{4.20}$$

where I_A is the index of the 2D WS, $A_c(\theta_3)$ is the WS area when the finger joint is constrained to a prescribed angle, and A is the WS area when the finger joint is unconstrained (Table 4.1).

Equation (4.21) defines an index pertaining to the 3D WS volume

$$I_V = \frac{V_c}{V} \tag{4.21}$$

where I_V is the index of the 3D WS volume, V_c is the WS volume when the finger joint is constrained to a prescribed angle, and V is the WS volume when the finger joint is unconstrained (Table 4.1).

Equation (4.22) defines an index pertaining to the manipulabity measure

$$I_w = \frac{w_{c\max}}{w_{\max}} \tag{4.22}$$

where I_w is the index of manipulability measure, $w_{c\max}$ is the maximum value of the manipulability measure when the finger joint is constrained to a prescribed angle, and $w_{\max}$ is the maximum value of the manipulability measure when the finger joint is not constrained (Table 4.2). In addition, equation (4.23) defines an index pertaining to the aspect ratio of the manipulability ellipse or ellipsoid at the fingertip as

$$I_e = \frac{\sigma_3}{\sigma_1} \tag{4.23}$$

where I_e is the aspect ratio of the manipulability ellipsoid at the fingertip with constraint, and σ_3 and σ_1 are the singular values corresponding to the minimum and maximum radii of the manipulability ellipsoid at the fingertip [54] (Table 4.1).

The design indices defined above describe different aspects in the consideration of movement and performance of the finger after joint constraints are imposed. Since each

index considers different aspects of the constrained finger and has different ranges of numerical values, the selection of the constraint angle is an optimization which takes into account the trade-offs between conflicting objectives. Although a single solution does not exist to simultaneously optimize each objective, we used a weighted-sum criterion to estimate the constraint angle that best satisfies such condition among the four indices (I_A, I_V, I_w, and I_e) as follows

$$\max_{\theta} \; f(\theta) \tag{4.24}$$

where f is the objective function to be optimized, defined as

$$f(\theta) = \sum_{i=1}^{n} \alpha_i \frac{I_i(\theta) - \min\{I_i\}}{\max\{I_i\} - \min\{I_i\}} \tag{4.25}$$

where α_i are the weighting factors to adjust for emphasis among considered indices with $\sum \alpha_i = 100\%$, $I_i(\theta_3)$ are index values pertaining to a particular aspect (i) and for a prescribed constraint angle (θ), and $i = A, V, w, e$ are the number of design indices considered. Note that the values of the parameters in equation (4.25) depend on the constraint angle, θ. The objective criterion can be adjusted depending on the finger utilization and preferences of each individual; thus, inclusion of the weighting factors allows to customize this perspective and quantify an optimal joint constraint angle among the aspects provided in the design indices.

The design indices for discrete PIP and DIP joint constraint angles are calculated and presented in Figure 4.8(a) and 4.8(b), respectively.

To illustrate the usage of the weighted-sum criterion in equation (4.25), we considered three scenarios. First, if all indices were weighted equally and treated with equal importance, the weighting factors would be $\alpha_A = \alpha_V = \alpha_w = \alpha_e = 0.25$. Using the results from Figure 4.8(a) and 4.8(b) with different constraint angle θ, the maximum of funtion f in equation (4.25) was obtained, and plotted in Figure 4.9(a) and 4.9(b). The second scenario emphasizes the 2D WS area, with a choice of $\alpha_A = 0.4$, $\alpha_V = 0.2$, $\alpha_w = 0.2$ and $\alpha_e = 0.2$ for the weighted-sum. The optimized function f was obtained and plotted in Figure 4.9(a) and 4.9(b). In the third scenario, the emphasis was in the consideration of the

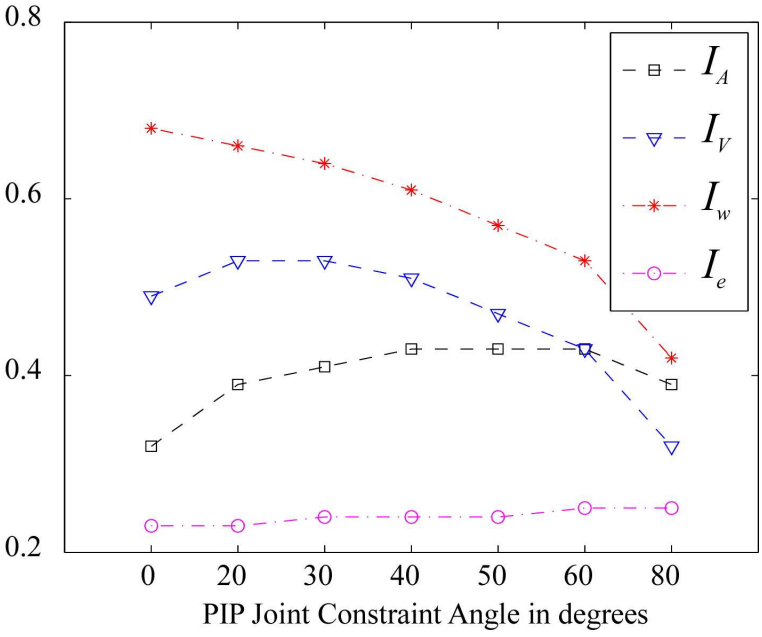

(a) PIP joint constrained

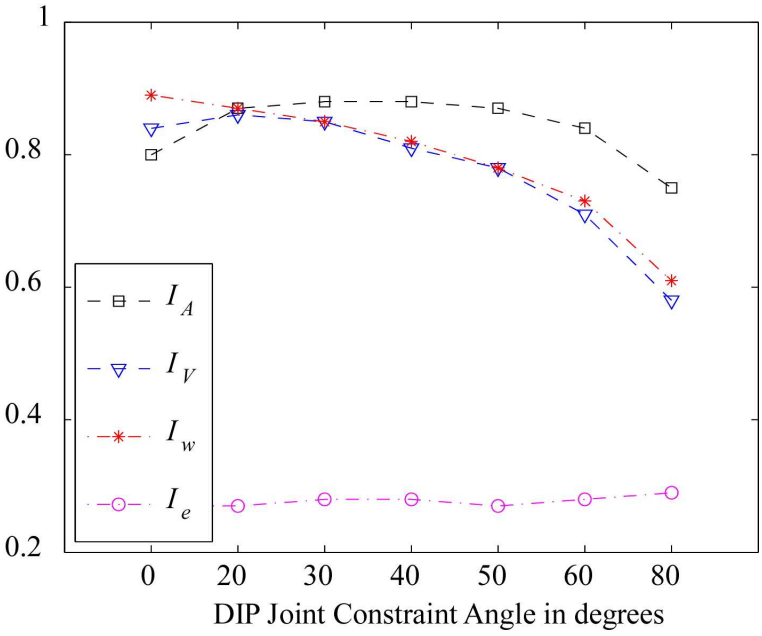

(b) DIP joint constrained

Figure 4.8: Four different design indices pertaining to the WS area (I_A), volume (I_V), the manipulability measure (I_w), and the aspect ration of the manipulabilty ellipsoid (I_e), as a function of varying: (a) PIP constraint angle (θ_3), and (b) DIP constraint angle (θ_4).

shape of the manipulabilty ellipsoid, with a penalty on large aspect ratio, in order to make the ellipsoid more homogeneous. With a choice of $\alpha_A = 0.2$, $\alpha_V = 0.2$, $\alpha_w = 0.2$, and $\alpha_e = 0.4$ to meet the criterion, f was obtained and plotted in Figure 4.9(a) and 4.9(b). In the first scenario when all indices are weighted equally and treated with equal importance, the values of f in Fig. 4.9 (a) and (b) reached their maximum values with the PIP and DIP joint constraint angles at 40° and 30°, respectively. In the second scenario, the model values of f are maximum when the PIP and DIP joints were constrained between 30° and 50° and between 30° and 40°, respectively. With an emphasis of the aspect ratio of the manipulabilty ellipsoid, I_e, in the third scenario, the model values of f reached their maximum values when the PIP and DIP joints were constrained at 50° and 30°, respectively.

4.4.2 Discussions

A novel methodology to determine the optimum joint constraint angles that allow for maximum finger function is proposed. Development and application of the proposed methodology is conducted on the index finger, although the systematic methodology can be easily applied to other fingers and limbs by changing the kinematic parameters. The WS of the index finger when its PIP and DIP joints are both unconstrained and constrained are investigated.

4.4.2.1 Design indices

Design indices for the 2D and 3D WS of the index finger, I_A and I_V, with constrained PIP and DIP joints are plotted in Figure 4.8, showing that the index fingertip has the greatest WS areas and volumes when the PIP joint is constrained to about 60° and 20°, respectively. Similarly, the index fingertip has the greatest WS areas and volumes when the DIP joint is constrained to about 30° and 20°, respectively.

Manipulability ellipsoids of the constrained finger are smaller than those of the unconstrained ones since one DOF has been removed. Indices pertaining to the manipulability

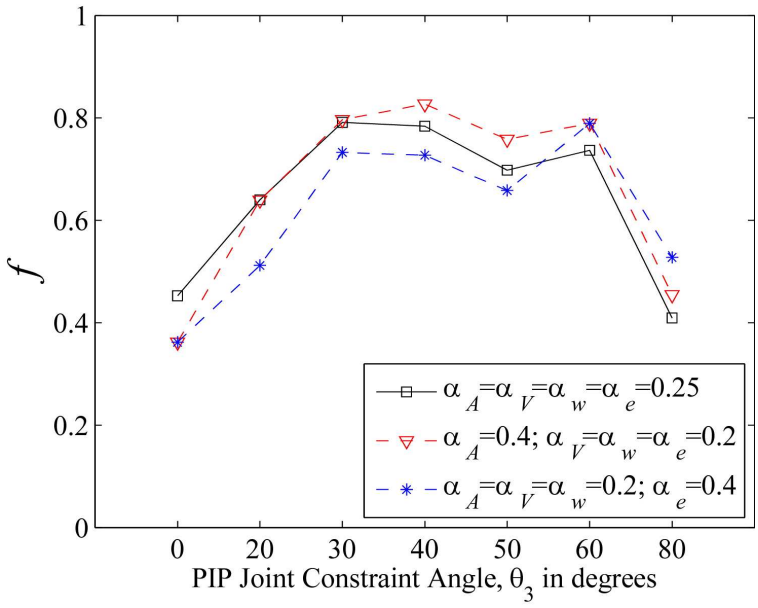

(a) PIP joint constrained

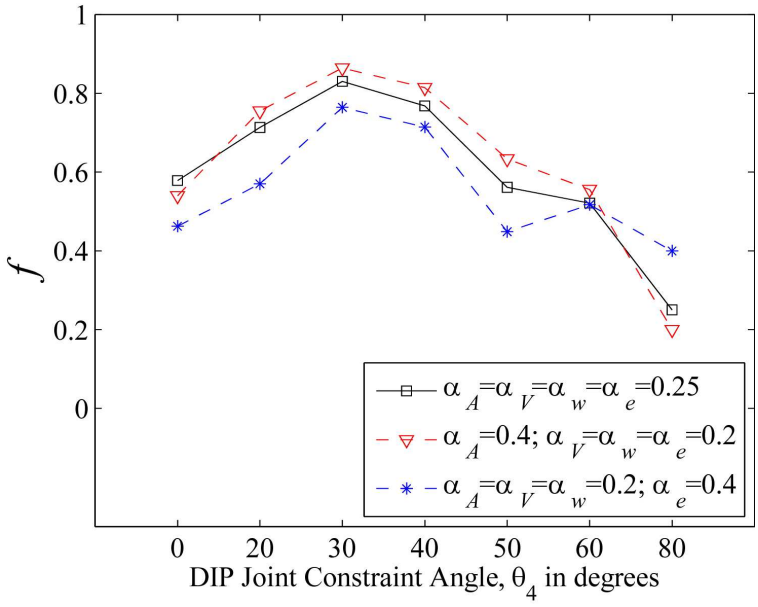

(b) DIP joint constrained

Figure 4.9: The weighted-sum criterion, f in equation 4.25, for different sets of α_i, as a function of: (a) PIP joint constraint angle (θ_3), and (b) DIP joint constraint angle (θ_4).

measure and aspect ratio of the manipulability ellipsoid are shown in Figure 4.8, showing that the manipulability measure is maximum when the PIP and DIP joints are constrained to 0°, and decreases to its minimum value whenthe PIP and DIP joints are constrained to 80°. On the other hand, the aspect ratio of the manipulability ellipsoid presents its maximum value when the PIP and DIP joints are constrained to an angle of 80° of flexion. Since the aspect ratio of the manipulability ellipsoid provides information of the directional uniformity of the ellipsoid and is independent of the size, the index finger with its PIP and DIP joints constrained to 80° presents the most uniform ellipsoid at the fingertip. The distribution of the values of the indices pertaining the aspect ratio of the manipulability ellipsoid are configuration-dependent, and those used in this analysis are obtained at different configurations determined by the maximum value of the manipulability measure.

4.4.2.2 Optimal criterion using the weighted-sum

Information of the design indices is combined to determine the optimum index finger PIP and DIP joint constraint angles. The function, f, of both the PIP and DIP, defined in equation (4.25), are plotted in Figure 4.9 with selected sets of weighting factors. Various scenarios are presented with different sets of weighting factors for trade-off among the indices to illustrate the application of the weighted-sum criterion. As mentioned in Section 2.4.5, weighted factors could be selected to represent aspects such as cosmetic appearance and specific functionality.

It is clear from the foregoing observations that the trade-off between different indices by varying the weighting factors has significant implication on the results of f, and hence the constraint angle for medical and rehabilitation procedures.

Figures 4.9(a) and (b) show that f reaches its maximum value when the PIP and DIP joints are constrained to 40° and 30° of flexion, when all indices are weighted equally and treated with equal importance ($\alpha_A = \alpha_V = \alpha_w = \alpha_e = 0.25$). In the second scenario with the emphasis on the 2D WS area only, the f is maximum when the PIP and DIP joints are

constrained at 40° and 30° of flexion, respectively. Although the f values of the PIP joint are nearly the same from $30^\circ \leq \theta_3 \leq 60^\circ$ in the three scenarios, the f values of the DIP joint were quite similar for $30^\circ \leq \theta_4 \leq 40^\circ$.

In the preceding discussions, f is defined and calculated based on different scenarios and physical situations under which distinct criteria are considered, through weighting factors, in order to obtain optimal factors to optimize the WS and manipulability of finger once the constraint angle is imposed on the patient. Constraint angles can be adapted by varying these factors. Hand surgeons, physicians, and therapists can select different weighting factors on the design indices, based on the chosen criteria and individual circumstances, in order to customize for each patient to enhance the quality of life after surgery or during rehabilitation.

4.5 Summary

A new methodology to find the optimum joint constraint angles that allow for better finger WS and manipulability has been presented. The index finger has been used to develop and illustrate this methodology. Kinematic analysis of the unconstrained and constrained index finger model has been conducted to find the optimum PIP and DIP joint constraint angles. Results presented show that even though the index finger functionality is going to be reduced due to the joint constraint, it is possible to optimize the finger WS and manipulability for a unique PIP and DIP joint constraint angles. In general, this new methodology can be applied systematically to other fingers and limbs so that constraint angles with optimal capability of movement and manipulability can be found. Therefore, this study will help surgeons, physicians, and therapists make more informed decisions before constraint angles are imposed, and customize those angles for each patient to enhance the quality of life after surgery or during rehabilitation.

Chapter 5

Biomechanics and Pinch Force of Finger Under Simulated Arhtrodesis

5.1 Introduction

Osteoarthritis is the most common cause of locomotor dysfunction and disabling joint pain in the United States. It is also the most common rheumatic disease [41]. The disease affects 33% of individuals over the age of 65 years. The rapid increase in the precentage of people older than 55 years of age in Western countries means that osteoarthritis is becoming a major public heath problem, affecting approximately 40 million people [41]. Hand and finger osteoarthritis typical presentation includes joint pain, limited range of motion, and occasional swelling. These signs and symptoms can significantly limit activities of daily living [41]. Conservative treatment with nonsteroidal anti-inflammatory drugs, steroids injections, splinting and therapy may relieve symptoms temporarily. However, once these treatment options fail, patients may require a more invasive treatment to relieve their symptoms [41, 45, 52, 3]. Arthrodesis, an artificial induction of joint ossification between two bones via surgery, provides a pain-free stable joint but sacrifices motion and fails to recover the biomechanics of the normal finger after the surgery [5, 32, 37, 41, 51]. Although the impact of arthrodesis on hand and finger function remains a matter of debate among surgeons, preoperative planning has to include a decision on the appropriate angle for arthrodesis [24, 25, 45, 51, 52, 3]. A fused joint alters the biomechanics and strength of

the finger. The objective of this research is to analyze how the distal interphalangeal (DIP) joint flexion-extension (FE) and maximum voluntary pinch forces of the index finger are affected under imposed proximal interphalangeal (PIP) joint constraint angles.

Several studies on hand and finger function under imposed joint constraints [51, 15, 3], as well as finger biomechanics [44, 47, 26, 27] were reviewed to enable us to place our work in perspective with respect to existing research. While these studies have significantly contributed to the understanding of finger and hand movement capabilities, there has not been an investigation on how the finger biomechanics and strength are affected under finger joint arthrodesis. The human finger contains tendinous mechanisms that are essential for proper control [27]. One such mechanism couples the DIP and PIP joints in the (unloaded) finger when flexed or extended [26]. This mechanism, however, is no longer coupling the motion of the DIP and PIP joints when the PIP joint is constrained because now the DIP joint can flex and extend independently [3]. Typically, a subject is unable to move the DIP joint separately. This is understandable, because the tendon of the Flexor Digitorum Profundus (FDP) acts on both the DIP and PIP joints simultaneously [4]. In addition, the strength of the finger depends on the anatomical structure and the maximum effort of each individual muscle involved.

The main purpose of this biomechanical study is to quantify and compare finger kinematics, index finger EMG during free DIP joint FE and maximal voluntary pinch, and pinch forces. The finger biomechanics and strength involved in movement and force application must be analyzed in order to better understand the impairment associated with fusion of an individual joint. In this study, a biomechanical and strength evaluation was conducted on the index finger to determine the PIP joint arthrodesis angle allowing for optimal free DIP joint FE activation and maximum voluntary pinch forces.

5.2 Methods and experimental setup

5.2.1 Participants

Five male right-handed subjects, aged from 24 to 35 years old, volunteered in this study. All participants had no previous history of upper extremity disorders. Prior to the data collection, subjects signed an informed consent document approved by the Stony Brook University Institutional Review Board.

5.2.2 Instrumentation

A seven-camera motion capture system (Vicon MX, Oxford, UK) at a sample frequency of 100 Hz, was arranged in a 2 m $\times$ 2 m square region for data collection. Three dimensional coordinate measurement was determined to be well within 0.5 mm [26]. Thirteen reflective markers were attached to the dorsal aspects of the thumb, index, and middle fingers and hand with double-sided tape. Figure 5.1 illustrates the marker placement for the 13 $\times$ 4 mm hemispherical markers. Markers were placed proximal to the joint on the distal head of the proximal bone [34]. Custom-made thermoplastic splints were used to constrain the PIP joint at distinct angles (Figure 5.1). One experimenter customized each PIP splint based on each individual finger length. Manual goniometers were used to verify the constraint angles and adjust the splints accordingly [3]. Kinematic data were reviewed immediately after testing to ensure proper data collection with minimal marker dropout. A mechanical pinch meter was used to collect index finger pinch strength data of each participant as they perform tip and chuck pinch (Figure 5.1). Index finger muscle activities were documented with two wireless surface electromyography (EMG) sensors placed on the volar and dorsal sides of the forearm to sense the FDP and the Extensor Digitorum (ED), respectively (Figure 5.1). These muscles were selected for their role in index finger flexion and extension. The FDP and ED data were collected at a sample frequency of 1000 Hz.

Figure 5.1: Thumb, index, and middle fingers postures with 4 mm markers attached, the PIP joint splinted, and wireless EMG sensors attached to the forearm during chuck pinch performance.

Setup: During measurements subjects were seated in a height-adjustable chair with the right shoulder in a neutral position, the elbow at approximately 90 ° of flexion, and the forearm in pronation. All fingers were flexed and relaxed with exception of the fingers which performed the movements instructed. Subjects were instructed to:

(1) Keep the wrist at a steady neutral position and with the index finger metacarpophalangeal (MCP) joint extended at approximately 0°, and continuously perform full FE movements of the DIP joint.

(2) Keep the wrist at a steady neutral position with the index finger MCP joint flexed at approximately 45°, and continuously perform full FE movements of the DIP joint.

(3) Maintain the wrist extended at approximately 30°, and pinch on a mechanical pinch meter, held by one experimenter, using the thumb and index finger.

(4) Maintain the wrist extended at approximately 30°, and pinch on a mechanical pinch meter, held by one experimenter, using the thumb, index, and middle fingers (Figure 5.1).

Participants performed 3 trials (5 seconds each) under two conditions: (1) unconstrained (UC) finger and (2) with the index finger PIP joint constrained to 0°, 20°, 30°, 40°, and 60° of flexion. Each subject performed a practice trial with the unconstrained and constrained finger before data recording.

5.2.3 Data processing

In order to analyze fingers motions, each marker was taken as a set of three points indicating the relative x, y, and z coordinates of the marker in space, relative to the Vicon coordinate system, or global coordinate system (GCS). A local coordinate system (LCS) is then embedded in the hand plane defined by the marker model and subsequent planes

and vectors are defined relative to the hand plane. Data were exported to and processed with MATLAB (MathWorks Inc., Natick, MA, USA) software package. Marker data were filtered using a second order Butterworth low-pass filter with 20 Hz cut-off frequency. Three vectors, one for each finger were created using markers placed on the MCP, PIP, and DIP joints, and the fingertips of the index and middle fingers. FE movements of the MCP, PIP, and DIP joints are calculated with respect to the plane defined by the markers placed on the hand (Figure 5.1). Thumb movements were described using a thumb plane defined by the markers at thumb carpometacarpal (CMC) and MCP joints as well as the index finger MCP joint. Likewise, movements of the CMC, MCP, and interphalangeal (IP) joints of the thumb are calculated with respect to the plane defined by the markers placed on the hand. Movements and joint angle calculations were performed according to Metcalf *et al.* [34]. Small rotations in other directions due to non-constant interphalangeal joint axes were neglected because of the assumption of parallel FE joint motions.

A running root-mean-square (RMS) of EMG signals was calculated for amplitude analysis of each test. A moving window with a frequency of 20 Hz was utilized for RMS calculation. In addition, a second order Butterworth low-pass filter with 10 Hz cut-off frequency was used to produce a smooth EMG RMS signal. Three peaks of EMG RMS values, corresponding to time instants when the DIP joint reached maximum flexion, were selected. The average value of the three EMG RMS peaks was used for analysis and comparison among the conditions considered. In order to analyze the thumb and fingers postures during tip and chuck pinch, the time for maximum EMG RMS value was utilized. This time was used to calculate the thumb and fingers postures during maximum pinch force exertion. Posture variation was analyzed with respect to the index finger UC condition. Furthermore, data from the pinch meter were recorded for each condition. All EMG RMS and force data were calculated as a percentage the maximal values obtained for each subject in each test performed.

5.2.4 Statistical analysis

Statistical significance of the simulated PIP joint constraint angles was analyzed with repeated measures ($p < 0.05$, significance level is 0.05) across the subjects using one-way analysis of variance (ANOVA). The simulated PIP joint constraint angles were randomized and assigned by one experimenter. The result of each condition was represented as the mean value across three measurements.

5.3 Results

5.3.1 Free DIP joint FE activation

The mean and standard deviation of the percentage of EMG RMS of the FDP and ED during FE of the DIP joint of the UC and constrained index finger with the MCP joint at 0° and 45° of flexion for all subjects are presented in Figure 5.2(a) and (b). The exertion of FE forces at the DIP joint did not change significantly ($p > 0.05$) among subjects under selected PIP joint constraint angles. The mean and standard deviation of the free FE range of motion (ROM) of the DIP joint when the index finger PIP joint was UC and constrained for all subjects is shown in Figure 5.3. The lower bound of the ROM of the DIP joint changed significantly ($p < 0.05$) among subjects under imposed PIP joint constraints whit the MCP joint at 0° and 45° of flexion, as shown in Figure 5.3. The upper bound of the ROM of the DIP joint did not vary significantly ($p < 0.05$) among subjects under imposed PIP joint constraints whit the MCP joint at 0° and 45° of flexion, as presented in Figure 5.3. Although the ROM of the DIP joint changed significantly ($p < 0.05$) with the MCP at 0°, it did not differ significantly ($p < 0.05$)with the MCP at 0° of flexion.

5.3.2 Pinch activation

The mean and standard deviation of the percentage of EMG RMS of the FDP and ED during tip and chuck pinch tests of the UC and constrained index finger for all subjects

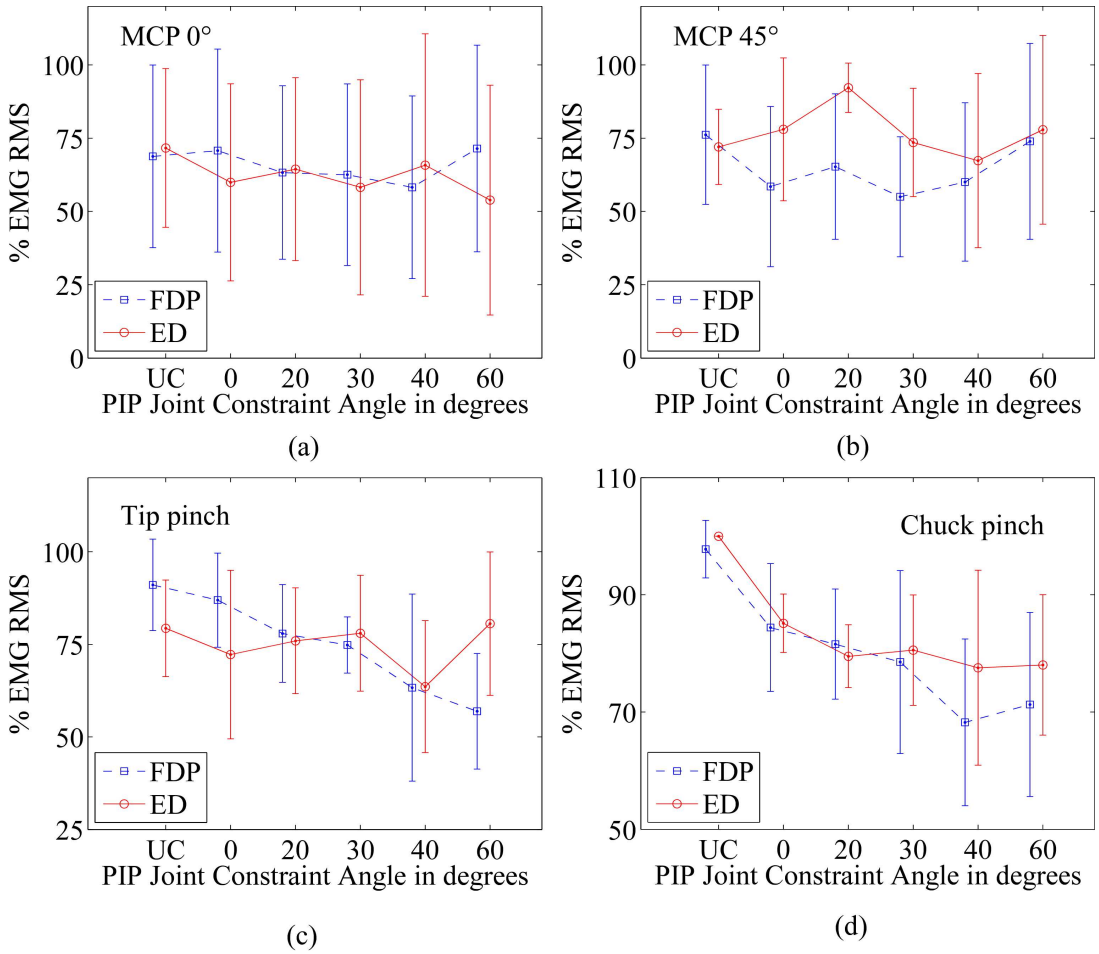

Figure 5.2: The mean and standard deviation of the percentage of EMG RMS activation of the FDP and ED during: (a) free FE of the DIP joint with the MCP joint at 0° of flexion; (b) free FE of the DIP joint with the MCP joint at 45° of flexion; (c) tip pinch; and (d) chuck pinch, of the UC and constrained index finger with experimental data of all subjects.

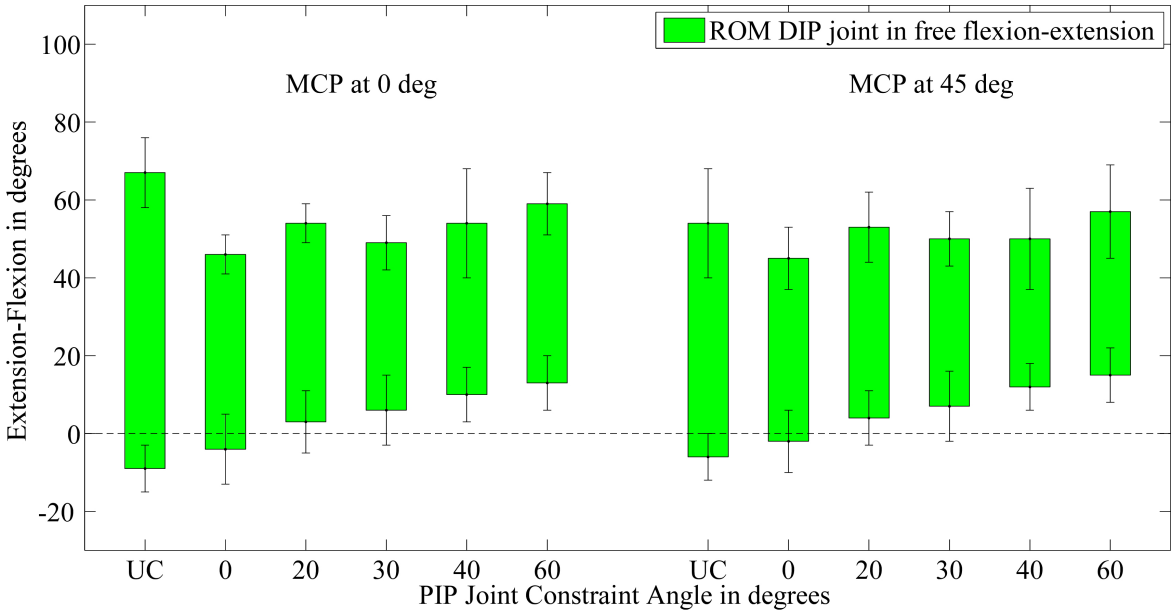

Figure 5.3: The free FE ROM of the DIP joint for all subjects when the PIP joint is unconstrained (UC) and constrained to selected angles and with the MCP joint at 0° and 45° of flexion.

are shown in Figure 5.2(c). The EMG RMS of the FDP of the index finger changed significantly ($p < 0.05$) among subjects under selected PIP joints constraints during tip pinch tests. The mean and standard deviation values of the FDP during tip pinch tests, shown in Figure 5.2(c), indicate the greatest force activation for the UC finger and when the PIP joint is constrained at 0° to 20° of flexion. The EMG RMS of the FDP decreases as the PIP joint constraint angle increases (Figure 5.2(c)). The EMG RMS of the ED did not change significantly ($p > 0.05$) among subjects under simulated PIP joint arthrodeses during tip pinch (see Figure 5.2(c)). The EMG RMS of the FDP and ED of the index finger changed significantly ($p < 0.05$) among subjects under selected PIP joints constraints during chuck pinch tests (Figure 5.2(d)). The mean and standard deviation values of the FDP during chuck pinch tests, shown in Figure 5.2(d), indicate the greatest force activation for the UC finger and when the PIP joint is constrained at 0° to 20° of flexion. Most of the values of EMG RMS of the FDP and ED decrease as the PIP joint constraint angle increases (Fig. 5.2(d)), except for the EMG RMS of the FDP when the PIP joint was constrained to 60° of flexion.

5.3.3 Pinch postures

The UC index finger condition was utilized to compare the thumb, index, and middle finger postures among subjects under simulated PIP joint arthrodesis during tip and chuck pinch. The mean and standard deviation for all subjects of the MCP abduction-adduction (AA), as well as MCP, PIP, and DIP FE joint angles of the UC index finger under tip and chuck pinch are 12° (SD 9°), 58° (SD 8°), 20° (SD 15°), and 7° (SD 11°), respectively. The MCP AA joint position did not differ significantly ($p > 0.05$) among subjects with respect to the UC condition under simulated PIP arthrodesis during tip and chuck pinch. The MCP FE joint angles were 65° (SD 9°), 57° (SD 9°), 48° (SD 14°), 46° (SD 17°), and 39° (SD 18°) for PIP joint constraints at 0°, 20°, 30°, 40°, and 60° of flexion, respectively. Similarly, the DIP FE joint angles were 7° (SD 14°), 10° (SD 12°), 5° (SD 22°), 3° (SD 23°),and 2° (SD 25°) for the PIP joint constraints analyzed. The MCP and DIP FE joint positions were

not significantly affected ($p > 0.05$) by simulated PIP arthrodesis with respect to the UC finger.

The thumb joint postures did not change significantly ($p > 0.05$) among subjects under simulated PIP joint arthrodeses of the index finger with respect to the UC condition during tip and chuck pinch. Likewise, the middle finger postures did not differ significantly ($p > 0.05$) among subjects under imposed PIP joint constraints with respect to the UC condition of the index finger during chuck pinch.

5.3.4 Pinch forces

The mean and standard deviation of the percentage of maximum force measured in the pinch meter during tip and chuck pinch with the index finger UC and constrained for all subjects are shown in Figure 5.4. The percentage of tip and chuck pinch forces did not change significantly ($p > 0.05$) among subjects under selected PIP joints constraints. The greatest values of the mean percentage of force for tip and chuck pinch are reached when the index finger PIP joint was UC and constrained to 0° and 20° of flexion.

The mean and standard deviation of the maximum tip pinch force, reached for the UC index finger, is 5.73 kg and SD 1.72 kg, respectively. Similarly, the mean and standard deviation of the maximum chuck pinch, reached when the PIP joint was unconstrained, is 8.27 kg and SD 1.34 kg, respectively.

5.4 Discussions

This study investigated the impact of simulated index finger PIP arthrodesis on finger biomechanics and pinch force. Individual and cooperative digits tasks were assessed with the index finger PIP joint UC and constrained to selected angles in order to understand the impairments associated with such conditions.

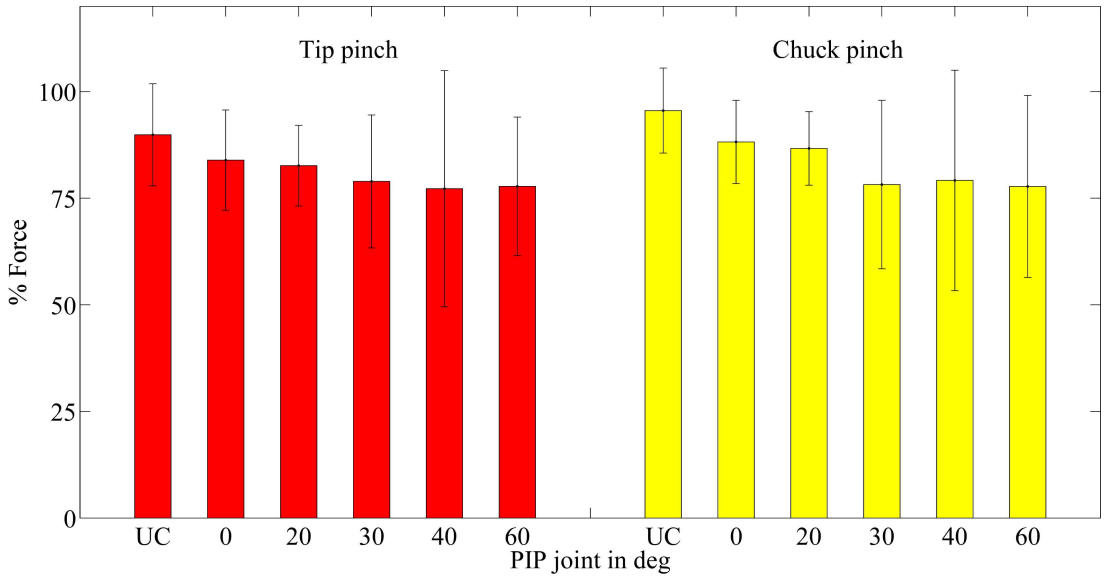

Figure 5.4: The mean and standard deviation of the percentage of tip and chuck pinch forces of the index finger with experimental data of all subjects under selected PIP joint constraints.

5.4.1 Free DIP joint FE activation

The free DIP joint FE activation of the index finger was analyzed under imposed PIP joint constraint angles. EMG RMS values of the FDP and ED indicate that varying angles of the PIP and MCP joint flexion have no significant influence on muscle activation forces used to freely flex and extend the DIP joint (see Figure 5.2(a) and (b)). This reuslt concurs with a previous cadaveric study reporting that DIP flexion resistance force did not differ significantly when the PIP joint was constrained to 0°, 30° and 60° of flexion and with the MCP joint at 0° of flexion [44]. It is known that the human finger contains tendinous mechanisms that are essential for proper control. One such mechanism couples the DIP and PIP joints in the finger when flexed or extended [3]. Our results suggest that the coupling mechanisms between the PIP and DIP joint do not have a significant influence on the forces required to freely flex and extend the DIP joint when he PIP joint is constrained to distinct angles. A similar conclusion can be drawn from the result obtained when the MCP joint is kept at 45° of flexion (Figure 5.2(b)). The DIP joint tended to slightly decrease its ROM as the simulated PIP joint arthrodesis angles increased (see Figure 5.3). This result agrees with the findings reported by Arauz *et al.* when measuring the DIP joint ROM for assessment of workspace attributes [3]. Free FE motions of the DIP joint, despite not presenting significant differences under selected PIP joint constraints for EMG RMS values FDP and ED, have a significant effect on the lower bound of the DIP ROM of the constrained finger. When the PIP is placed in flexion, the oblique retinacular ligament is on slack and is unable to pull on the lateral bands of the extensor mechanism. Therefore when the PIP is placed in flexion, the DIP will not be able to actively extend [30]. This would account for why the EMG activity doesn't present with significant differences but the DIP shows decreased ROM, particularly an extensor lag, as the PIP is constrained in greater flexion.

5.4.2 Pinch

Tip and chuck pinch were investigated with the index finger PIP joint UC and constrained to selected angles. EMG RMS values of the FDP indicate that the greatest muscle force was exerted when the index finger PIP joint was UC and constrained to 0° and 20° of flexion during tip and chuck pinch. A similar result was obtained for the ED muscle during chuck pinch. There were no significant differences under selected PIP joint constraints for the ED muscle force exertion during tip pinch.

The corresponding index finger postures during tip and chuck pinch indicate that the MCP and DIP joint positions were not significantly affected under simulated PIP joint arthrodesis with respect to the UC (natural) posture. However, our findings suggest that compensation for the loss of a degree of freedom in cooperation of the index finger and thumb, in tip pinch, as well as index and middle fingers and thumb, in chuck pinch, was only presented in the index finger. The postures of the thumb and middle finger did not change significantly under imposed PIP joint constraints with respect to the postures of the UC finger condition during tip and chuck pinch. These results are in agreement with previous studies reporting greater compensatory motion demands of the MCP and DIP joints in precision pinch [15, 51]. These results further support the thumb's primary role of providing a fixed support on which the index and middle fingers rest during tip and chuck pinch [15]. The UC PIP joint angle for tip and chuck pinch was approximately 20° of flexion. This result can be related to EMG RMS values of the FDP and ED during tip and chuck pinch, indicating greater activities with the PIP joint constrained to angles in the vicinity of the UC condition.

Although there were no significant differences for tip and chuck pinch forces under simulated index finger PIP arthrodesis among subjects, average results indicate greater force exertion for the UC condition. The mean value of chuck pinch force (8.27 kg) was 40% bigger than the tip pinch force (5.73 kg). This result concurs with a previous study reporting on the strength of tip and chuck pinch [42].

The interpretation of our data is that individuals without other hand impairments may adapt relatively well to PIP joint arthrodesis in tip and chuck pinch. Based on our results, a PIP joint arthrodesis at approximately 20° of flexion (close to a natural posture) may be optimal for tip and chuck pinch. Nonetheless, due to the fact that no significant differences in pinch and chuck force were found under imposed PIP joint constraints, the relevance of the pinch strength in selecting the appropriate PIP joint angle for arthrodesis may be of less interest when compared to other aspects such as precision handling functionality, workspace dimensions, and aesthetic preferences, among others [3, 15, 51].

Despite the fact that perfect immobilization of the PIP joint was not possible due to soft tissue and skin movement, custom-made thermoplastic splints constrain the motion of the PIP join to less than 5°. Perhaps this variation led to underestimating the impairment experienced by patients with surgical PIP arthrodesis. Moreover, arthrodesis of the PIP joint might affect some tendionous mechanism that could change the finger biomechanics. Furthermore, the impact of the loss of the PIP joint motion is probably underestimated when compared with the impact in individuals with arthritis involving multiple joints of the fingers and thumb because all subjects tested in this study had normal function of the hand.

5.5 Summary

This study reports the impact from simulated PIP arthrodesis in the biomechanics and pinch force of the index finger. EMG RMS values of the FDP and ED revealed that a PIP arthrodesis at 0° and 20° of flexion leads to a more natural finger posture during tip and chuck pinch. However, the significance of pinch force measurements was limited.

Chapter 6

Shoulder Joint Forces and Moments During Blocking in Football

6.1 Introduction

The purpose of this study was to develop an inverse dynamics model in order to estimate the shoulder joint forces and moments exerted by collegiate American football players during hitting of a blocking sled. The inverse dynamics model of articulated segments was utilized to characterize three-dimensional (3D) upper extremity joint kinematics and kinetics during simulated blocking using a custom-built sled including five load cells. The forces and moments at the upper extremity joints (glenohumeral (GH), elbow, and wrist) of one subject (one investigator) were determined during hitting of the blocking sled.

Blocking, a key part of American football, is the legal effort by an offensive player to obstruct a defender in order to complete successful running or passing plays. On running plays, offensive players block defenders in order to stop them tackling the ball carrier. On passing plays, offensive linemen aim to prevent rushing defenders from reaching the quarterback as he throws downfield. Injuries are common in the contact and collision sport of American football. As many as 1.5 million young men participate in American football in the United States [38]. It is estimated that 11% to 81% of participants will sustain an injury at some time while playing the sport [43, 23]. Since 1970s epidemiological studies have shown that the risk of injury is higher in older athletes and lower in teams with more

experienced coaches and more assistant coaches. These studies have shown that 51% of injuries occurred at training, and contact sessions were 4.7 times more likely to produce injuries than controlled sessions [38]. The shoulder is the fourth most common site of musculoskeletal injury behind the hand, knee, and ankle, composing roughly 10% to 20% of the total number of injuries encountered [7, 13, 23]. Linemen have been thought to be at higher risk for the development of posterior labral abnormalities and instability because of the loads on an outstretched arm when blocking [23]. Although not a very common injury, data from previous investigations [31, 23] confirm that linemen are more prone to this injury than players in other positions. Even though shoulder injuries are relative common in American football, there has been no study that has examined the shoulder forces and moments exerted by linemen during blocking.

Modeling of movement of the wrist and elbow is relatively simple, since both can be represented as two degree-of-freedom (DOF) joints. Nonetheless, the shoulder joint complex is an articulation that defies simple kinematic description [36]. Accurate determination of scapular position is difficult without skeletal pins, time-consuming palpation, or complex imaging techniques that are potentially invasive, expensive and impractical in most research settings [36]. Consequently, an approach to measure the upper limb relative to the trunk, previously used and supported by other investigators [36, 48], was utilized to investigate the shoulder forces and moments exerted by American football players during hitting of a blocking sled. Although the average impact force measured at the blocking sled has been reported [17], upper extremity joint impact loading has not been investigated.

This Chapter is organized as follows. Section 6.2 presents the materials and methods used to calculate the upper extremity forces and moments generated during blocking. The kinematic and kinetic models of the upper extremity are developed. In addition, the experimental setup used to evaluated the models during simulated blocking experiments is described. In Section 6.3, experimental results are presented. Discussions are presented in Section 6.4.

6.2 Material and methods

In the following, the methodology to model the upper extremity and determine the its joint forces and moments during simulated blocking are explained.

6.2.1 Kinematic model

The upper body model comprises seven segments including the thorax, upper arms, forearms, and hands, as shown in Figure 6.1. All joints are assumed to have fixed joint centers of rotation [36]. The upper extremity is a redundant manipulator able to move with multiple DOF. Rigid segments connected to several joints were utilized to generate the kinematic model of the upper extremity. The motions of the wrist joints were utilized in developing its kinematic model. In particular, flexion/extension and radial/ulnar deviation were modeled by a universal joint with two DOF. The elbow joint is modeled as rotating-hinge joint with two DOF, centered in the distal humerus. Forearm pronation and supination were modeled as rotations about an axis connecting the elbow and wrist joint centers. The glenohumeral (GH) joint was modeled as a ball and socket joint with three DOF, located at the center of the humeral head. To define the segments, reflective 14 mm spherical markers were placed on the subject. Joint axis were embedded at the joint centers, which were calculated using subject specific anthropometric data. In addition, the axial motion of the sled was modeled as a rigid body using three 14 mm spherical markers.

6.2.2 Kinetic model: body segment parameters

The mass and segment center of mass location of the hands, forearms, and upper arms, were estimated using measurements of weight and segment lengths of the subject by applying these measurements to anthropometric relations published in literature [50]. The three segments of the upper extremity were modeled as rigid bodies of uniform density. The principal moments of inertia on the upper arm and forearm segments were obtained by modeling them as conic shapes. The upper and lower circumferences of the upper arm and

forearm as well as the length of these segments were measured during the study [2]. The hand was modeled as a square cuboid with the lengths being measured from the wrist to the middle finger metacarpal and the height corresponding to the hand thickness (see Fig. 6.1).

6.2.3 Kinetic model: body segment angular velocity and angular acceleration

Three noncollinear virtual markers were equidistantly created in the LCS of the upper arm, forearm, and hand, respectively, with the LCS centered at center of mass of each segment. The global coordinates of these markers were utilized to calculate each segment acceleration, as well as the angular velocity and angular acceleration. Trajectories of the virtual markers were were filtered using a second order Butterworth low-pass filter with 20 Hz cut-off frequency. First and second derivatives were applied to the filtered data in order to determine velocities and accelerations of the there points on each segment.

We let the three noncollinear points of the segment under study be denoted by ${}^{B}P_i$ in the LCS and let ${}^{A}\mathbf{p_i} = [x_i(t)\ y_i(t)\ z_i(t)]^T$ be their corresponding position vectors in the GCS. The centroid C of the foregoing set has a position vector $\mathbf{c}$ that is the mean value of the three given position vectors [1], namely,

$$\mathbf{c} = \frac{1}{3}\sum_{1}^{3}\mathbf{p_i} \tag{6.1}$$

Likewise, if the velocities of the three points are denoted by $\dot{\mathbf{p}}_\mathbf{i}$, and their centroid by $\dot{\mathbf{c}}$ [1], one has

$$\dot{\mathbf{c}} = \frac{1}{3}\sum_{1}^{3}\dot{\mathbf{p}}_\mathbf{i} \tag{6.2}$$

Similary, if the accelerations of the three points are denoted by $\ddot{\mathbf{p}}_\mathbf{i}$, and their centroid by $\ddot{\mathbf{c}}$ [1], one obtains

$$\ddot{\mathbf{c}} = \frac{1}{3}\sum_{1}^{3}\ddot{\mathbf{p}}_\mathbf{i} \tag{6.3}$$

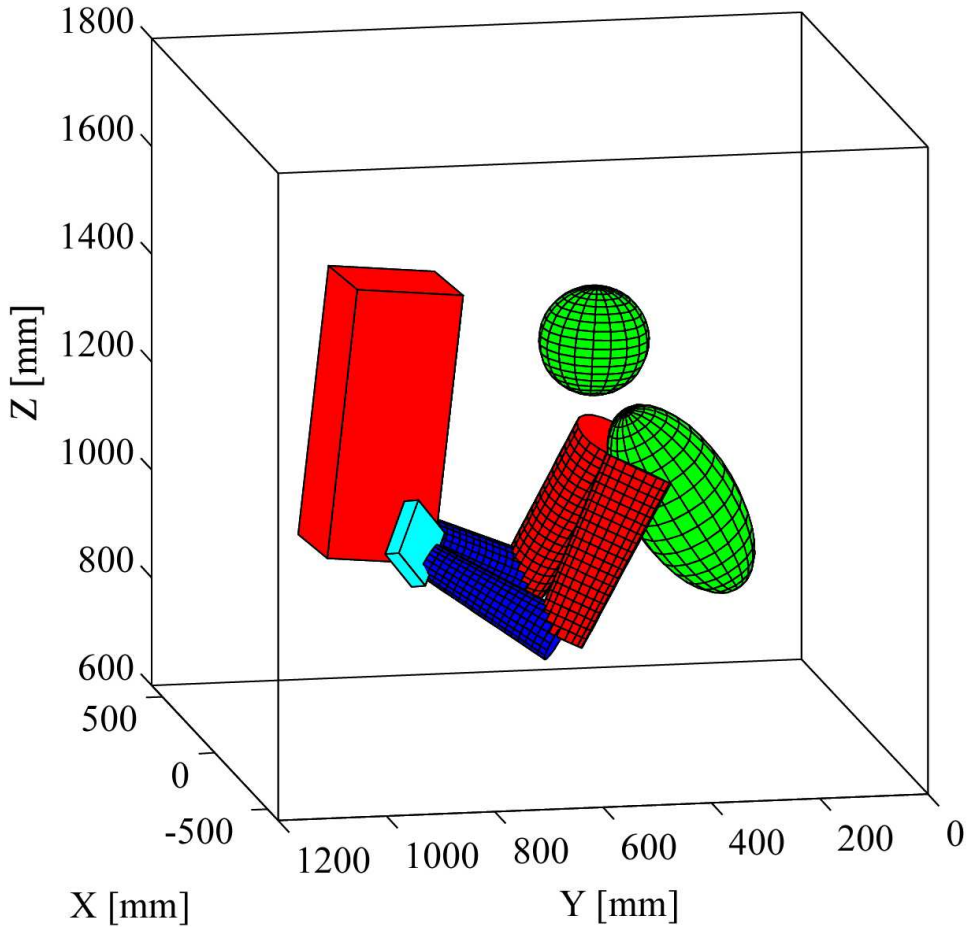

Figure 6.1: Hitting of the blocking sled simulation. The upper limbs modeled as rigid bodies of uniform density. The upper arm (red) and forearm (blue) modeled as conic shapes. The hand (cyan) modeled as a cuboid. The head and trunk (green) modeled as a sphere and ellipsoid, respectively. The moving part of the sled (red) modeled as a cuboid.

For a rigid body, the velocity of three given points can be expressed as

$$\dot{\mathbf{p}}_\mathbf{i} - \dot{\mathbf{c}} = \Omega(\mathbf{p}_\mathbf{i} - \mathbf{c}), \qquad i = 1,2,3 \tag{6.4}$$

Now we define a 3×3 matrix $\mathbf{P}$ as

$$\mathbf{P} = [\mathbf{p_1} - \mathbf{c} \quad \mathbf{p_2} - \mathbf{c} \quad \mathbf{p_3} - \mathbf{c}] \tag{6.5}$$

Upon differentiation of both sides of equation (6.5) with respect to time, one has

$$\dot{\mathbf{P}} = [\dot{\mathbf{p}}_\mathbf{1} - \dot{\mathbf{c}} \quad \dot{\mathbf{p}}_\mathbf{2} - \dot{\mathbf{c}} \quad \dot{\mathbf{p}}_\mathbf{3} - \dot{\mathbf{c}}] \tag{6.6}$$

Upon a second differentiation of both sides of equation (6.5) with respect to time, one obtains

$$\ddot{\mathbf{P}} = [\ddot{\mathbf{p}}_\mathbf{1} - \ddot{\mathbf{c}} \quad \ddot{\mathbf{p}}_\mathbf{2} - \ddot{\mathbf{c}} \quad \ddot{\mathbf{p}}_\mathbf{3} - \ddot{\mathbf{c}}] \tag{6.7}$$

Further, equation (6.4) can be written in matrix form as

$$\dot{\mathbf{P}} = \Omega\mathbf{P} \tag{6.8}$$

Upon multiplying both sides of equation (6.8) by $\mathbf{P}^T$ from the right, we obtain

$$\dot{\mathbf{P}}\mathbf{P}^T = \Omega\mathbf{R}, \quad \text{where} \quad \mathbf{R} = \mathbf{P}\mathbf{P}^T \tag{6.9}$$

Then, if we take the vector of both sides of equation (6.9), we obtain

$$\frac{1}{2}\mathbf{J}\,\omega = \text{vect}(\dot{\mathbf{P}}\mathbf{P}^T) \tag{6.10}$$

where $\mathbf{J}$ is defined as

$$\mathbf{J} = \text{tr}(\mathbf{R})\mathbf{I} - \mathbf{R} \tag{6.11}$$

Then, the angular velocity and angular acceleration of the segment can be calculated as follows [1]

$$\omega = 2\mathbf{J}^{-1}\text{vect}(\dot{\mathbf{P}}\mathbf{P}^T) \tag{6.12}$$

$$\dot{\omega} = 2\mathbf{J}^{-1}\text{vect}(\ddot{\mathbf{P}}\mathbf{P}^T - \Omega^2\mathbf{R}) \tag{6.13}$$

6.2.4 Kinetic model: Newton-Euler equations

Since ground reaction forces (contact sled forces) are measures in the GCS and the moments of inertia are known in the segment LCS, transformation matrices can be used in the kinetic calculation. All joint reaction forces are initially calculated in the GCS, and all joint moments are calculated in the the segment LCS. Load cells and makers from the sled enabled to estimate the force exerted by the players during hitting of the blocking sled.The videos simultaneously recorded during data collection were used in order to identify the initial and final time when the player makes contact with the sled's red man. Those times were used to select the interval of the sled forces acting on the player. Selected intervals of the sled forces were used in Newton-Euler equations of motion to determine the forces and moments at each upper extremity joint through the inverse dynamics method [40].

Equation (6.14) calculates the forces of each joint in the GCS as follows

$$\begin{cases} \mathbf{F}_W &= m_H(\mathbf{a}_H + \mathbf{g}) - \mathbf{F}_{SL} \\ \mathbf{F}_E &= m_F(\mathbf{a}_F + \mathbf{g}) - \mathbf{F}_W \\ \mathbf{F}_{GH} &= m_U(\mathbf{a}_U + \mathbf{g}) - \mathbf{F}_E \end{cases} \tag{6.14}$$

where $\mathbf{F}_W$, $\mathbf{F}_E$, and $\mathbf{F}_{GH}$ are the forces at the wrist, elbow, and glenohumeral joints, respectively. $\mathbf{F}_{SL}$ is the force measured at the sled. m_H, m_F, and m_U are the masses of the hand, forearm, and upper arm, respectively. $\mathbf{a}_H$, $\mathbf{a}_F$, and $\mathbf{a}_U$ are the accelerations of the center of mass of the hand, forearm, and upper arm, respectively. $\mathbf{g}$ is the acceleration of gravity (9.81 m/s^2).

Equation (6.15) calculates the moments of each joint in the segment LCS as

$$\begin{cases} {}^H\mathbf{M}_W &= {}^H\dot{\mathbf{H}}_H + {}^H\mathbf{r}_{DisH} \times {}^H\mathbf{F}_{SL} - {}^H\mathbf{r}_{ProxH} \times {}^H\mathbf{F}_W \\ {}^F\mathbf{M}_E &= {}^F\dot{\mathbf{H}}_F - {}^F\mathbf{M}_W + {}^F\mathbf{r}_{DisF} \times {}^F\mathbf{F}_W - {}^F\mathbf{r}_{ProxF} \times {}^F\mathbf{F}_E \\ {}^U\mathbf{M}_{GH} &= {}^U\dot{\mathbf{H}}_U - {}^U\mathbf{M}_E + {}^U\mathbf{r}_{DisU} \times {}^U\mathbf{F}_E - {}^U\mathbf{r}_{ProxU} \times {}^U\mathbf{F}_{GH} \end{cases} \tag{6.15}$$

where ${}^H\mathbf{M}_W$, ${}^F\mathbf{M}_E$, and ${}^U\mathbf{M}_{GH}$ are the segment moments at the wrist, elbow, and glenohumeral joints, respectively calculated at their corresponding LCS. ${}^H\dot{\mathbf{H}}_H$, ${}^F\dot{\mathbf{H}}_F$, and ${}^U\dot{\mathbf{H}}_U$

are the rates of change of angular momentum of the hand, forearm, and upper arm, respectively measured in the corresponding LCS. ${}^{H}\mathbf{r}_{DisH}$, ${}^{F}\mathbf{r}_{DisF}$, and ${}^{U}\mathbf{r}_{DisU}$ are the moment arms from the center of mass to the distal joint of the hand, forearm, and upper arm, respectively measured in the corresponding LCS. ${}^{H}\mathbf{r}_{ProxH}$, ${}^{F}\mathbf{r}_{ProxF}$, and ${}^{U}\mathbf{r}_{ProxU}$ are the moment arms from the center of mass to the proximal joint of the hand, forearm, and upper arm, respectively measured in the corresponding LCS. Note superscripts H, F, and U indicate forces and moments expressed in the LCS of the hand, forearm, and upper arm, respectively.

6.2.5 Data Acquisition

Participans: One investigator, with experience in football, volunteered in testing the experimental setup

Instrumentation: A ten-camera motion capture system (Vicon MX, Oxford UK) at a sample frequency of 100 Hz, was utilized for data collection. The three dimensional coordinate measurements were determined to be well within 0.5 mm [3]. For kinematic analysis, 37 reflective markers were attached to anatomical landmarks of the subject with double-sided tape. Figure 6.2 illustrates the marker placement of for the 37 $\times$ 14 mm spherical markers. A marker placed on lateral left side of the pelvis (LPLV) was used to define the 3D positions of the markers attached at the left and right side of the anterior superior iliac spine (LASI and RASI, as shown in Figure 6.2) when the player flexes his trunk completely occluded those marker with his body. The upper body model analyzed included the thorax, upper arms, forearms, and hands [36]. In addition, three markers placed on the sled were utilized to estimate the sled kinematics

To measure the blocking force, an instrumented blocking sled was custom built, as shown in Figure 6.3(a). A commercial available blocking sled, typically used in football training, was chosen for this study. This device implements a resistive element to absorb player impact. The blocking sled was bolted to five load cells (Omega LC101) symmetrically arranged in order to measure three orthogonal components of the ground reaction

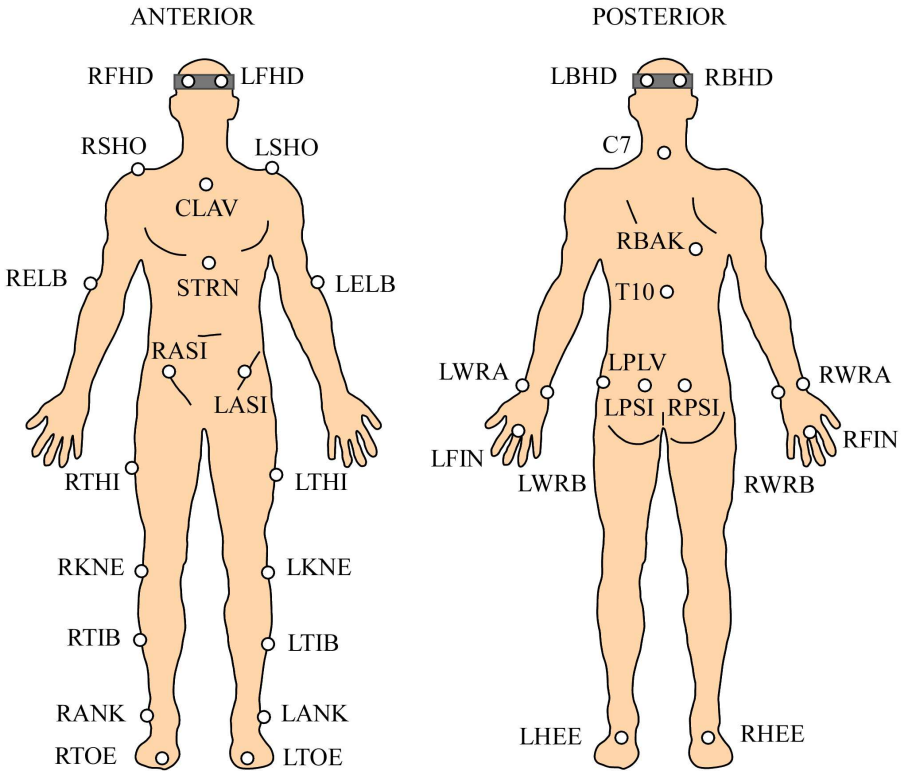

Figure 6.2: Full body marker set. Prefixes denote the following: L: Left, and R: Right. The following landmarks were used: suprasternal notch (CLAV), xiphoid process (STRN), spinous process at C7 (C7), spinous process at T10 (T10), acromial angle (BAK), acromioclavicular joint (SHO), lateral epicondyle of humerus (ELB), radial styloid (WRA), ulnar styloid (WRB), third metacarpal (FIN), temple (FHD), back head (BHD), anterior superior iliac spine (ASI), posterior superior iliac spine (PSI), lateral side of the pelvis (LPLV), femur (THI), lateral epicondyle of femur (KNE), tibia, (TIB), lateral malleoli (ANK), and distal interphalangeal joint of the first toe (TOE).

force, as illustrated in Figure 6.3(b). Each load cell can measure tension/compression forces in one axis. Four load cells are capable of measuring up to 8,900 N and one up to 11,150 N. The blocking sled reaction forces were calculated by summation of the projected components of each load cell on a global coordinate system used for analysis, as illustrated in Figure 6.3. In addition, force components due to acceleration of the moving red cushion (red man) and square piston with a mass of 20 kg, as indicated by the green arrow in Figure 6.3(a), yielding the resistive element, were calculated using equation (6.16) (see Section 6.2.6), and were included in the calculation of the sled blocking forces. Three reflective markers were placed on the head and lateral sides of the sled's red man, as indicated in Figure 6.3(a), to measure the sled kinematics. Load cell outputs were recorded at 1000 Hz. All data were synchronized using the motion capture system (Vicon MX, Oxford UK). No shear forces were recorded due the limitation of the load cells. Each load cell was calibrated individually. A controlled force was applied along the tension/compression axis of each load cell using the setup illustrated in Figure 6.4. Each load cell was calibrated using four compression loads as described in Section 6.2.6. Distinct loads were utilized with an input DC voltage of 12 V in order to determine the gains required to quantify the axial force on each load cell.

Videos simultaneously recorded during data collection were used to identify the period of time when the player makes contact with the sled's red man.

Setup: The we subject hit the blocking sled one time, as presented in Figure 6.5, in each of these conditions:

(1) An impulsive hit to the blocking sled: the time the player is in contact with the sled less than 1 second.

(2) A sustained hit to the blocking sled: the time the player is in contact with the sled less at least 2 seconds.

The blocks were recorded for analysis. The subject was asked to perform the block

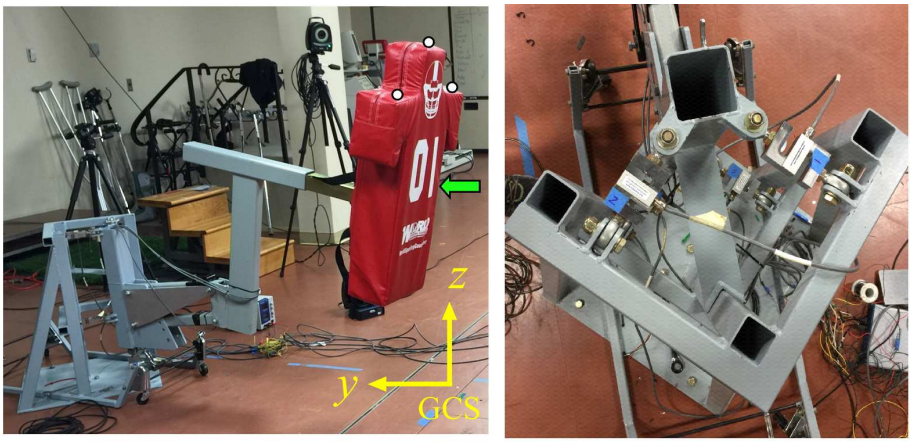

(a) (b)

Figure 6.3: (a) Custom built blocking sled, and (b) load cells bolted to the blocking sled and ground.

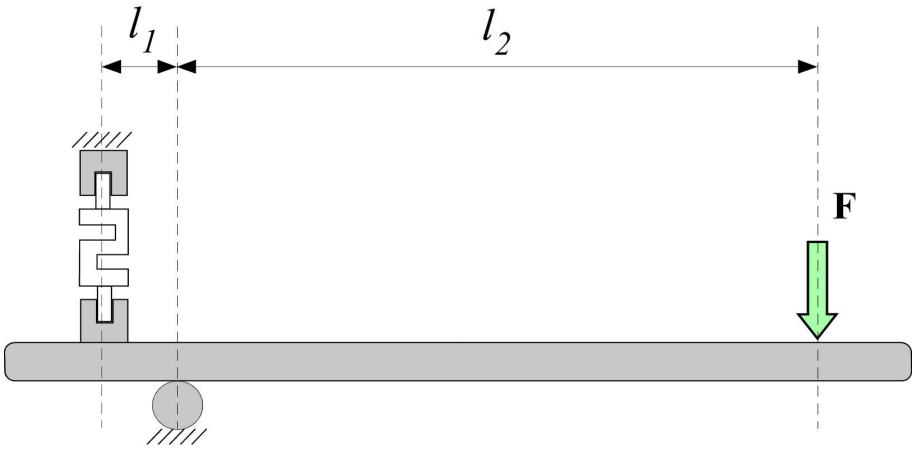

Figure 6.4: The schematic diagram of the setup used for load cell calibration.

as required in the in the Laws of the Game. He was advised to hit the blocking sled as he would normally do on the field during a competitive match or during practice [46]. The subject performed a practice trial under each condition before data recording.

6.2.6 Data processing

In order to analyze upper body motions, each marker was taken as a set of three points indicating the relative x, y and z coordinates of the marker in space, relative to the Vicon coordinate system, or GCS. A local coordinate system (LCS) is then embedded in the trunk plane defined by the marker model and subsequent planes and vectors are defined relative to the trunk plane. Data were exported to and processed with MATLAB (MathWorks Inc., Natick, MA, USA) software package. Data were filtered using a second order Butterworth low-pass filter with 20 Hz cut-off frequency. Shoulder offset, elbow and wrist width, as well as hand thickness were measured for the subject in order to identify joint centres. The thorax origin was calculated using the four markers attached to this segment. The orientation of segments was identified by calculating three orthogonal axes directions (x-axis sagittal, y-axis transverse, and z-axis longitudinal). Two of these axis directions were calculated directly from marker data, and the third was determined perpendicularly to the plane defined by the direction of these two axes. The GH joint center was calculated from the thorax segment using the measured shoulder offset (the longitudinal distance from the shoulder marker to the GH joint center). To calculate the upper extremity from the proximal and distal direction, the joint centers of the proximal segment were used. The marker of the joints, the wand markers of the segments (defined by three markers attached to each segment), and the joint widths (elbow and wrist width, as well as hand thickness) were utilized to determine the distance from the joint markers to the joint centers, as illustrated in Figure 6.6. The orientations of the extremity segments were labeled by longitudinal z-axis, the transverse y-axis (from the distal joint center to the distal joint marker) and the perpendicular sagittal x-axis, with the distal joint center as the origin [49, 36], as illustrated

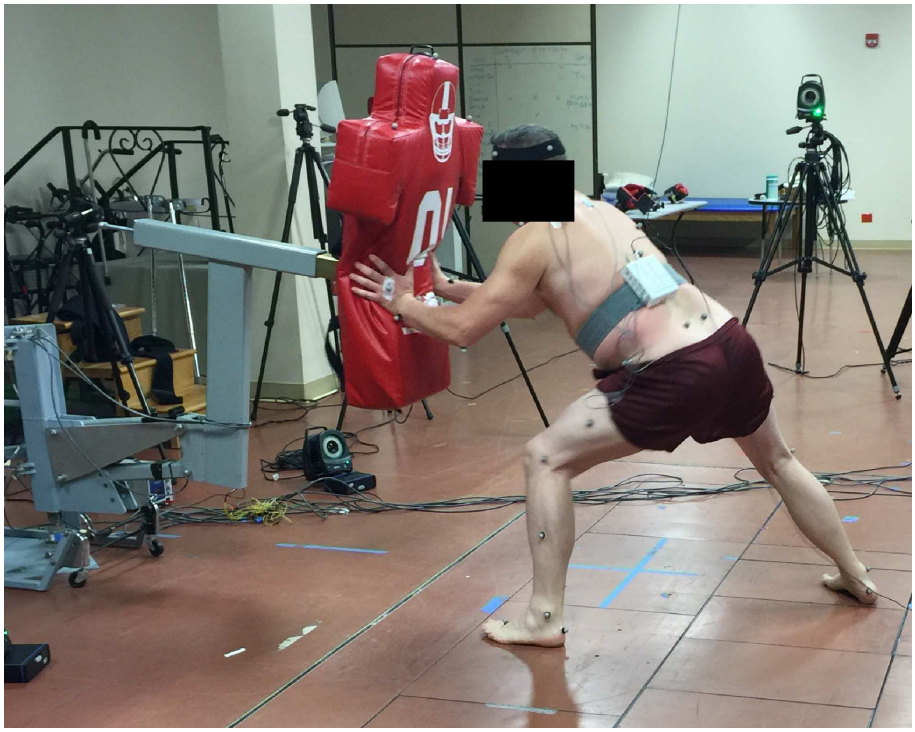

Figure 6.5: Player hitting the blocking sled as set-up in the present study

in Figure 6.8. Three dimensional joint angles were calculated by the relative orientation of the proximal and distal segments. The joint flexion angles (shoulder, elbow, and wrist) were the angles determining the transverse axes of the proximal and distal segments, as shown in Figure 6.8. The angle directions were defined as positive for shoulder, elbow and wrist flexion and negative for shoulder and wrist extension. The shoulder internal rotation angle was defined as the rotation of the humerus along the longitudinal axis of the humerus. A positive value corresponds to an internally rotated humerus. The forearm pronation and supination was calculated between the sagittal axis of the wrist and the sagittal axis of the humerus, where a positive value corresponded to a forearm pronation. Wrist flexion and extension as well as radial and ulnar deviation were measured relative to the LCS embedded in the wrist, as presented in Figure 6.8. Shoulder adduction and hand ulnar deviation were defined as positive. The thorax rotation angle was defined between the projected sagittal x-axis of the thorax and the y-axis of the GCS. Finally, the thorax or trunk flexion was calculated between the projected and sagittal x-axis of the thorax [49, 36], as illustrated in Figure 6.7.

Compression loads of 1,120 N, 2,220 N, 3340 N, and 6450 N were used to calibrate each load cell. The values of voltage obtained for each load was fitted to a linear relations and those relations were used to calculate the forces measured at each load cell during hitting of the blocking sled.

Figure 6.9(a) illustrated the schematic representation of the blocking sled. The free-body diagram of moving part of the sled (part 1) is illustrated in Fig. 6.9(b). The load cells kinetic data were re-sampled to 100 Hz and combined with the kinetic data from the moving part of the sled in order to provide the total force of hitting the blocking sled using equation (6.16) as follows.

$$\mathbf{F}_{SL} = m_s(\mathbf{a}_{SL} + \mathbf{g}) - \mathbf{R} \tag{6.16}$$

where $\mathbf{F}_{SL}$ is the total force of hitting the blocking sled, $\mathbf{R}$ is the ground reaction force measured at the load cells, m_s is the mass of the moving part of the sled, $\mathbf{a}_{SL}$ is acceleration

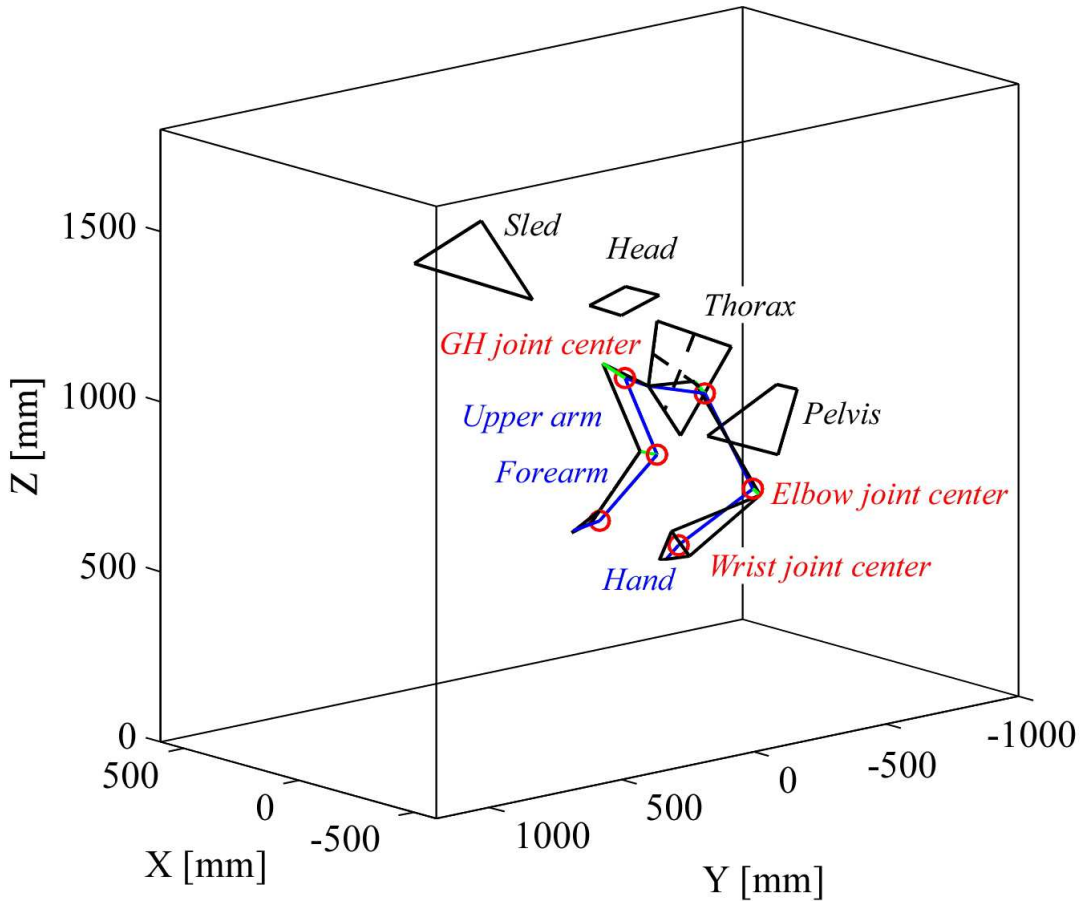

Figure 6.6: Segment model of the upper body constructed with markers placed on anatomical landmarks of the subject. Red circles correspond to the joint centers of the upper limbs. Segments in blue illustrate the segment model of the upper limbs (upper arm, forearm, and hand). The head, thorax, pelvis, upper arms, forearms, and hands are represented by lines in black connecting surface markers attached to each segment. The black lines in a triangular shape above the marker model corresponds to the marker model of the moving part of the sled.

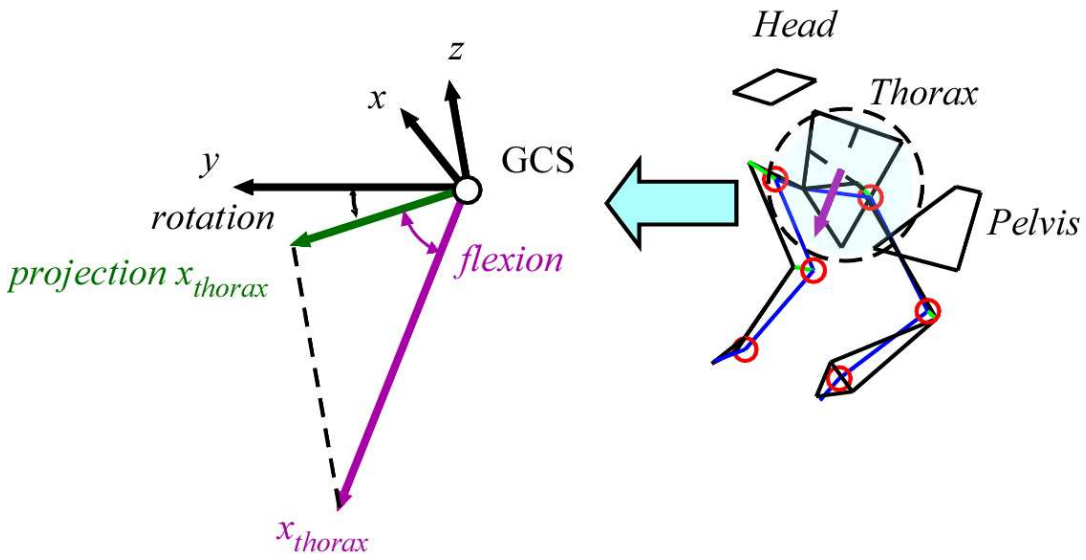

Figure 6.7: Orientation and joint angles of the thorax segment with respect to the GCS.

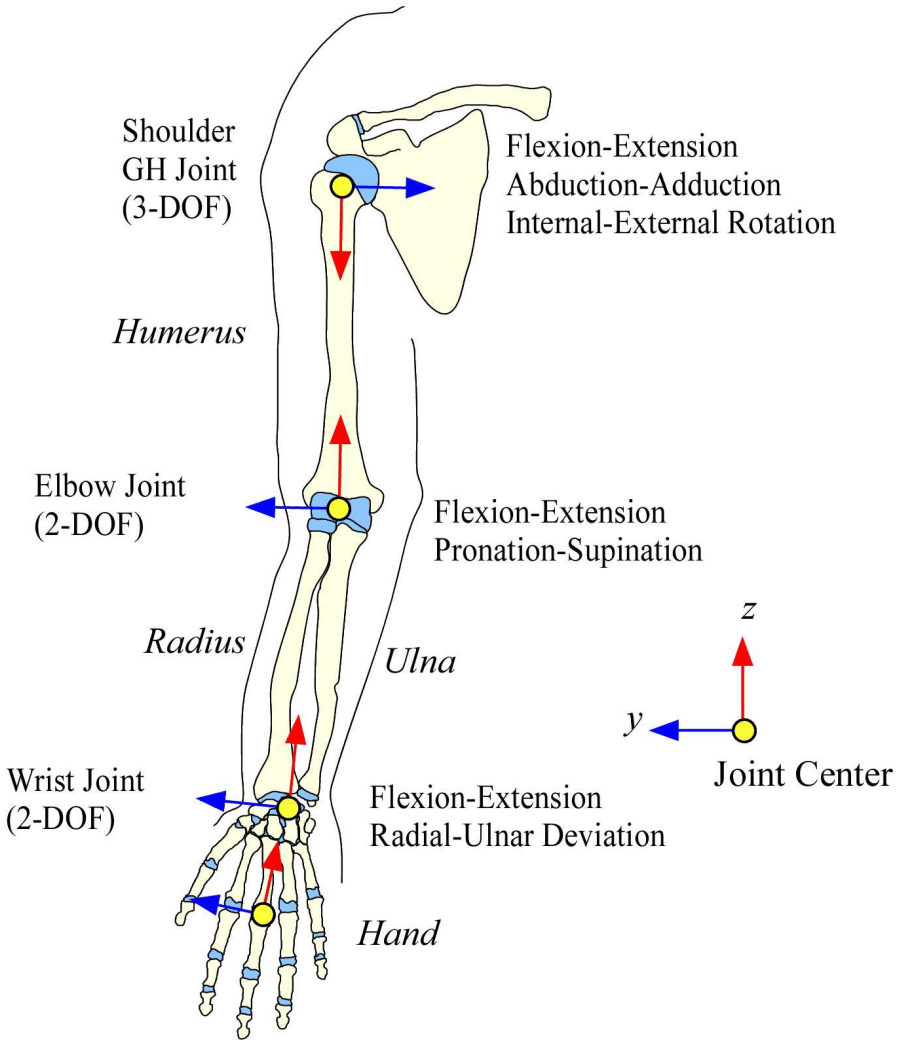

Figure 6.8: Schematic diagram of the upper extremity joint centers and their axes of motion.

computed relative to the global coordinate system (GCS) using the markers placed on the moving part of the sled, and **g** is the acceleration of gravity.

6.3 Results

In the following, the result of the measurements for the parameters of the subject are presented. In addition, the calibration of the load cells is described. Moreover, forces measured at the sled are presented. Finally, the result of the forces and moments measured at the upper extremity joints is presented for the two hits considered.

6.3.1 Subject parameters

The mass and height of the subject were 100 kg and 185 cm, respectively. The segment lengths of the upper upper arm, forearm, and hand were calculated using the average distance between the estimated centers of the GH and elbow joints, the elbow and wrist, and the wrist and hand joints, respectively. The lengths of the upper upper arm, forearm, and hand were $l_{ua} = 338$ mm (SD 9 mm), $l_f = 277$ mm (SD 2 mm), $l_h = 100$ mm (SD 4 mm), respectively.

6.3.2 Load cell calibration

Load cells were calibrated using compression loads of 1,120 N, 2,220 N, 3340 N, and 6450 N. Figure 6.10 illustrates the calibration results of each of the five load cells used in this study. The values of voltage obtained for each load applied and the fitted linear equations are illustrated in Figure 6.10. All load cells present a linear relation between the load applied and the output voltage for the range of the load values utilized. The average and standard deviation of the signal-to-noise ratio for the load cells was 8.81 dB (SD 8.17 dB).

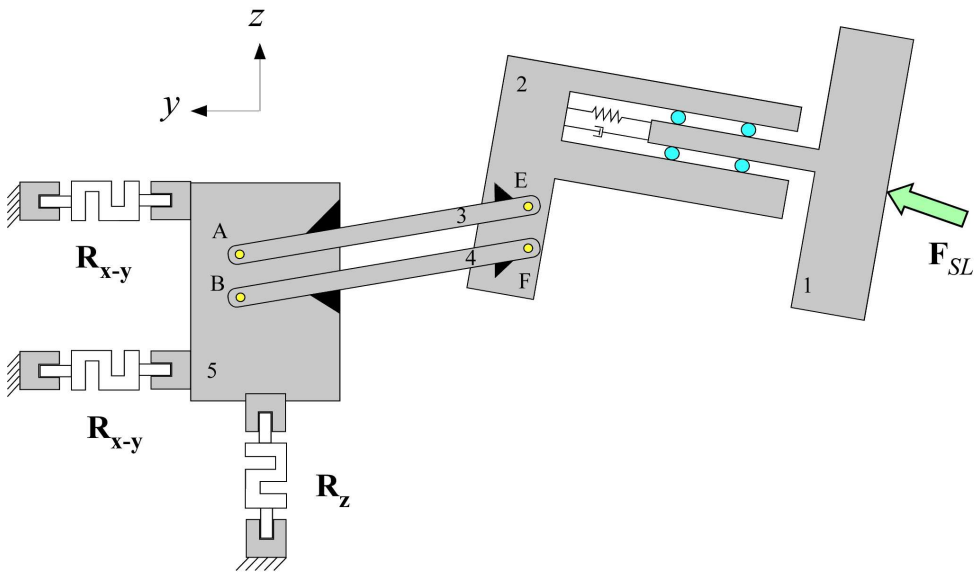

(a)

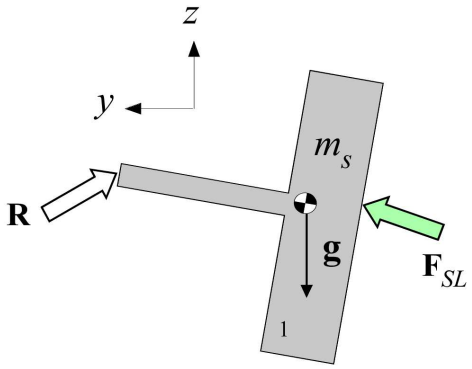

(b)

Figure 6.9: (a) The schematic diagram of the custom built blocking sled, and (b) free-body diagram of the moving part of the sled during hitting.

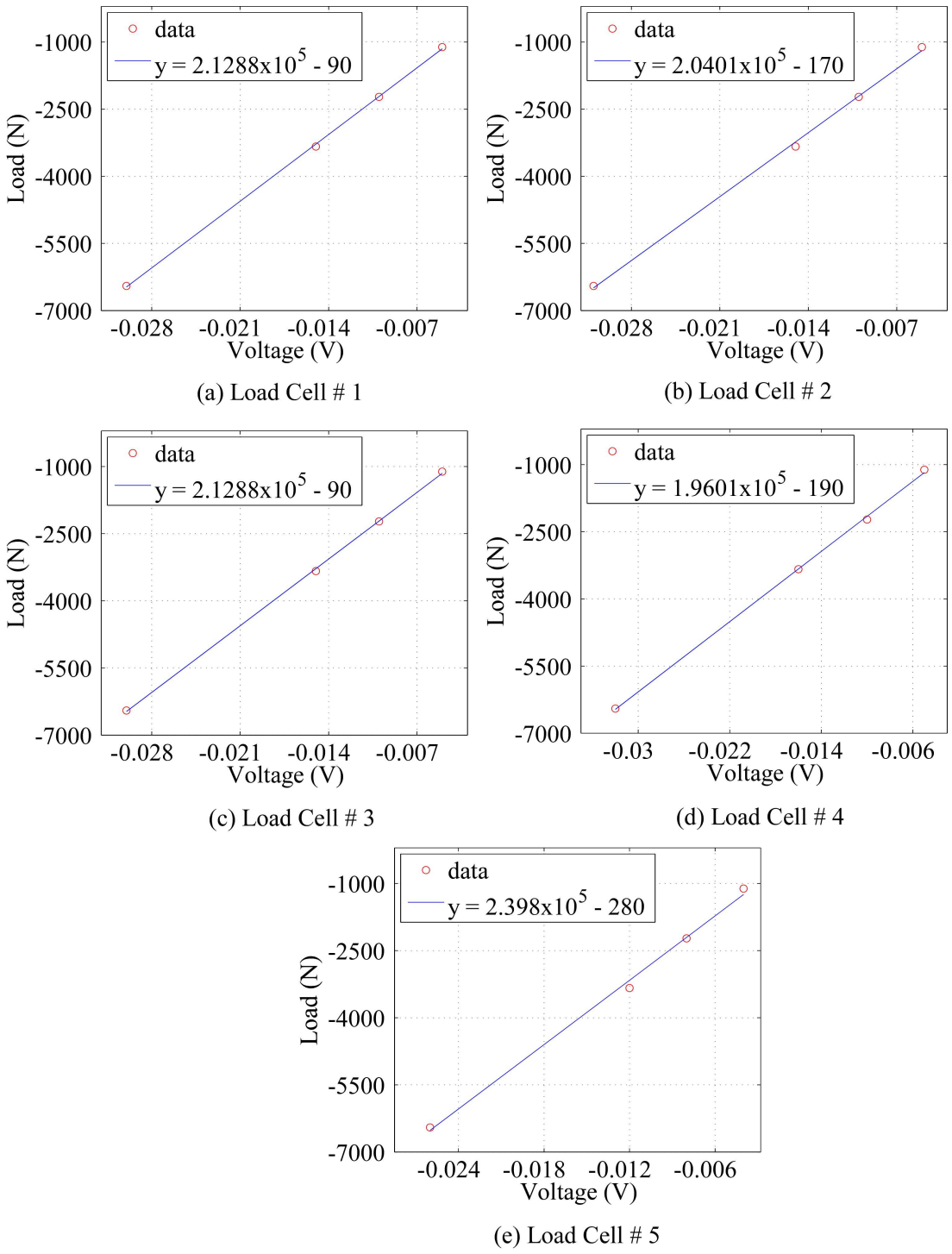

Figure 6.10: Experimental calibration of the five load cells (a-e). The load cells input DC voltage was 12 V.

6.3.3 Sled forces

Sled forces were calculated with respect to the GCS. The force component normal to the player was along the y-axis, and the z-axis is along the vertical plane. Figure 6.11(a) presents the result of the forces measured at the sled (only when the player makes contact with the sled) during an impulsive hit to the blocking sled. The maximum 3D net force at the sled for the impulsive hit was approximately 2000 N. The time duration of the hit was approximately 0.62 seconds (from time 2.08 to 2.7 seconds). Figure 6.11(b) presents the result of the forces measured at the sled during a sustained hit to the blocking sled. The maximum 3D net force at the sled (only when the player makes contact with the sled) for the sustained hit was approximately 2200 N. The time duration of the hit was approximately 3.13 seconds (from time 0.52 to 3.65 seconds).

6.3.4 Forces and moments at the upper limb joints.

The forces and moments at the joints of the left upper limb were calculated. Since measurements of the force at the sled provides only one force vector, it was assumed that this force vector was equally acting on each upper limb. The sled force data were used in equations (6.14) and (6.15) to determine the forces and moments at each joint of the left upper limb. Figure 6.12 shows the forces at the wrist, elbow, and GH joints measured with respect to the GCS for the impulsive hit to the blocking sled. The maximum magnitude of the forces at each joint was approximately 1000 N. Figure 6.13 shows the forces at the wrist, elbow, and GH joints measured with respect to the GCS for the sustained hit to the blocking sled. The maximum magnitudes of the forces at each joint were approximately 1000 N.

The moments generated during hitting of the blocking sled were calculated in the LCS of each segment. Moments generated during an impulsive hit to the blocking sled, shown in Figure 6.14, indicate that the maximum magnitude of moment at the wrist joint was approximately 60 N-m. Likewise, the maximum magnitudes of moment at the elbow

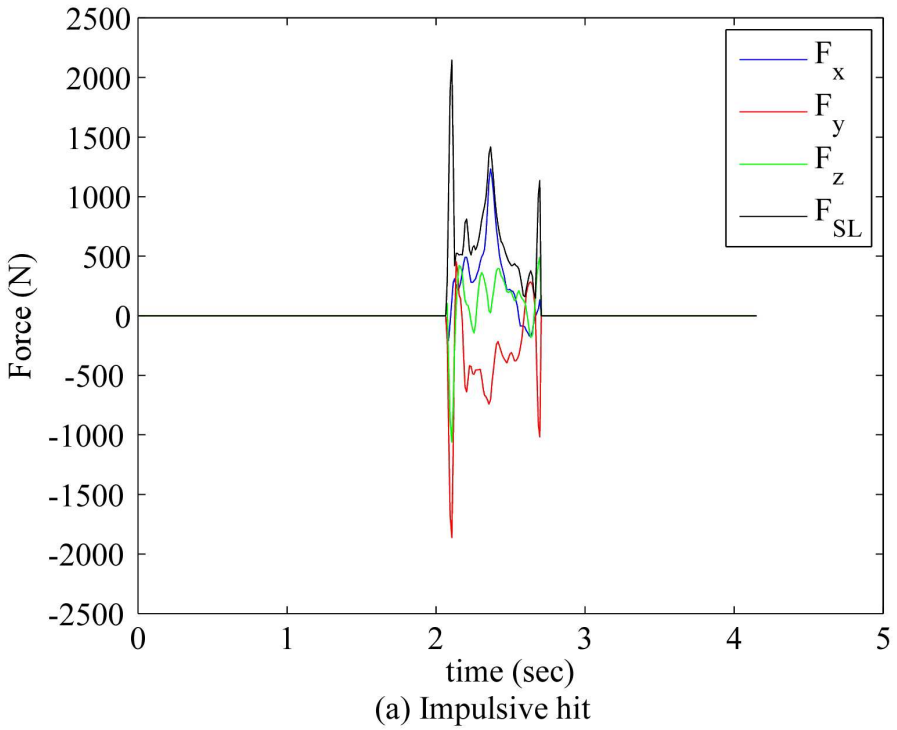

(a) Impulsive hit

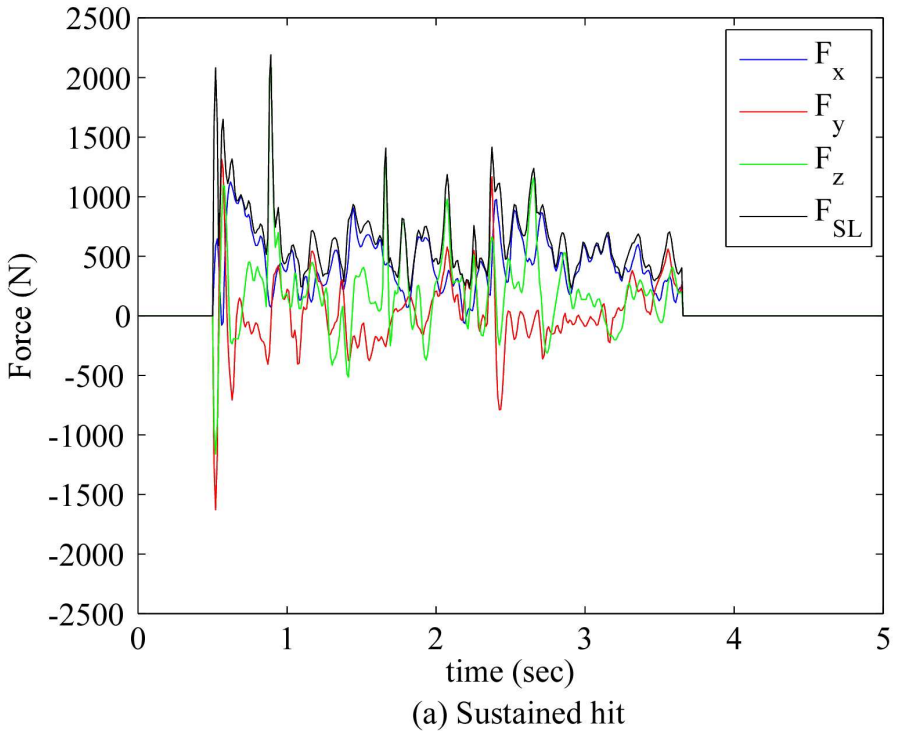

(a) Sustained hit

Figure 6.11: Forces measured at the sled during impulsive and sustained blocking hits. The black solid line corresponds to the 3D force magnitude.

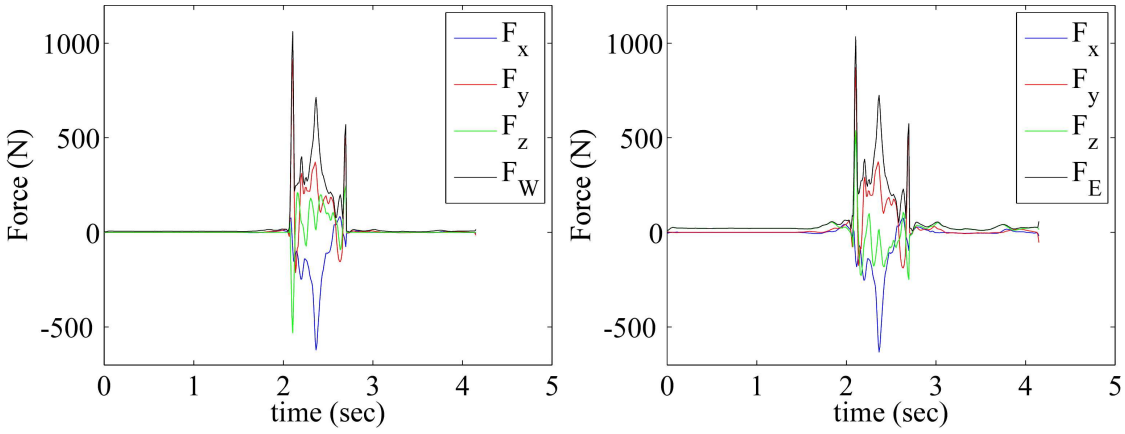

(a) Forces at the wrist joint

(b) Forces at the elbow joint

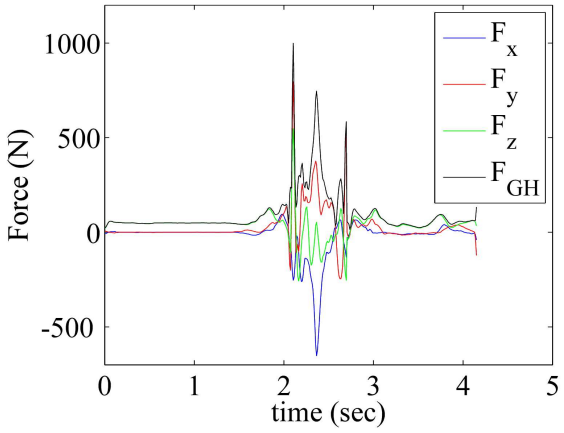

(c) Forces at the GH joint

Figure 6.12: Measurement of forces at the left upper limb joints in the GCS for the impulsive hit to the blocking sled. The black solid line corresponds to the force magnitude.

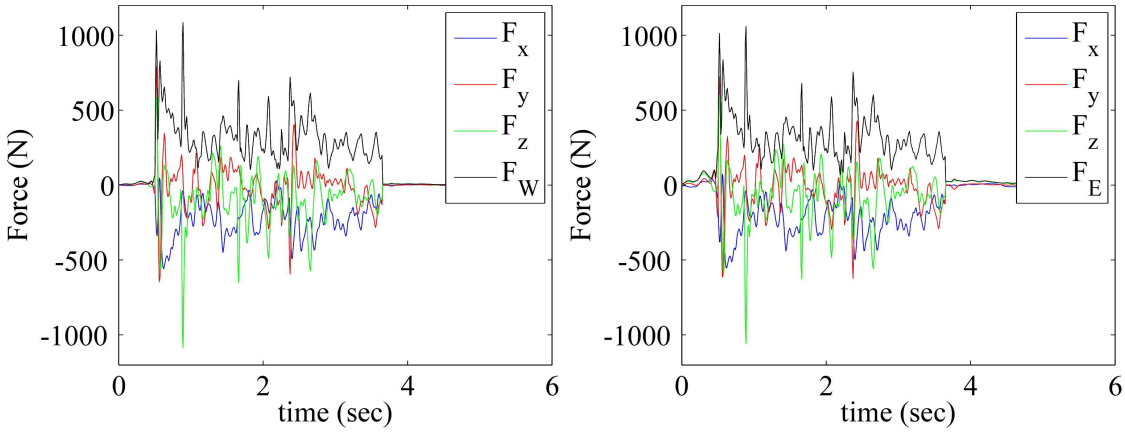

(a) Forces at the wrist joint

(b) Forces at the elbow joint

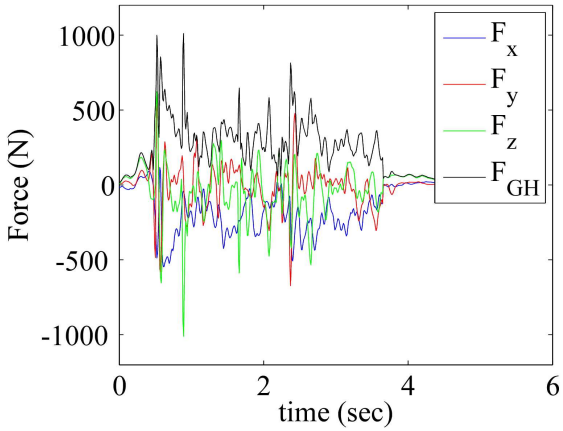

(c) Forces at the GH joint

Figure 6.13: Measurement of forces at the left upper limb joints in the GCS for the sustained hit to the blocking sled. The black solid line corresponds to the force magnitude.

and GH joints were approximately 150 and 330 N-m, respectively. Figure 6.15 shows the estimation of the moments at the wrist, elbow, and GH joints measured with respect to the LCS for the long hit of the blocking sled. The approximate maximum magnitudes of moment at the wrist, elbow and GH joints are 80, 320, and 440 N-m, respectively.

6.4 Discussion

Measurements of subject parameters are in agreement with athropometric measurements reported in literature [50]. Although those measurements were used to determine mass of each segment, the body mass index(BMI) [46] can be used to adjust for larger athletes.

The inverse dynamics model calculated the upper limb joint forces and moments generated during hitting of a custom-built blocking sled in one volunteer. Model accuracy was acceptable as long as the reaction forces measured at the sled were grater than the resolution of the load cells (between 200 and 300 N). It is expected that the accuracy of the proposed model will be improved by including force sensing devices with better resolution than the load cells utilized. In particular, since measurements of the force at the sled provides only one force vector, assumptions that this vector acts equally on each upper limb were made. A more innovative design of the blocking sled incorporating sensors to measure forces and moments at each upper limb will increase the model accuracy.

Since the participant involved in this study has not been an active player for several years, the magnitude of the blocking forces measured at the sled (2200 N) were 30% lower than those reported in previous studies conducted with collegiate football linemen (3013 $\pm$ 598 N) [17]. In addition, despite having measured a similar force at the blocking sled, the magnitudes of the moment at the shoulder joint differed by approximately 25% for impulsive and sustained hits to the blocking sled (330 and 440 N-m). This result indicates the kinematic and dynamic variation of the upper limb under two distinct hits.

The exploratory protocol to measure the forces and moments at the upper limbs of

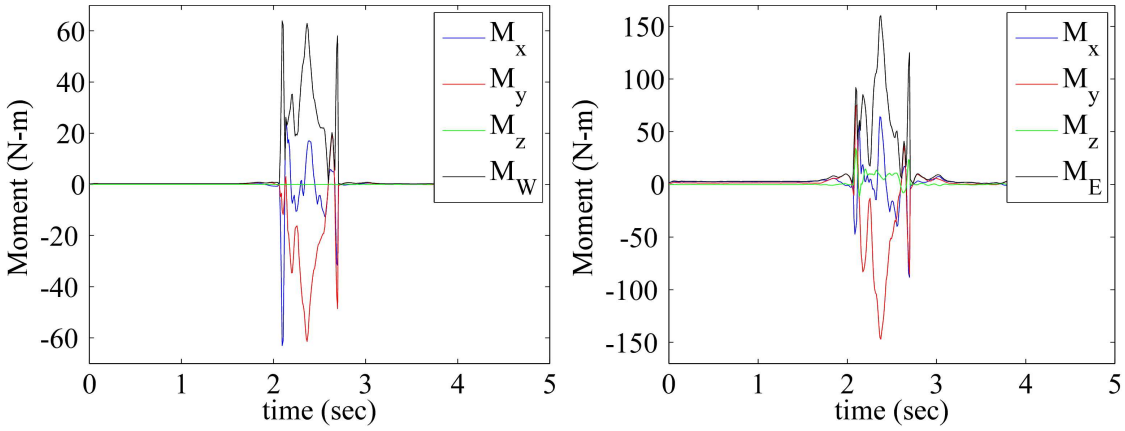

(a) Moments at the wrist joint

(b) Moments at the elbow joint

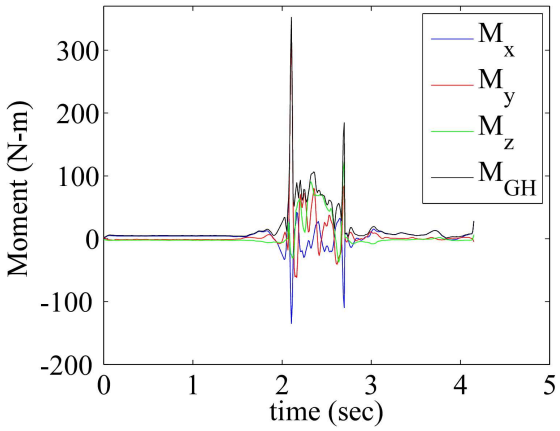

(c) Moments at the GH joint

Figure 6.14: Measurement of moments at the left upper limb joints in the LCS for the impulsive hit to the blocking sled. The black solid line corresponds to the moment magnitude.

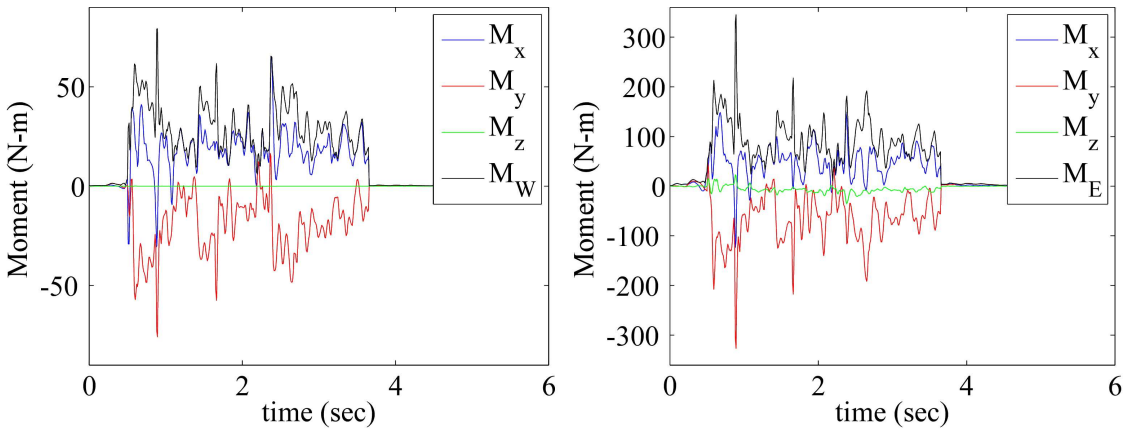

(a) Moments at the wrist joint

(b) Moments at the elbow joint

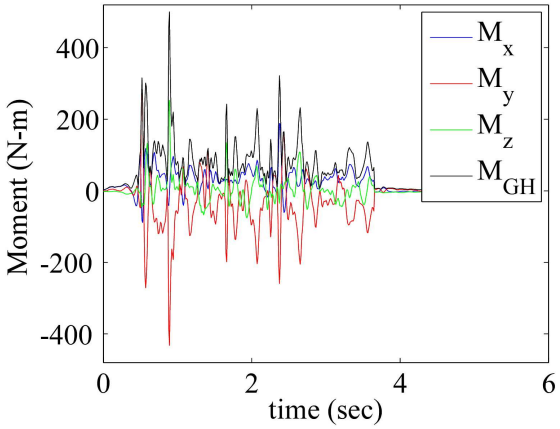

(c) Moments at the GH joint

Figure 6.15: Measurement of moments at the left upper limb joints in the LCS for the sustained hit to the blocking sled. The black solid line corresponds to the moment magnitude.

American football players during simulated blocking has shown that it is possible to apply an inverse dynamics model. However, further improvements in the force sensing devices may be required in order to increase the accuracy of the outputs of the model.

6.5 Summary

In this chapter, an inverse dynamics model was utilized to determine the upper limb joint forces and moments during blocking. Model development and the methodology used to measure the forces and moments were introduced. The experimental setup and data acquisition were discussed. The model was applied in experiments conducted on one subject who hit an instrumented blocking sled. The model and methodology implemented worked well on measuring the joint forces and moments generated at the upper limb when the subject hit the blocking sled. The future work will include the implementation of the model and experimental protocol on assessment of collegiate American football players during blocking.

Chapter 7

Conclusions and Future Work

7.1 Conclusion

This dissertation critically examined and implemented mechanical models to investigate the appropriate finger arthrodesis, as well as shoulder joint forces and moments during blocking in American football. The following attempts to reach overall conclusions of the findings presented in the preceding chapters.

7.1.1 Finger arthrodesis

In this dissertation, the application of novel systematic and analytical methodologies to investigate the index finger PIP arthrodesis found optimal constraint angles based on several finger criteria such as workspace, manipulability, functional ROM, biomechanics, and strength. Although it is not possible to find a unique PIP constraint angle that simultaneously optimize each criterion, our studies provide analytical methodologies that allow for comparison among several criteria, before the arthrodesis angle is selected, and customize for this angle for each patient in order to enhance not only finger performance but also the quality of life after surgery or during rehabilitation. Hence, application of the proposed methods results in better surgical planning and rehabilitation techniques helping surgeons, clinicians, and therapists to make more informed decisions on the appropriate angle for arthrdesis.

7.1.2 Shoulder joint forces and moments during blocking

An inverse dynamics model of the upper limb was implemented to measure the impact blocking forces, as well as upper limb joint forces and moments during simulated blocking. In particular, the shoulder joint forces and moments were compared for two types of hits. Our results indicate that the inverse dynamics model worked well on measuring the upper limb joint forces and moments.

7.2 The proposed future work

Possible future work which follows the research and development presented in this dissertation includes the following.

7.2.1 Hand and finger rehabilitation

To begin with, the proposed methodologies and finger models can be implemented in the field of ergonomics to assist in the design of hand-held devices. In addition, the use of the proposed methodology can be extended to define other body segment models such as toes or thumbs which may require arthrodesis surgical procedures. Moreover, we should explore the design of bio compatible mechanical devices that allow an effective and stable finger joint replacement without sacrificing motion (arthroplasty). Finally, it will be important to explore the dynamic manipulation of the hand and fingers. Further development of hand and finger models along with kinematic and kinetic information obtained from experiments will allow to better understand how people manipulate objects.

7.2.2 Sports - American football

We have developed an inverse dynamics model to be used in measuring upper limb joint forces and moments exerted by football players during simulated blocking. The proposed model will be used to explore skill deficiencies due to fatigue and their role on injuries. In addition, the model can be implemented to investigate the influence of player

size and skill level on the magnitude of upper limb joint forces and moments. Furthermore, EMG information measured from several muscles at the shoulder complex can be used to developed and assess biomechanical models of the upper arm and shoulder complex. Finally, it will be important to explore whether a full-body inverse dynamics model with force and moment inputs at the hands and feet enhances the accuracy of the model to measure the upper limb joint forces and moments.

Appendix A

The 4×4 Homogeneous Transformation

The 4×4 homogeneous transformation matrix in equation (A.1), ${}^{i-1}_{i}\mathbf{T}$, defines the transformation of frame $\{i\}$ relative to frame $\{i-1\}$, and involves the parameters of rotation and translation defined by the D-H parameters in Table A.1 [12].

Table A.1: The Denavit-Hartenberg (D-H) parameters of the index finger model.

i	α_{i-1}	a_{i-1}	d_i	θ_i
1	0	0	0	θ_1
2	-90°	0	0	θ_2
3	0	l_1	0	θ_3
4	0	l_2	0	θ_4

$$
{}^{i-1}_{i}\mathbf{T} = \begin{bmatrix} c\theta_i & -s\theta_i & 0 & a_{i-1} \\ s\theta_i c\alpha_{i-1} & c\theta_i c\alpha_{i-1} & -s\alpha_{i-1} & -s\alpha_{i-1} d_i \\ s\theta_i s\alpha_{i-1} & c\theta_i s\alpha_{i-1} & c\alpha_{i-1} & c\alpha_{i-1} d_i \\ 0 & 0 & 0 & 1 \end{bmatrix} \tag{A.1}
$$

where $c\theta_i$ and $s\theta_i$ are $\cos\theta_i$ and $\sin\theta_i$, respectively. This transformation is a function of one independent variable (θ_i), and three spatial parameters (a_{i-1}, α_{i-1}, and d_i) of the kinematic chain [12].

Examples of calculation of the 4×4 homogeneous transformation matrices of frame

$\{0\}$ to $\{1\}$ and $\{1\}$ to $\{2\}$ are shown in equation (A.2) using the D-H parameters in Table A.1.

Since the fingertip is moving with frame $\{4\}$, the position vectors of the fingertip in this frame is $\mathbf{l}_3 = [l_3\ 0\ 0\ 1]^T$, and l_3 is the segment length of the distal phalanx of index finger, as shown in Figure 2.1.

Employing equation (A.1) by using the D-H parameters in Table A.1, we can obtain the following homogeneous transformation matrices.

$$ {}^0_1\mathbf{T} = \begin{bmatrix} c\theta_1 & -s\theta_1 & 0 & 0 \\ s\theta_1 & c\theta_1 & 0 & 0 \\ 0 & 0 & 1 & 0 \\ 0 & 0 & 0 & 1 \end{bmatrix} \qquad {}^1_2\mathbf{T} = \begin{bmatrix} c\theta_2 & -s\theta_2 & 0 & 0 \\ 0 & 0 & 1 & 0 \\ -s\theta_2 & -c\theta_2 & 1 & 0 \\ 0 & 0 & 0 & 1 \end{bmatrix} \tag{A.2} $$

Equation (A.3) calculates the position vector $\mathbf{p}_{tip} = [x_{tip}\ y_{tip}\ z_{tip}\ 1]^T$ of the tip of the index finger represented in the reference coordinate system $\{0\}$.

$$ \mathbf{p}_{tip} = {}^0_1\mathbf{T}\ {}^1_2\mathbf{T}\ {}^2_3\mathbf{T}\ {}^3_4\mathbf{T}\ \mathbf{l}_3 \tag{A.3} $$

Applying the forward kinematics, the 4×4 transformations can be multiplied together, and the x_{tip}, y_{tip}, and z_{tip} coordinates of the fingertip with respect to the base reference frame $\{0\}$, which initially coincides with frame $\{1\}$ in Figure 2.1b, are calculated.

Bibliography

[1] Jorge Angeles. *Fundamentals of Robotic Mechanical Systems: Theory, Methods, and Algorithms*. Springer-Verlag New York, Inc., Secaucus, NJ, USA, 1st edition, 1995.

[2] J. Apkarian, S. Naumann, and B. Cairns. A three-dimensional kinematic and dynamic model of the lower limb. *J Biomech*, 22(2):143–55, 1989.

[3] P. G. Arauz, S. A. Sisto, and I. Kao. Assessment of workspace attributes under simulated index finger proximal interphalangeal arthrodesis. *J Biomech Eng*, 2016. Arauz, Paul G Sisto, Sue A Kao, Imin ENG 2016/03/15 06:00 J Biomech Eng. 2016 Mar 14. doi: 10.1115/1.4032967.

[4] Signe Brunnstrom. *Brunnstrom's clinical kinesiology*. F. A. Davis Companyl, Philadelphia, PA 19103, 1996.

[5] J. P. Brutus, A. K. Palmer, J. F. Mosher, B. J. Harley, and J. B. Loftus. Use of a headless compressive screw for distal interphalangeal joint arthrodesis in digits: clinical outcome and review of complications. *J Hand Surg Am*, 31(1):85–9, 2006. Brutus, Jean-Paul Palmer, Andrew K Mosher, John F Harley, Brian J Loftus, Jon B eng 2006/01/31 09:00 J Hand Surg Am. 2006 Jan;31(1):85-9.

[6] I. Bullock, T. Feix, and A. Dollar. Workspace shape and characteristics for human two- and three-fingered precision manipulation. *IEEE Trans Biomed Eng*, 2015. Bullock, Ian Feix, Thomas Dollar, Aaron ENG 2015/04/04 06:00 IEEE Trans Biomed Eng. 2015 Mar 31.

[7] S. T. Canale, Jr. Cantler, E. D., T. D. Sisk, and 3rd Freeman, B. L. A chronicle of injuries of an american intercollegiate football team. *Am J Sports Med*, 9(6):384–9, 1981.

[8] H. Y. Chiu, S. C. Lin, F. C. Su, S. T. Wang, and H. Y. Hsu. The use of the motion analysis system for evaluation of loss of movement in the finger. *J Hand Surg Br*, 25(2):195–9, 2000. Chiu, H Y Lin, S C Su, F C Wang, S T Hsu, H Y eng Case Reports Scotland 2000/11/04 11:00 J Hand Surg Br. 2000 Apr;25(2):195-9.

[9] H. Y. Chiu and F. C. Su. The motion analysis system and the maximal area of fingertip motion. a preliminary report. *J Hand Surg Br*, 21(5):604–8, 1996. Chiu, H Y Su, F

C eng Research Support, Non-U.S. Gov't SCOTLAND 1996/10/01 J Hand Surg Br. 1996 Oct;21(5):604-8.

[10] H. Y. Chiu, F. C. Su, and S. T. Wang. The motion analysis system and the fingertip motion area. normal values in young adults. *J Hand Surg Br*, 23(1):53–6, 1998. Chiu, H Y Su, F C Wang, S T eng Research Support, Non-U.S. Gov't SCOTLAND 1998/05/08 J Hand Surg Br. 1998 Feb;23(1):53-6.

[11] H. Y. Chiu, F. C. Su, S. T. Wang, and H. Y. Hsu. The motion analysis system and goniometry of the finger joints. *J Hand Surg Br*, 23(6):788–91, 1998. Chiu, H Y Su, F C Wang, S T Hsu, H Y eng Research Support, Non-U.S. Gov't SCOTLAND 1999/01/15 J Hand Surg Br. 1998 Dec;23(6):788-91.

[12] John J. Craig. *Introduction to robotics : Mechanics and control*. Prentice Hall, Harlow, 2005.

[13] J. C. DeLee and W. C. Farney. Incidence of injury in texas high school football. *Am J Sports Med*, 20(5):575–80, 1992.

[14] B. J. Divelbiss and M. E. Baratz. The role of arthroplasty and arthrodesis following trauma to the upper extremity. *Hand Clin*, 15(2):335–45, ix, 1999. Divelbiss, B J Baratz, M E eng Review 1999/06/11 Hand Clin. 1999 May;15(2):335-45, ix.

[15] M. Domalain, P. J. Evans, Jr. Seitz, W. H., and Z. M. Li. Influence of index finger proximal interphalangeal joint arthrodesis on precision pinch kinematics. *J Hand Surg Am*, 36(12):1944–9, 2011. Domalain, Mathieu Evans, Peter J Seitz, William H Jr Li, Zong-Ming eng R01 AR056964/AR/NIAMS NIH HHS/ R01 AR056964-02/AR/NIAMS NIH HHS/ R01AR056964/AR/NIAMS NIH HHS/ Research Support, N.I.H., Extramural Research Support, Non-U.S. Gov't 2011/11/05 06:00 J Hand Surg Am. 2011 Dec;36(12):1944-9. doi: 10.1016/j.jhsa.2011.09.010. Epub 2011 Nov 3.

[16] S. S. Gamage and J. Lasenby. New least squares solutions for estimating the average centre of rotation and the axis of rotation. *J Biomech*, 35(1):87–93, 2002. Gamage, Sahan S Hiniduma Udugama Lasenby, Joan eng 2001/12/19 10:00 J Biomech. 2002 Jan;35(1):87-93.

[17] Jr. Gatt, C. J., T. M. Hosea, R. C. Palumbo, and J. P. Zawadsky. Impact loading of the lumbar spine during football blocking. *Am J Sports Med*, 25(3):317–21, 1997.

[18] B. Goislard de Monsabert, L. Vigouroux, D. Bendahan, and E. Berton. Quantification of finger joint loadings using musculoskeletal modelling clarifies mechanical risk factors of hand osteoarthritis. *Med Eng Phys*, 36(2):177–84, 2014.

[19] P. Hahn, H. Krimmer, A. Hradetzky, and U. Lanz. Quantitative analysis of the linkage between the interphalangeal joints of the index finger. an in vivo study. *J Hand Surg Br*, 20(5):696–9, 1995. Hahn, P Krimmer, H Hradetzky, A Lanz, U eng SCOTLAND 1995/10/01 J Hand Surg Br. 1995 Oct;20(5):696-9.

[20] I. Kao, S. F. Chen, Y. M. Li, and G. Wang. Sacst: Smart anthropomorphic contact surface technology. *Ieee Robotics & Automation Magazine*, 10(1):47–53, 2003. 660CR Times Cited:2 Cited References Count:23.

[21] I. Kao and M. R. Cutkosky. Quasi-static manipulation with compliance and sliding. *International Journal of Robotics Research*, 11(1):20–40, 1992. Hc871 Times Cited:56 Cited References Count:37.

[22] I. Kao and F. Q. Yang. Stiffness and contact mechanics for soft fingers in grasping and manipulation. *Ieee Transactions on Robotics and Automation*, 20(1):132–135, 2004. 776QL Times Cited:36 Cited References Count:6.

[23] L. D. Kaplan, D. C. Flanigan, J. Norwig, P. Jost, and J. Bradley. Prevalence and variance of shoulder injuries in elite collegiate football players. *Am J Sports Med*, 33(8):1142–6, 2005.

[24] S. J. Leibovic. Instructional course lecture. arthrodesis of the interphalangeal joints with headless compression screws. *J Hand Surg Am*, 32(7):1113–9, 2007. Leibovic, Stephen J eng Review 2007/09/11 09:00 J Hand Surg Am. 2007 Sep;32(7):1113-9.

[25] S. J. Leibovic, V. A. Richmond, and L. W. Strickland. Arthrodesis of the proximal interphalangeal joint of the finger - comparison of the use of the herbert screw with other fixation methods. *Journal of Hand Surgery-American Volume*, 19A(2):181–188, 1994. Nj837 Times Cited:24 Cited References Count:0.

[26] J. N. Leijnse, P. M. Quesada, and C. W. Spoor. Kinematic evaluation of the finger's interphalangeal joints coupling mechanism–variability, flexion-extension differences, triggers, locking swanneck deformities, anthropometric correlations. *J Biomech*, 43(12):2381–93, 2010. Leijnse, J N A L Quesada, P M Spoor, C W eng Evaluation Studies Validation Studies 2010/05/21 06:00 J Biomech. 2010 Aug 26;43(12):2381-93. doi: 10.1016/j.jbiomech.2010.04.021. Epub 2010 May 18.

[27] J. N. Leijnse, C. W. Spoor, and R. Shatford. The minimum number of muscles to control a chain of joints with and without tenodeses, arthrodeses, or braces–application to the human finger. *J Biomech*, 38(10):2028–36, 2005. Leijnse, J N A L Spoor, C W Shatford, R eng Research Support, Non-U.S. Gov't 2005/08/09 09:00 J Biomech. 2005 Oct;38(10):2028-36. Epub 2004 Dec 7.

[28] S. T. Leitkam, L. Bix, J. de la Fuente, and T. Reid Bush. Mapping kinematic functional abilities of the hand to three dimensional shapes for inclusive design. *J Biomech*, 48(11):2903–10, 2015. Leitkam, Samuel T Bix, Laura de la Fuente, Javier Reid Bush, Tamara eng 2015/05/03 06:00 J Biomech. 2015 Aug 20;48(11):2903-10. doi: 10.1016/j.jbiomech.2015.04.025. Epub 2015 Apr 22.

[29] S. T. Leitkam, T. R. Bush, and L. Bix. Determining functional finger capabilities of healthy adults: comparing experimental data to a biomechanical model. *J Biomech Eng*, 136(2):021022, 2014. Leitkam, Samuel T Bush, Tamara Reid Bix, Laura eng Comparative Study 2013/12/18 06:00 J Biomech Eng. 2014 Feb;136(2):021022. doi: 10.1115/1.4026255.

[30] Pamela K Levangie and Cynthia C Norkin. *Joint structure and function: a comprehensive analysis*. FA Davis, 2011.

[31] S. D. Mair, R. H. Zarzour, and K. P. Speer. Posterior labral injury in contact athletes. *Am J Sports Med*, 26(6):753–8, 1998.

[32] G. Mantovani, W. Y. Fukushima, A. B. Cho, M. A. Aita, Jr. Lino, W., and F. N. Faria. Alternative to the distal interphalangeal joint arthrodesis: lateral approach and plate fixation. *J Hand Surg Am*, 33(1):31–4, 2008. Mantovani, Gustavo Fukushima, Walter Y Cho, Alvaro Baik Aita, Marcio A Lino, Waldo Jr Faria, Fabiano Nunes eng 2008/02/12 09:00 J Hand Surg Am. 2008 Jan;33(1):31-4. doi: 10.1016/j.jhsa.2007.09.004.

[33] M. Mentzel, A. Benlic, N. J. Wachter, D. Gulkin, S. Bauknecht, and J. Gulke. [the dynamics of motion sequences of the finger joints during fist closure]. *Handchir Mikrochir Plast Chir*, 43(3):147–54, 2011. Mentzel, M Benlic, A Wachter, N J Gulkin, D Bauknecht, S Gulke, J ger English Abstract Germany 2011/04/01 06:00 Handchir Mikrochir Plast Chir. 2011 Jun;43(3):147-54. doi: 10.1055/s-0031-1271804. Epub 2011 Mar 30.

[34] C. D. Metcalf, S. V. Notley, P. H. Chappell, J. H. Burridge, and V. T. Yule. Validation and application of a computational model for wrist and hand movements using surface markers. *IEEE Trans Biomed Eng*, 55(3):1199–210, 2008. Metcalf, Cheryl D Notley, Scott V Chappell, Phappell H Burridge, Jane H Yule, Victoria T eng Evaluation Studies Research Support, Non-U.S. Gov't Validation Studies 2008/03/13 09:00 IEEE Trans Biomed Eng. 2008 Mar;55(3):1199-210. doi: 10.1109/TBME.2007.908087.

[35] A. Miller, P. Allen, V. Santos, and F. Valero-Cuevas. From robotic hands to human hands: a visualization and simulation engine for grasping research. *Industrial Robotan International Journal*, 32(1):55–63, 2005. 903vu Times Cited:23 Cited References Count:33.

[36] G. Rab, K. Petuskey, and A. Bagley. A method for determination of upper extremity kinematics. *Gait Posture*, 15(2):113–9, 2002.

[37] M. Rizzo, S. L. Moran, and A. Y. Shin. Long-term outcomes of trapeziometacarpal arthrodesis in the management of trapeziometacarpal arthritis. *J Hand Surg Am*, 34(1):20–6, 2009. Rizzo, Marco Moran, Steven L Shin, Alexander Y eng 2009/01/06 09:00 J Hand Surg Am. 2009 Jan;34(1):20-6. doi: 10.1016/j.jhsa.2008.09.022.

[38] J. A. Saal. Common american football injuries. *Sports Med*, 12(2):132–47, 1991.

[39] J. L. Sancho-Bru, A. Perez-Gonzalez, M. Vergara-Monedero, and D. Giurintano. A 3-d dynamic model of human finger for studying free movements. *J Biomech*, 34(11):1491–500, 2001. Sancho-Bru, J L Perez-Gonzalez, A Vergara-Monedero, M Giurintano, D eng Research Support, Non-U.S. Gov't Validation Studies 2001/10/24 10:00 J Biomech. 2001 Nov;34(11):1491-500.

[40] A. J. Schnorenberg, B. A. Slavens, M. Wang, L. C. Vogel, P. A. Smith, and G. F. Harris. Biomechanical model for evaluation of pediatric upper extremity joint dynamics during wheelchair mobility. *J Biomech*, 47(1):269–76, 2014.

[41] S. A. Sisto and G. Malanga. Osteoarthritis and therapeutic exercise. *Am J Phys Med Rehabil*, 85(11 Suppl):S69–78; quiz S79–81, 2006. Sisto, Sue Ann Malanga, Gerard eng Review 2006/11/03 09:00 Am J Phys Med Rehabil. 2006 Nov;85(11 Suppl):S69-78; quiz S79-81.

[42] A. B. Swanson, I. B. Matev, and G. de Groot. The strength of the hand. *Bull Prosthet Res*, 10(14):145–53, 1970.

[43] S. D. Turbeville, L. D. Cowan, W. L. Owen, N. R. Asal, and M. A. Anderson. Risk factors for injury in high school football players. *Am J Sports Med*, 31(6):974–80, 2003.

[44] H. Ueba, N. Moradi, H. C. Erne, T. R. Gardner, and R. J. Strauch. An anatomic and biomechanical study of the oblique retinacular ligament and its role in finger extension. *J Hand Surg Am*, 36(12):1959–64, 2011.

[45] R. L. Uhl. Proximal interphalangeal joint arthrodesis using the tension band technique. *J Hand Surg Am*, 32(6):914–7, 2007. Uhl, Richard L eng Lectures 2007/07/04 09:00 J Hand Surg Am. 2007 Jul-Aug;32(6):914-7.

[46] J. Usman, A. S. McIntosh, and B. Frechede. An investigation of shoulder forces in active shoulder tackles in rugby union football. *J Sci Med Sport*, 14(6):547–52, 2011.

[47] F. J. Valero-Cuevas, F. E. Zajac, and C. G. Burgar. Large index-fingertip forces are produced by subject-independent patterns of muscle excitation. *Journal of Biomechanics*, 31(8):693–703, 1998.

[48] F. C. van der Helm and G. M. Pronk. Three-dimensional recording and description of motions of the shoulder mechanism. *J Biomech Eng*, 117(1):27–40, 1995.

[49] H. Wagner, M. Buchecker, S. P. von Duvillard, and E. Muller. Kinematic description of elite vs. low level players in team-handball jump throw. *J Sports Sci Med*, 9(1):15–23, 2010.

[50] David A Winter. *Biomechanics and motor control of human movement*. John Wiley & Sons, 2009.

[51] J. A. Woodworth, M. B. McCullough, N. M. Grosland, and B. D. Adams. Impact of simulated proximal interphalangeal arthrodeses of all fingers on hand function. *J Hand Surg Am*, 31(6):940–6, 2006. Woodworth, Jessica A McCullough, Matthew B Grosland, Nicole M Adams, Brian D eng 2006/07/18 09:00 J Hand Surg Am. 2006 Jul-Aug;31(6):940-6.

[52] J. Yao, M. J. Park, D. Davis, and J. Chang. Ideal position for thumb interphalangeal arthrodesis in the era of smartphones and text communication. *Orthopedics*, 35(11):955–7, 2012. Yao, Jeffery Park, Min Jung Davis, Drew Chang, James eng 2012/11/07 06:00 Orthopedics. 2012 Nov;35(11):955-7. doi: 10.3928/01477447-20121023-07.

[53] R. Yokogawa and K. Hara. Manipulabilities of the index finger and thumb in three tip-pinch postures. *J Biomech Eng*, 126(2):212–9, 2004. Yokogawa, Ryuichi Hara, Kei eng Clinical Trial Research Support, Non-U.S. Gov't 2004/06/08 05:00 J Biomech Eng. 2004 Apr;126(2):212-9.

[54] Tsuneo Yoshikawa. *Foundations of robotics : analysis and control*. MIT Press, Cambridge, Mass., 1990.